THE GEOMETRY AND TOPOLOGY OF DEFORMATION BAND NETWORKS IN VOLCANICLASTIC ROCKS: A CASE STUDY FROM SHIHTIPING, SOUTH-EASTERN TAIWAN

Master in Geodynamics and Basin Studies

Torgeir Fenne Vestly

Department of Earth Science
University of Bergen
February 2021

ABSTRACT

Deformation bands are tabular strain localization features, common in porous and granular rocks. These structures of millimeter to centimeter thickness can occur as single bands and develop into clusters or networks of bands. Deformation bands have been extensively documented in siliciclastic rocks, whereas fewer studies address deformation bands in porous volcaniclastic rocks. In recent years, volcaniclastic reservoirs have become a hot topic in petroleum- and geothermal exploration, groundwater aquifers and CO_2 storage. Deformation bands are generally associated with a permeability reduction from one to three orders of magnitude compared to the host rock and deformation band networks may affect subsurface fluid flow patterns. Knowing the network properties of deformation bands are therefore crucial when predicting their impact on fluid flow. This M.Sc. project quantifies clusters and networks of deformation bands in volcaniclastic rocks from Shihtiping, Eastern Taiwan.

A thorough topological analysis of deformation band networks has been carried out, focusing on characterizing the distribution and connectivity of bands within a network. Individual deformation bands were analyzed based on their geometry, including length, density, and intensity, to access the spatial relationship of bands within the networks. The quantitative relation of nodes and branches provides the basis for describing the connectivity in the studied deformation band networks. The deformation band networks are generally dominated by connecting Y-nodes and fully connected (C-C) branches, resulting in high average connectivity. Furthermore, the topological characteristics can be associated with bifurcating, abutting, and splaying bands, and bands are less prone to crosscut one another. The highest connectivity is related to mature deformation band networks and deformation band networks in fully developed faults. This supports the theory that the connectivity of deformation networks develops with time and maturity (strain). The analyses of the deformation bands show that nodal distribution, intensity and connectivity are vulnerable to lithological heterogeneities across the network.

This study strengthens our understanding of the development of deformation bands in volcaniclastic rocks and explores the evolution of connectivity in deformation band networks. Quantifying the topological and geometrical characteristics of deformation band networks is essential as it generates parameters used to assess the potential for fluid flow in a reservoir.

Acknowledgements

This M.Sc. thesis is a part of my master's degree in Structural Geology at the Department of Earth Science at the University of Bergen. Throughout this project, I have received invaluable assistance and support. I would like to express my sincere gratitude to all of you who helped me along the way.

First and foremost, I would like to express my deepest gratitude to my main supervisor Prof. Atle Rotevatn (University of Bergen), and my co-supervisor Martin Kjenes (University of Bergen), for support and motivation throughout the project. Thank you for your constructive feedback, great discussions, and always being available, despite the COVID-19 outbreak.

A special thanks to both Bjørn Nyberg and Casey Nixon for introducing me to QGIS and NetworkGT. Bjørn Nyberg for always respond quickly to emails and being available for a chat in the office. I am also very grateful to Eivind Block Vagle and Martin Vika Gjesteland for teaching me the workflow in NetworkGT and for guidance throughout the thesis. I would also like to thank Leo Zijerveld and the IT department for setting up remote desktop access and organizing access to "Grotten" during the COVID-19 outbreak. Without this access, I could never have finished my work in QGIS. Thanks to Alma, Marthe, Martin, Eivind, Helene and others for discussions, feedback and proof reading.

I want to thank fellow students and friends at the University of Bergen for many great memories and fun times. The last years would not have been as fun without you guys. The social environment at the Department of Geosciences has been fantastic and I am grateful for the time we have had together.

Finally, I want to thank my family and Julie for their words of encouragement and support throughout the master.

Bergen, February 2021
Torgeir Fenne Vestly

List of contents

1 Introduction

This study builds upon two previous M.Sc. projects from 2018 (Jervidalo, 2018, Kjenes, 2018), where deformation bands in volcaniclastic porous rocks on the eastern coast of Taiwan were studied. These two projects focused on deformation mechanisms affecting volcaniclastic rocks at micro- and macroscale, while the focus of the present thesis is a quantitative study of the network properties (network geometry and topology) of deformation band networks in volcaniclastic rocks.

1.1 Rationale and background

Deformation bands are millimeter- to centimeter-thick tabular zones of localized strain in porous granular rocks and sediments (Aydin, 1978, Antonellini et al., 1994, Fossen and Bale, 2007, Ballas et al., 2015, Fossen et al., 2018). Deformation bands can occur as single structures, cluster zones, or as networks. The evolution and microstructure of deformation bands has for a long time been a topic of interest due to their influence on petrophysical properties (permeability and porosity) within subsurface reservoirs and aquifers (Antonellini et al., 1994, Sternlof et al., 2006, Fossen and Bale, 2007, Ballas et al., 2015, Fossen et al., 2018). Consequently, deformation bands spatial relationship could have implications for hydrocarbon exploration, geothermal reservoirs, groundwater aquifers and CO_2 storage (Schutter, 2003, Annunziatellis et al., 2008, Lenhardt and Götz, 2011, Zhu et al., 2011, Dinwiddie et al., 2012). Deformation bands have been extensively documented in siliciclastic rocks (e.g. Aydin and Johnson, 1978, Antonellini and Aydin, 1994, Fossen et al., 2007, Charalampidou et al., 2011). The last decade more research has been devoted to deformation bands in carbonate rocks and in the less studied volcaniclastic rocks (Tondi et al., 2012, Antonellini et al., 2014, Cavailhes and Rotevatn, 2018). Still, there are significant knowledge gaps surrounding the structure and evolution of deformation bands in volcaniclastic rocks; notably, there are no previous studies, to my knowledge, that study the network properties of deformation band networks in such rocks.

To address this knowledge gap, a topological approach was used, quantifying the network properties of the studied deformation band networks (e.g. Manzocchi, 2002, Sanderson and Nixon, 2015, Nyberg et al., 2018). In recent years, node and branch topology has become the state-of-the-art in the description, visualization and quantification of structural networks (e.g.

Manzocchi, 2002, Sanderson and Nixon, 2015, Morley and Nixon, 2016, Dimmen et al., 2017, Duffy et al., 2017, Nyberg et al., 2018, Awdal et al., 2020). This is an effective method to access spatial relationships such as deformation band intensity and connectivity within a network (described in Subchapter 2.5) (Sanderson and Nixon, 2015). The study of deformation band network topology and geometry adds valuable insights into band growth and linkage in volcaniclastic rocks, in addition to their effect on subsurface fluid flow.

1.2 Aims and objectives

The aim of this thesis is to investigate and improve the understanding of deformation band network properties in volcaniclastic rocks. This is achieved through performing topological analyses of clusters and networks of deformation bands. More specifically, quantifying and characterizing the distribution, geometry, and topology of deformation bands in volcaniclastic rocks from Shihtiping, Taiwan. The main aim will be reached by the following objectives:

1) Analyze virtual outcrops and merge images to obtain high resolution models of the deformation band networks.
2) Use topological analysis to quantify and compare the network properties (geometry, topology and distribution) of deformation band networks in volcaniclastic rocks.
3) Quantify and discuss spatial variation within deformation band networks in volcaniclastic rocks. How does the topology compare to other structural networks?
4) Discuss how resolution affects the nodal distribution in a deformation band network and how deformation bands topology control subsurface fluid flow.

1.3 Study area and data

The study area is located in Shihtiping on the island of Taiwan in East Asia (Fig. 1.1). Taiwan is situated at the convergence boundary between the Philippine Sea Plate and Eurasian Plate (Fig. 1.1A). The term ‘Cuesta’ is locally (and herein) used for the studied outcrop. The Cuesta (Fig. 1.1C red box) is situated in the Coastal Range, one of four structural domains in Taiwan (Huang et al., 2000). The Coastal Range is bounded to the west by the Longitudinal Valley Fault and to the east by the coastline (Fig. 1.1B). The studied deformation band networks are hosted in volcaniclastic rocks of polygenic conglomerate, ignimbrites and tuff of Miocene age (Song and Lo, 2002). The results from this study come from high resolution UAV- (unmanned

aerial vehicle) and close-up photos of deformation band networks. A more detailed description of the study area and the geological development of Taiwan can be found in Chapter 3.

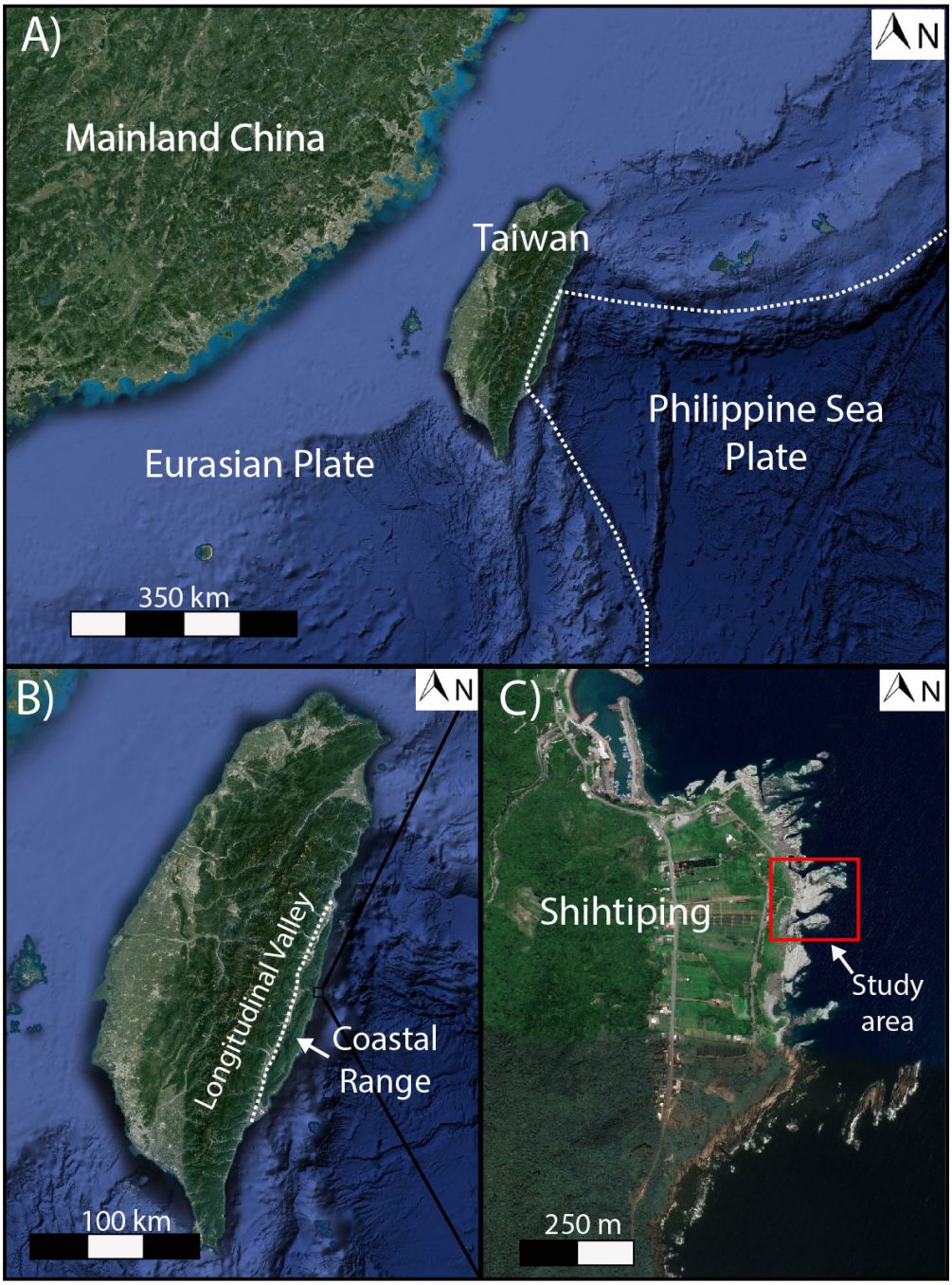

Figure 1.1: A) Satellite photo of Taiwan and where it is situated relative to South-Eastern China. Tectonic plates and boundaries are highlighted. B) Satellite photo of the island of Taiwan. The Longitudinal Valley and the Coastal Range are marked. C) Satellite photo of the coastline of Shihtiping and where the "Cuesta" study area is located. Satellite image © Google Earth 2021.

2 Theoretical background

The focus of this chapter is to review and explain existing terminology, theory, and concepts related to the formation and classification of deformation bands in porous media. The majority of previous studies focuses on deformation bands in porous sandstone and carbonates (Aydin, 1978, Antonellini and Aydin, 1994, Fossen et al., 2007, Tondi et al., 2012, Ballas et al., 2015, Fossen et al., 2018). Less research has been devoted to deformation bands in volcaniclastic rocks (Cavailhes and Rotevatn, 2018), however, the concepts from sandstone are transferable to volcaniclastic rocks. In this chapter, characteristics and classification of deformation bands will be covered in the subchapters 2.1 and 2.2, deformation bands effect on fluid flow in 2.3, deformation band in volcaniclastics in 2.4, whereas 2.5 will cover quantitative network topology and its application to deformation band networks.

2.1 Deformation bands

Deformation bands are expressed as millimeter to centimeter-thick tabular zones of strain-localization in granular and porous material. The term deformation band was first introduced by Aydin (1978). Since then, deformation bands have become a common term used to describe strain localization structures in porous rocks (e.g. Aydin and Johnson, 1978, Antonellini et al., 1994, Fossen and Bale, 2007, Soliva et al., 2013). These structures are limited to granular and porous material (porosity higher than c. 15%) and can develop in any tectonic regime (Fossen and Bale, 2007). Deformation bands occur as networks of bands, clusters, or as individual bands (Aydin and Johnson, 1978).

There is a significant difference between the accommodation of deformation in porous vs. non-porous rocks, and there are several ways to distinguish deformation bands from faults and fractures. Strain in highly porous rocks are associated with the formation of deformation bands, while strain in stiff, low porosity rocks is accommodated by slip-surfaces and extensional fractures (Fossen et al., 2007). In brittle fractures (e.g. joints), permeability increases, while deformation bands usually have an opposite effect with enhanced cohesion and reduced permeability and porosity (Davis et al., 2000, Lothe et al., 2002, Fossen and Bale, 2007). In addition, the high porosity in granular rocks promotes reorganization of grains, stress concentration at grain contacts and cataclasis (Fossen et al., 2007). The petrophysical properties (porosity and permeability) of porous and granular rocks are considered important to petroleum

geologists and hydrogeologists due to their good reservoir/aquifer potential. Deformation bands affect the petrophysical properties of the host rock and generally lower the permeability and porosity. Hence, deformation bands may act as baffles, or even barriers to fluid flow, if sufficiently abundant and low-permeable (Fossen et al., 2007).

2.2 Classification of deformation bands

Deformation bands are commonly classified in two different ways, according to i) *the dominant deformation mechanism*, or by ii) *kinematics* (Aydin et al., 2006, Fossen et al., 2007, 2018).

2.2.1 Mechanisms

Deformation bands are formed by one or more mechanisms, where the classification is based on the dominant deformation mechanism (Aydin et al., 2006, Fossen et al., 2007). The deformation mechanisms comprise reorganization of grain, cataclasis (grain crushing/fracturing), phyllosilicate smearing, dissolution and cementation (Fossen et al., 2007) (Fig. 2.2). The type of deformation depends on several external and internal host rock conditions. Internal properties include porosity, grain distribution, grain size and shape, sorting, mineralogy, and cementation. At the same time, external conditions include burial depth (confining pressure), deviatoric stress (tectonic regime), and fluid overpressure (listed in Fig. 2.1B). Over time, external conditions will affect the deformation of any porous material (Fossen et al., 2007, Fossen et al., 2018). The different deformation mechanisms generate bands with distinctive petrophysical properties which affect fluid flow in a reservoir, these different types of bands will be addressed in the following.

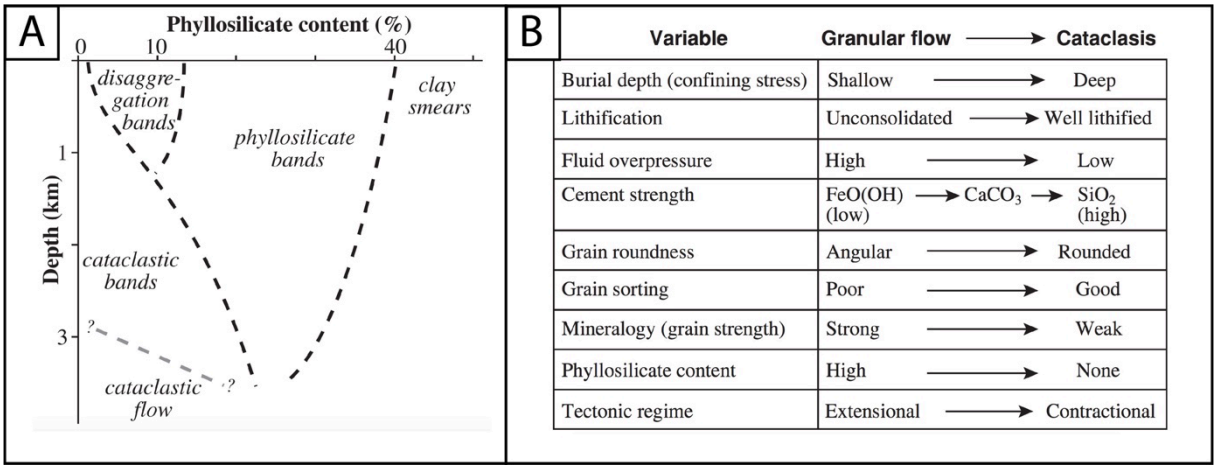

Figure 2.1: A) Relationship between burial depth and phyllosilicate content and their effect on different types of deformation bands. B) Table showing controlling factors influencing the degree of cataclasis. From Fossen et al. (2018).

Disaggregation bands

Disaggregation bands (Fig. 2.2A) are formed by reorganization of grains when the host rock is exposed to compression, dilation, and/or shearing, causing a granular flow (Rawling and Goodwin, 2003, Fossen et al., 2007). This process involves breaking of grain-bounding cement, sliding, and rolling and rotation of grains without crushing the grains, and will often lead to localized compaction (and thus a reduction of porosity) of the porous material within the band (Fossen et al., 2007). Disaggregation bands are normally formed at low confining pressure at shallow burial depths (< 1 km) and are commonly found in poorly consolidated rocks (e.g. Hesthammer and Fossen, 2001, Bense et al., 2003, Torabi, 2014). If fluid overpressure reduces the stress of the grain contacts, disaggregation bands can be formed at even deeper depths (Fossen et al., 2018). If the bands are dilatant (i.e. affected by an increase in porosity), disaggregation bands may increase fluid flow in the host rock (Antonellini and Aydin, 1994, Du Bernard et al., 2002a).

Phyllosilicate bands

Phyllosilicate bands (Fig. 2.2B), also referred to as framework phyllosilicates, develop in porous rocks that contain a certain amount of mica/clay minerals (14% - 40%) (Knipe et al., 1997). Phyllosilicate bands develop under the same conditions as disaggregation bands and are often considered as a sub-group of these (Fossen et al., 2003). The minerals act as a lubricant and enhance granular flow and grain boundary sliding (Fossen et al., 2018). Elongated phyllosilicate minerals relocate and align parallel to the band, resulting in an increased sealing effect (Fisher and Knipe, 2001). Permeability can be reduced up to five orders of magnitude where phyllosilicate grains are small (< 0 – 5 um) (Fisher and Knipe, 2001). Determined by the local source of phyllosilicates, the permeability may vary along the deformation bands (Fisher and Knipe, 2001).

Cataclastic bands

Cataclastic bands (Fig. 2.2C) form when applied stress leads to mechanical grain fracturing and crushing. Grain reorganization is also typical in the formation of these bands. Cataclastic bands commonly have an inner, compact core characterized by fractured and crushed, angular grains, poor sorting, a high proportion of matrix content (because of grain-size reduction), and less

pore space (Aydin, 1978, Aydin and Johnson, 1983). Around the inner core, there is an area that Fossen et al. (2007) has referred to as the transition zone. The transition zone is more compact than the host rock but has less fractured grains in comparison to the inner core (Fossen et al., 2007).

Cataclasis, grain-reorganization, and compaction cause grains to interlock, where crushed grains provide more contact points and distribute stress more evenly (Aydin and Johnson, 1983). This results in a strain hardening effect, favoring formation of new bands in the host rock instead of reactivating a stiffening deformation band (Mair et al., 2000). The deformation band becomes stiffer and stronger and thus more resistant to weathering in relation to the host rock (Rotevatn et al., 2013, Torabi, 2014, Tindall and Eckert, 2015). Cataclastic deformation bands can occur as single strands to larger clusters depending on the deformation intensity (Antonellini and Aydin, 1994, Nicchio et al., 2017). Cataclastic bands have been documented in a variety of rocks and environmental conditions, e.g. bands in porous sandstones with burial depth 1.5 - 2.5 km (most common) (Du Bernard et al., 2002b, Soliva et al., 2013, Fossen et al., 2018), unconsolidated marine sand buried at 80 m (Cashman and Cashman, 2000), carbonate grainstones (Rotevatn et al., 2016), subglacial deformation till (van der Meer et al., 2003) and tuffs and non-welded ignimbrites (Wilson et al., 2003).

Solution and cementation bands

Solution and cementation bands (Fig. 2.2D) form due to dissolution and/or cementation processes. The dissolution and cementation along the band take place normally after deformation, occasionally during deformation (Fossen et al., 2007). These bands are typically dense, packed zones with grain sizes smaller than the matrix, and with no or little indication of cataclasis (Gibson, 1998, Fossen et al., 2007). These bands are associated with pressure solution and/or chemical compaction. In sandstone, these processes are triggered by greater burial depths and high temperatures (> 90°C) (Walderhaug, 1996, Fossen et al., 2007). However, these bands are more common in carbonate rocks (Tondi et al., 2006, Cilona et al., 2012). Precipitation and cementing along the bands occur most frequently on fresh cracked and exposed grain surfaces, and in tensile fractures (Leveille et al., 1997, Fossen et al., 2007). Compared to extensional regimes, the pressure solution is more common in contractional regimes (Rath et al., 2011, Rotevatn et al., 2016). It has been observed that solution and cementation bands have a great impact on porosity and permeability (Ogilvie and Glover, 2001). In dilation cementation bands, there can be as much as a 75% decrease in porosity and

a decrease of five orders of magnitude in permeability (Ogilvie and Glover, 2001). However, fluid flow is not affected to any great extent due to their discontinuous nature (Fisher and Knipe, 2001).

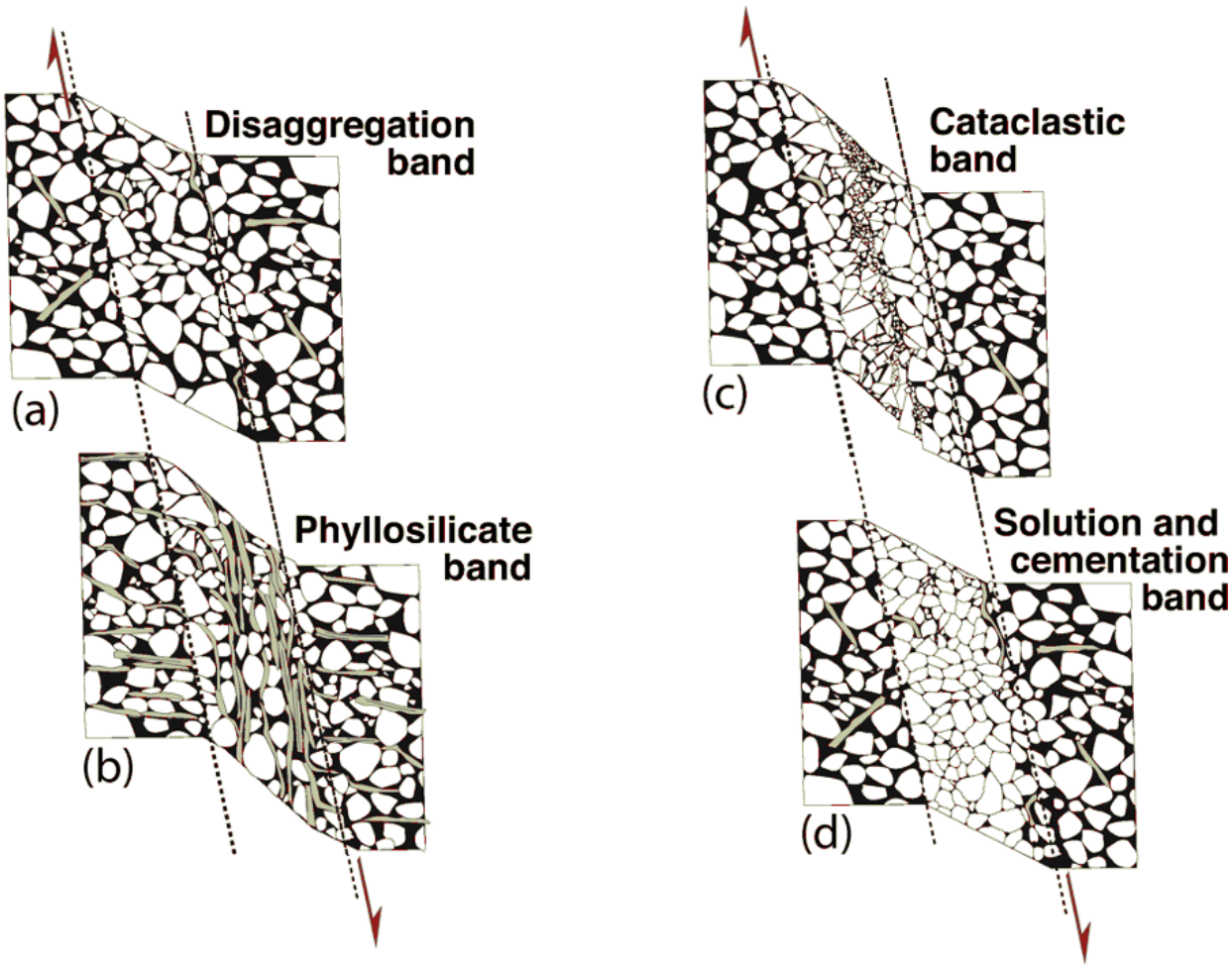

Figure 2.2: Classification of deformation bands based on the dominant deformation mechanism. A) Disaggregation band formed by granular flow. B) Phyllosilicate bands develop as a result of alignment of phyllosilicates. C) Cataclastic bands result from mechanical grain fracturing and crushing, resulting in grain size reduction. D) Solution and cementation bands are results of dissolution and/or cementation processes. Modified after Fossen et al. (2007).

2.2.2 Kinematics

The second approach to distinguish various types of deformation bands is by kinematics. Aydin et al. (2006) suggested the classification of deformation bands based on three end members: dilation bands (volume increase), simple shear bands (no volume change), and compaction bands (volume decrease) (Fig. 2.3). However, a combination of these is more common (e.g. compactional shear bands and shear enhanced compaction bands), with the combination of shear displacement and compaction as the most common (Aydin et al., 2006, Charalampidou et al., 2011, Fossen et al., 2018).

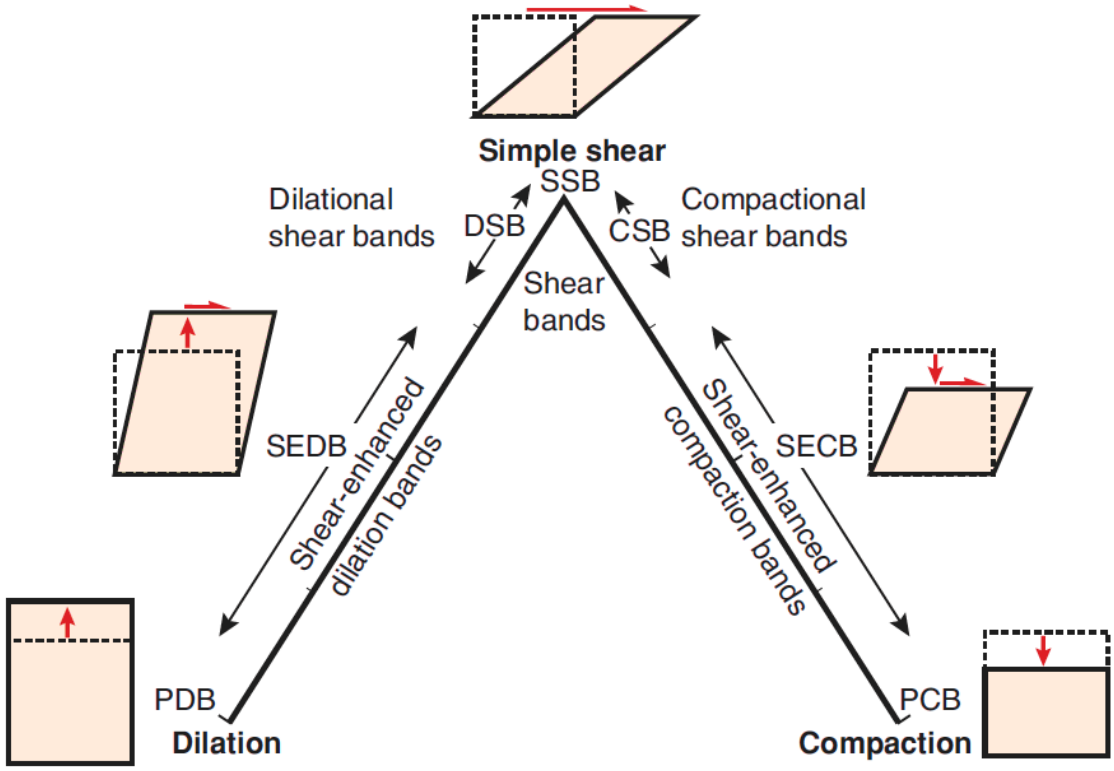

Figure 2.3: Classification of deformation bands based on kinematics, with the three end members: dilation bands (volume increase), simple shear bands (no volume change), and compaction bands (volume decrease). PDB: pure dilation band, SEDB: Shear-enhanced dilation band, DSB: dilational shear band, SSB: simple shear band, CSB: compactional shear band, SECB: shear-enhanced compaction band, PCB: pure compaction band. Modified after Fossen et al. (2018).

Dilation bands (Fig. 2.3) represent volume expansion or dilation and show no shear displacement. This results in increasing pore space and permeability with respect to the host rock (Du Bernard et al., 2002a, Aydin et al., 2006, Fossen et al., 2007). The increased amount of porosity is accomplished by granular flow mechanisms through disaggregation (Fossen et al., 2007). Dilation bands are documented by Du Bernard et al. (2002a) in poorly consolidated, porous sand but is rarely found in the field (Fossen et al., 2007).

Compaction bands (Fig. 2.3) are characterized by volume loss or compaction, and no shear displacement. Strain is accommodated entirely by compactional volumetric deformation, resulting in a localized reduction of permeability and porosity loss with respect to the host rock (Mollema and Antonellini, 1996, Issen and Rudnicki, 2001, Bésuelle and Rudnicki, 2004, Fossen et al., 2015). Grain crushing (cataclasis), grain reorganization, or dissolution can generate compaction. Pure compaction bands can only be formed in a rock with a porosity of 30% or higher (Tondi et al., 2006, Fossen et al., 2015). Pure compaction bands have been documented in a variety of rocks, including Jurassic aeolian sandstones (Mollema and

Antonellini, 1996, Sternlof et al., 2006) and limestones (Antonellini et al., 2014, Rotevatn et al., 2016).

Simple shear or isochoric shear bands (Fig. 2.3) are characterized by no volume change, where grains are deformed by shearing. The displacement takes place parallel to the band. Grain rotation and translation (i.e. granular flow) are the primary deformation mechanism. Simple shear bands are rarely found in the field. More common are compactional shear bands with a combination of compaction and shear (Aydin et al., 2006, Fossen et al., 2018).

2.3 Effect on petrophysical properties and fluid flow

The influence of deformation bands on petrophysical properties has been heavily investigated in previous studies (Sternlof et al., 2006, Fossen and Bale, 2007, Rotevatn et al., 2009b, Fossen and Rotevatn, 2012, Rotevatn et al., 2013). Deformation bands can cause a reduction in permeability up to six orders of magnitude and reduction in porosity by one order of magnitude (Antonellini and Aydin, 1994, Fisher and Knipe, 2001, Ballas et al., 2015). The bands distribution, orientation, connectivity and thickness determine whether they act as baffles or pathways to subsurface fluid flow (Fossen and Bale, 2007, Brandenburg et al., 2012, Fossen et al., 2018). Independent of the tectonic regime, deformation band development favors the stratigraphic units with the highest porosity (and often with higher permeability). Conceding that, a reduction in porosity and permeability in the most permeable layer would reduce fluid flow (effective permeability) in the reservoir (Fossen and Rotevatn, 2012). The sealing capacity of clusters and individual bands is greatly affected by lateral differences in porosity, permeability, and thickness (Torabi and Fossen, 2009). According to Torabi et al. (2013) thick clusters of cataclastic deformation bands have the potential to create significant hydrocarbon traps if they are connected to a continuous slip-surface. Variations within the deformation band clusters (porosity, permeability, and thickness) are components that can also act as leakage points and will weaken deformation bands sealing effect (Fossen and Bale, 2007, Rotevatn et al., 2013, Torabi et al., 2013). Even though the deformation bands do not completely seal fluids, they may be of importance considering the three-dimensional flow patterns in the reservoir (Fossen and Bale, 2007).

2.4 Deformation bands in volcaniclastics

Deformation bands have been extensively documented in siliciclastics. However, less work has been done on the development of deformation bands in volcaniclastics rocks (Soden and Shipton, 2013). The term "volcaniclastic" was first introduced by Fisher (1961) to distinguish sedimentary facies produced or affected by volcanism. This includes all clastic material entirely or partly composed of volcanic fragments, as well as any particle-forming mechanism (e.g. pyroclastic and epiclastic) (Fisher and Smith, 1991). Deformation structures such as faults, fractures, and deformation bands are all naturally occurring in porous and granular volcaniclastic rocks (Wilson et al., 2006, Dinwiddie et al., 2006, McGinnis et al., 2009, Riley et al., 2010, Soden and Shipton, 2013). Deformation bands of volcanic origin are found in ignimbrites (Wilson et al., 2003), and in welded and non-welded tuffs (Evans and Bradbury, 2004). Ignimbrites are pyroclastic deposits made mostly from pumiceous material, placed in a hot and concentrated particulate flow (Walker, 1983). Tuff is ash deposits with a grain size of < 2 mm (Fisher, 1961). Both ignimbrite and tuff have low bulk density and high porosity (Moon, 1993, Fisher, 1961).

Previous studies show that porosity and the degree of welding are the primary controlling factors for mechanical strength and failure in volcaniclastic rocks (Moon, 1993b, Wilson et al., 2003, Evans and Bradbury, 2004, Zhu et al., 2011, Okubo, 2012). The rock's mechanical strength is further enhanced by post-depositional mineralization of volcanic glass into crystals, reducing pore space, and favoring brittle deformation (Wilson et al., 2003, Wilson, 2004). Ignimbrites with low porosity and a high degree of welding typically deform as fractures and faults (Wilson et al., 2003, Riley et al., 2010, Soden and Shipton, 2013). Deformation bands, by contrast, form in non-welded, high porosity ignimbrites with poor consolidation (Zhu et al., 2011). Properties of volcaniclastic rocks may also be influenced by several other factors, including grain shape and size, presence of clay minerals, microcracks, grain organization, the presence of water, pumice, and lithophysae (Wilson et al., 2003, Zhu et al., 2011, Okubo, 2012). Several deformation processes have been documented in volcaniclastic rocks such as shearing, grain crushing, grain boundary sliding, and compaction (Wilson et al., 2006), and various types of deformation bands have been reported from field e.g. cataclastic bands in nonwelded tuffs (Evans and Bradbury, 2004) and pumice (Wilson et al., 2006), disaggregation and dilation bands in ash and pumice units (Dinwiddie et al., 2012).

Deformation bands in volcaniclastic rocks show similar changes in petrophysical properties relative to the host rock, as in sandstones and carbonates (Wilson et al., 2003, Evans and Bradbury, 2004, Dinwiddie et al., 2006, 2012, Lin and Huang, 2014). Volcaniclastic rocks (like ignimbrites and tuffs) often exhibit high porosity (Moon, 1993). They are therefore, potential hydrocarbon reservoirs (Schutter, 2003), geothermal reservoirs (Zhu et al., 2011), groundwater aquifers (Lenhardt and Götz, 2011), nuclear waste repositories (Dinwiddie et al., 2012), and CO_2 storage (Annunziatellis et al., 2008). However, the development of deformation bands in volcaniclastic rocks are not investigated to a large extent (Walker et al., 2013, Cavailhes and Rotevatn, 2018).

2.5 Quantitative network topology and its application to deformation band networks

Topology is used to characterize and quantify complex networks in various sciences (e.g. engineering, communication, social sciences, and geology) (Latora and Marchiori, 2002, Boccaletti et al., 2006, Thiele et al., 2016). In geology, topological analyses have become an effective method for characterization and visualization of fracture networks (Manzocchi, 2002, Sanderson and Nixon, 2015, Nyberg et al., 2018). Previous studies focus on topology in fracture networks, and thorough topological analyses of deformation band networks has only recently been conducted (Awdal et al., 2020, Wilson et al., 2020). However, the concepts are transferable. An individual deformation band is often described by its geometry, such as band length, width, and orientation (Fossen and Hesthammer, 1997, Manzocchi et al., 1998, Fossen et al., 2005). However, topology is useful as deformation bands often occur as networks, and network properties are often more related to topology than geometry (Sanderson and Nixon, 2015).

In two-dimensions, the relationship of a deformation band network can be divided into branches and nodes (Manzocchi, 2002, Nixon, 2013, Morley and Nixon, 2016). A branch is a continuous line bounded by a node at each end, while nodes represent points where branches intersect, meet, or end (Fig. 2.4). Thereof, branches and nodes can be classified: An I-node represents an isolated tip of a branch, a Y-node is a point where a branch abuts or splays, and X-nodes represent the point where two branches fully crosscut each other (Manzocchi, 2002). Nodes are further used to identify three different types of branches: Isolated (I-I) branches, isolated by an I-node on each side, partly connected (C-I) branches, with a connecting (X or Y) node and one

I-node, and fully connected (C-C) branches having two connecting nodes (Fig. 2.4) (Sanderson and Nixon, 2015).

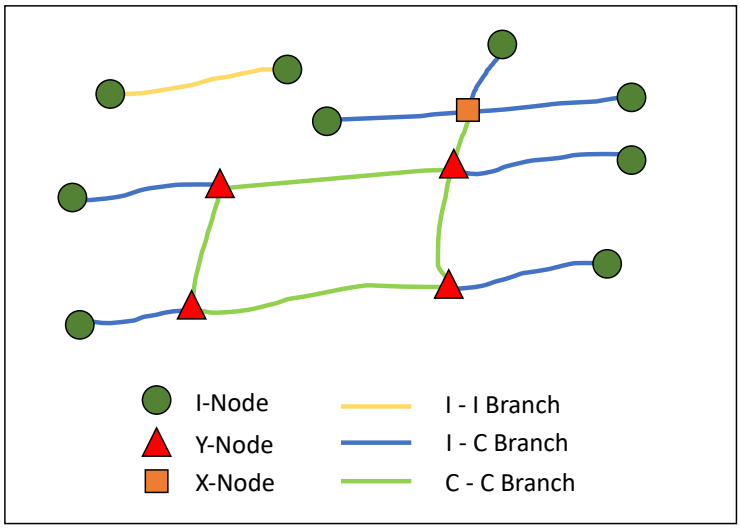

Figure 2.4: Schematic illustration of the different branches and nodes in a network. I-nodes represent the termination of an isolated tip. Y-nodes represent where a branch splays or abuts against another branch. X-nodes represent the point where two branches crosscut one another. I-I branches are isolated with two I-nodes on both end tips. I-C branches are partly connected, with one connecting node and one isolated node. C-C branches are fully connected branches with two connecting nodes on both end tips. Terminology from Sanderson and Nixon (2015).

The development of software has made it easy to extract statistics from deformation networks. For example, the proportions of branches and nodes can be addressed with ternary plots (Fig. 4.2) (Ortega and Marrett, 2000, Manzocchi, 2002, Sanderson and Nixon, 2015). An underdeveloped network will normally have a lower proportion of Y- and X-nodes (Sanderson and Nixon, 2015), representing low connectivity. Mature networks typically have higher connectivity, thus, a higher proportion of Y- and X-nodes (Sanderson and Nixon, 2015). Fracture networks generally show a higher proportion of Y-nodes than X-nodes. Preservation problems occur when an active fault meets a recently active fault, the younger faults stop at the older fault, resulting in two Y-nodes, instead of one X-node in two dimensions (Morley and Nixon, 2016). Deformation band networks with a higher proportion of Y-nodes has been documented in ternary plots from Manzocchi (2002). The use and visualization of topology in this thesis will be further explained in the data and methodology chapter (Chapter 4).

3 Geological framework

This chapter provides an overview of the regional structural and stratigraphic framework of Taiwan. The main focus is the Coastal Range, on the eastern part of the island, where the study area Shihtiping is located.

3.1 Regional tectonic setting

The island of Taiwan is located in southeast Asia and is separated from mainland China by the South China Sea. The geological architecture of the island is dominated by the Miocene to presently active Taiwan orogeny, related to the convergent plate boundary between the Philippine Sea Plate and the Eurasian Plate (Lu and Hsu, 1992, Lu and Malavieille, 1994, Yui et al., 2012) (Fig. 3.1A). Oblique convergence of these plates gives a relative NW - SE plate motion of about 8 cm/yr (Fig. 3.1A) (Lee et al., 2001).

Taiwan is situated in an active subduction-collision region (Fig. 3.1). To the south, the oceanic lithosphere of the South China Sea is subducted beneath the Philippine Sea Plate along the Manila trench, inducing the volcanism of the Luzon Arc (Huang et al., 1997, Taylor and Hayes, 1983, Sibuet and Hsu, 2004).

In the north-east of Taiwan, the Philippine Sea Plate is subducted beneath the Eurasian continent along the Ryukyu trench, resulting in the Ryukyu arc (Fig. 3.1B). The subduction of the Philippine Sea Plate beneath the Ryukyu arc in the north, initiates the formation of Okinawa back-arc basin. The subduction occurred as a result of active extension and extensional collapse of the northern Taiwanese mountain belt as a result of crustal thinning (Teng, 1996, Lallemand et al., 2001, Huang et al., 2006). The evolution of Taiwan itself is the result of arc-continent collision between the Luzon Arc and Eurasian Plate, which took place in the Middle Miocene to Late Pliocene (Chai, 1972, Page and Suppe, 1981, Malavieille and Trullenque, 2009).

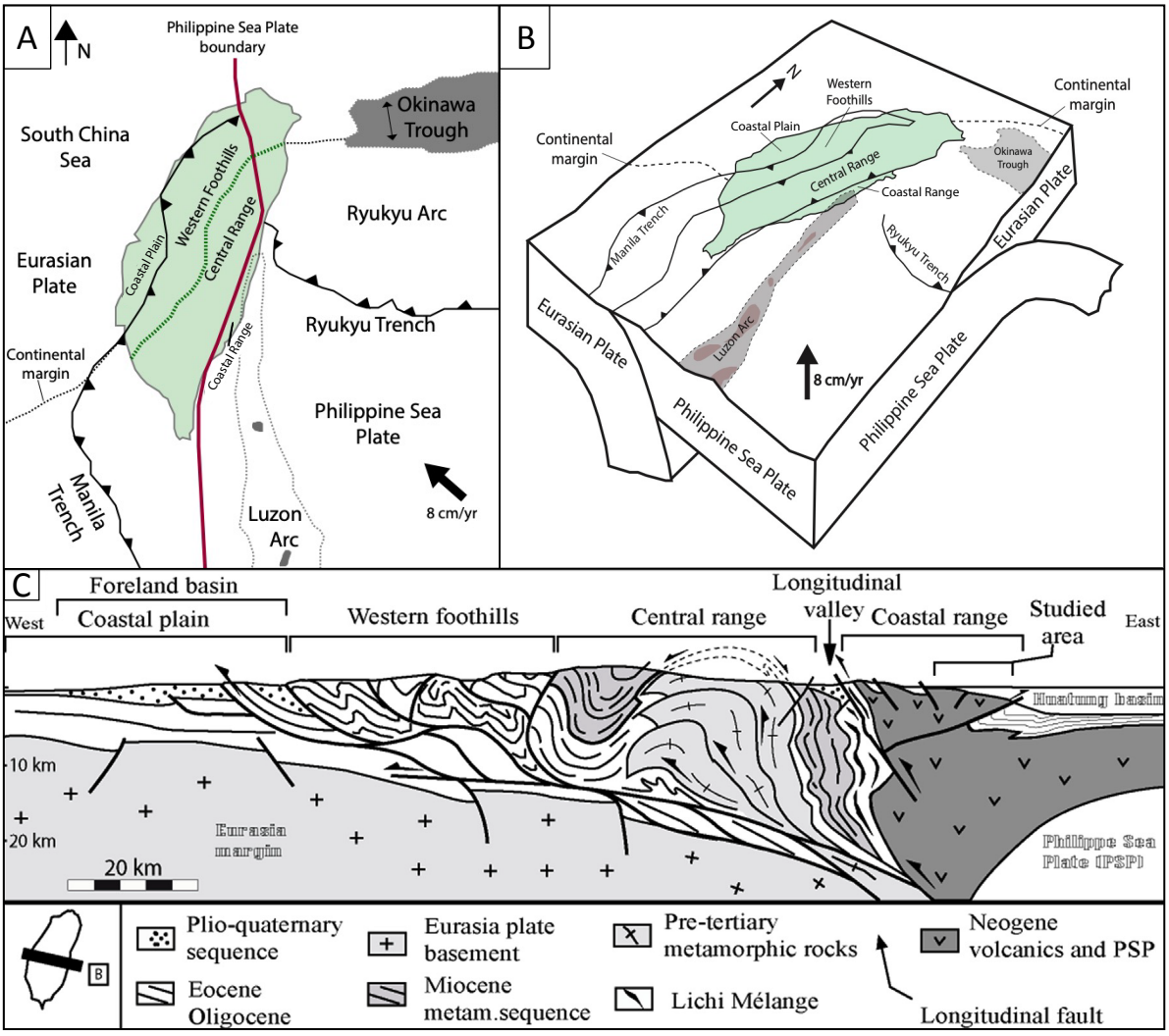

Figure 3.1: A) Sketch of Taiwan's tectonic setting and where the four structural domains are located on the island: (1) the Coastal Plain to the west; (2) the Western Foothills; (3) The Central Range, and (4) the Coastal Range. Modified from Sibuet and Hsu (2004). B) Map of Taiwan and surrounding tectonics related to the NW - SE convergence between the Philippine Sea Plate and the Eurasian Plate. Modified from Chang et al. (2001). C) Geological cross-sections of Taiwan from west to east, from Cavailhes and Rotevatn (2018).

Plate reorganization along the Pacific Plate induced Taiwan's formation in the Early Miocene (16 Ma). The Luzon Arc (N S trending) and the convergent collision zone were oblique relative to mainland China, resulting in a stepwise evolution of the collision zone from the north towards the south (Teng, 1990, Malavieille et al., 2002, Sibuet and Hsu, 2004). The southern part of Taiwan, along with the Manila Subduction zone, is in a pre-collisional phase. The central part of Taiwan represents on-going collision and mountain building, while the northeastern part is in the stage of orogen collapse (Thomas et al., 2014a). The Manila Subduction zone became active around 15 Ma due to the subduction of the Eurasian margin under the Philippine Sea Plate and initiated the intra-oceanic subduction stage (Wolfe, 1981, Sibuet and Hsu, 2004). Volcanism and accretion of marine sediments along the Manila Trench resulted in the formation

of the Luzon Arc (Fig. 3.2A). From the Early Miocene to the Late Miocene, the forearc basin was filled up by thick sequences of Tuluanshan volcanics and sediments (Thomas et al., 2014a). South of the Luzon Island, near 21°N, the present intra-oceanic subduction stage is active (Huang et al., 2000, Thomas et al., 2014b).

The initial arc-continent collision phase started in the Late Miocene (9 Ma), due to collision between the Luzon Arc and the Eurasian Plate (Teng, 1990, Sibuet and Hsu, 2004). The Luzon Arc failed to resist subduction and began colliding obliquely with the Eurasian Plate (Sibuet and Hsu, 2004). The initiation of the arc-continent collision begins with the closure of the Luzon Arc forearc basin, bringing the continental margin of China closer to the arc. During the collision, the forearc basin and its basement is consumed, and the Luzon Volcanic Arc is placed parallel to the fold-and-thrust belt of Taiwan (Fig. 3.2B). Today's initial arc-continent collision stage is located just south of Taiwan, at 21° 10'N to 22° 40'N (Huang et al., 2000, Huang et al., 2006).

The advanced arc-continent collision phase was entered 1.5 - 1 Ma. (Chi et al., 1981, Huang et al., 2006). The eastern part of Taiwan, the Coastal Range, is highly affected by this step, represented by east-dipping thrust faults in a volcanic succession (Fig. 3.2C). The arc-continent collision initiated when the Luzon Arc, together with sedimentary basins, was pushed and accreted onto the Eurasian margin. The Philippine Sea Plate, the Luzon Arc, and the Eurasian continental plate are divided by the Longitudinal Valley, which also separates the Central Range from the Coastal Range (Fig. 3.2C). Today, the advanced arc-continent collision zone is situated in the central part of Taiwan (22° 40'N to 24°N) and has very much formed Taiwan's geology (Angelier et al., 1997).

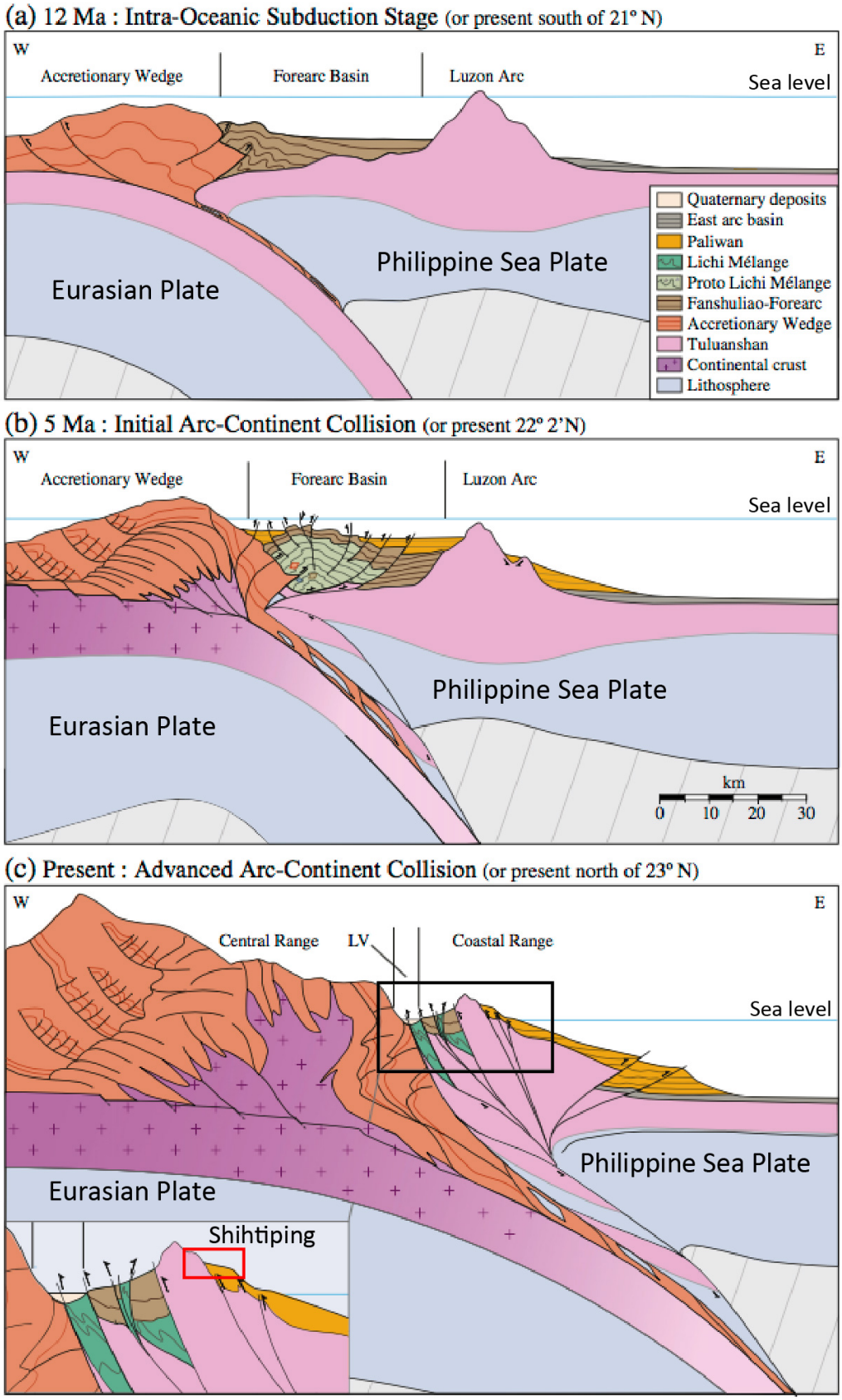

Figure 3.2: A step-by-step schematic model of the evolution of Taiwan. LV: Longitudinal Valley. A) Intra-oceanic subduction stage, inducing the volcanism of the Luzon Arc and Manila accretionary prism. B) Initial arc-continent collision stage, the collision of the Luzon Arc in the Eurasian Plate. C) Advanced arc-continent collision and present-day tectonic framework of the Coastal Range (black box) in Taiwan's eastern part. The red box refers to the approximately tectonic situation of Shihtiping. Modified from Thomas et al. (2014a).

3.2 Structural domains of Taiwan

The mountain belt of Taiwan can be subdivided into four structural domains, extending from west to east: the Coastal Plain, the Western Foothills, the Central Range, and the Coastal Range (Fig. 3.1C) (Huang et al., 2000, Huang et al., 2006, Cavailhes and Rotevatn, 2018). The western part includes the Coastal Plain, located at the top of the Eurasian marginal continental crust, forming Taiwan's present-day foreland basin (Yu and Chou, 2001). The Western Foothills are where sediments from the Eurasian continental margin have been deformed and accreted in a foreland fold-and-thrust belt (Suppe, 1980). The Central Range is characterized by uplifted, pre-collisional accretionary prism deposits, consisting of metasediments and gneisses of Eurasian continental margin affinity (Huang et al., 1997, Lin et al., 2003). The Central Range, and the Coastal Range are separated by a slim, linear, and seismically active valley called the Longitudinal Valley (Fig. 3.1A, C). The Coastal Range is formed by the accreted Luzon Volcanic Arc (Barrier and Angelier, 1986).

3.2.1 Coastal Range

The Coastal Range is a c. 150 km long and 15 km wide mountain chain, and represent the western boundary of the Philippine Sea Plate (Fig. 3.1A, B and Fig. 3.2C) (Jahn et al., 1986, Hsieh et al., 2004, Sibuet and Hsu, 2004, Yui et al., 2012). The structural domain results from the arc-continent collision between the Luzon Volcanic Arc and the Eurasian continental margin around 12 - 9 Ma (Teng and Wang, 1981, Sibuet and Hsu, 2004, Malavieille and Trullenque, 2009). The Coastal Range most likely included several volcanic islands, as magma continuously erupted in front of the subduction zone (Teng and Wang, 1981). The northernmost extension of the Luzon Volcanic Arc collided with the Eurasian Plate as further subduction took place, forming the Central Range as horizontal compressional tectonic forces led to buckling of the continental margin (Barrier and Angelier, 1986). As a result, the rocks in the Coastal Range were continuously thrusted and deformed at the margin (Teng and Wang, 1981). The Longitudinal Valley separates the Coastal Range from the Central Range on the Eurasian continental margin. The Longitudinal Valley Fault (Fig. 3.1C) delimits the coastal area to the east as a sinistral oblique thrust fault (Teng and Wang, 1981, Angelier et al., 1997), where the Coastal Range overthrust against the metamorphic basement of the Central Range (Barrier and Angelier, 1986). The Coastal Range consists of NNE-SSE trending synclines and anticlines in addition to low-angle, east-dipping imbricate thrust faults (Ho, 1986).

3.3. Stratigraphy: Tuluanshan Formation and the Shihtiping White Tuff

Based on the major lithology, the Coastal Range can be subdivided into five different units: the Tuluanshan Formation, the Paliwan Formation, the Fanshuliao Formation, the Lichi Formation, and the Pinianshan Conglomerate (Fig. 3.3) (Teng and Wang, 1981, Thomas et al., 2014b). Shihtiping is located within the Tuluanshan Formation.

Tuluanshan Formation

The Tuluanshan Formation (Fig. 3.3) is considered to be the oldest formation of the coastal area. Based on fossils and Ar/Ar geochronology, the unit has been dated to 16.6 – 3.5 Ma (Song et al., 1994, Song and Lo, 2002, Thomas et al., 2014b). The volcanic and volcaniclastic rocks in the formation originate from the Luzon Arc (described in Subchapter 3.1) and represent a volcanic sequence of several accreted volcanic islands (Song and Lo, 2002). Volcanic eruptions formed the volcanic islands in a deep marine environment in the Early Miocene, characterized by massive lava flows, pillow lavas, and hyaloclastites (Lai and Song, 2013, Song and Lo, 1988, Song and Lo, 2002). Sedimentary processes reworked volcanic material as the Luzon Arc entered a shallower environment in the Middle to Late Miocene. Thus, creating the volcaniclastic succession (Song and Lo, 2002). The volcanic islands gradually began to move from a marine environment and became subaerially exposed in the Early Pliocene (Teng et al., 1988). Consequently, the Tuluanshan Formation comprises a variety of volcaniclastic and volcanic rocks of andesitic origin, including volcanic breccia, lapilli stones, lava flows, tuffs, tuffaceous conglomerates, and sandstones (Hsu, 1956, Chang, 1967, Song and Lo, 2002, Thomas et al., 2014b). The upper part of the formation consists of limestones originating from fringing reefs formed when the islands were subaerially exposed (Teng and Lo, 1985, Huang et al., 1988, Song and Lo, 2002). The Tuluanshan Formation is approximately 1500 m thick and can be subdivided into three main units: the Shihtiping tuffs, the Shimen breccia and, the Kanghou limestones (Fig. 3.3C) (Song and Lo, 2002). The Kanghou limestones has been dated to be between 5.1 – 5.2 Ma, based on studies of foraminifers (Huang et al., 1988). The Kanghou limestones postdate the deposition of the Shihtiping tuffs, which contain the deformation bands studied in this thesis.

The Shihtiping tuff member

The Shihtiping tuffs host the deformation bands studied in this thesis and are the main lithology of interest. The Shihtiping tuffs is as aforementioned, a member of the Tuluanshan formation (Fig. 3.3) and comprises breccias, coarse- to fine-grained tuffs, pumices and, pyroclastic conglomerates, ignimbrites and sandstones (Song and Lo, 1988, 2002, Lai and Song, 2013). At the Cuesta study area, about 36 m (upper part) of this c. 100 m section is exposed (Cavailhes and Rotevatn, 2018). The Shihtiping tuffs at the Cuesta consist of non-welded ignimbrites, volcanic bombs (10 cm – 1 m diameter) of andesitic to basaltic composition and layered pyroclastic to volcaniclastic sandstones and conglomerates (0.5 – 5 m thickness) (Song and Lo, 2002, Cavailhes and Rotevatn, 2018). The ignimbrites are products of pyroclastic flows from the Chimei Volcano in Late Miocene and comprises poorly sorted, rounded to sub-angular volcanic bombs, lithic fragments, and pumice. Deformation structures within the ignimbrites show evidence of high temperature during deposition (Lai and Song, 2013). The tuffaceous sandstones originate from eroded tuff (Lai and Song, 2013). The tuffs contain crystal fragments (55 - 80 %), within a groundmass of volcanic glass and lithic fragments. The tuffs at Shihtiping consist of thin to thick layers of well-sorted, fine to medium ash interbedded with the ignimbrites (Song and Lo, 2002). The mineral composition in both the ignimbrite and the crystalline tuff consists mainly of plagioclase and hornblende, with smaller amounts of hypersthene, augite, and magnetite. Sedimentary structures such as herringbone cross-stratification and parallel lamination occur in the tuff, indicating deposition in a tidal environment (Song and Lo, 2002). Song and Lo (2002) suggest that the ignimbrites in Shihtiping developed in a subaerial environment, while the tuffaceous sandstone with herringbone cross-stratification are derived from a tidal environment. However, the tuffaceous sandstone may originate from eroded ignimbrites redeposited in tidal environments, and peperite in the ignimbrite layers may indicate that the hot pyroclastic flow was deposited in water (Song and Lo, 2002, Lai and Song, 2013).

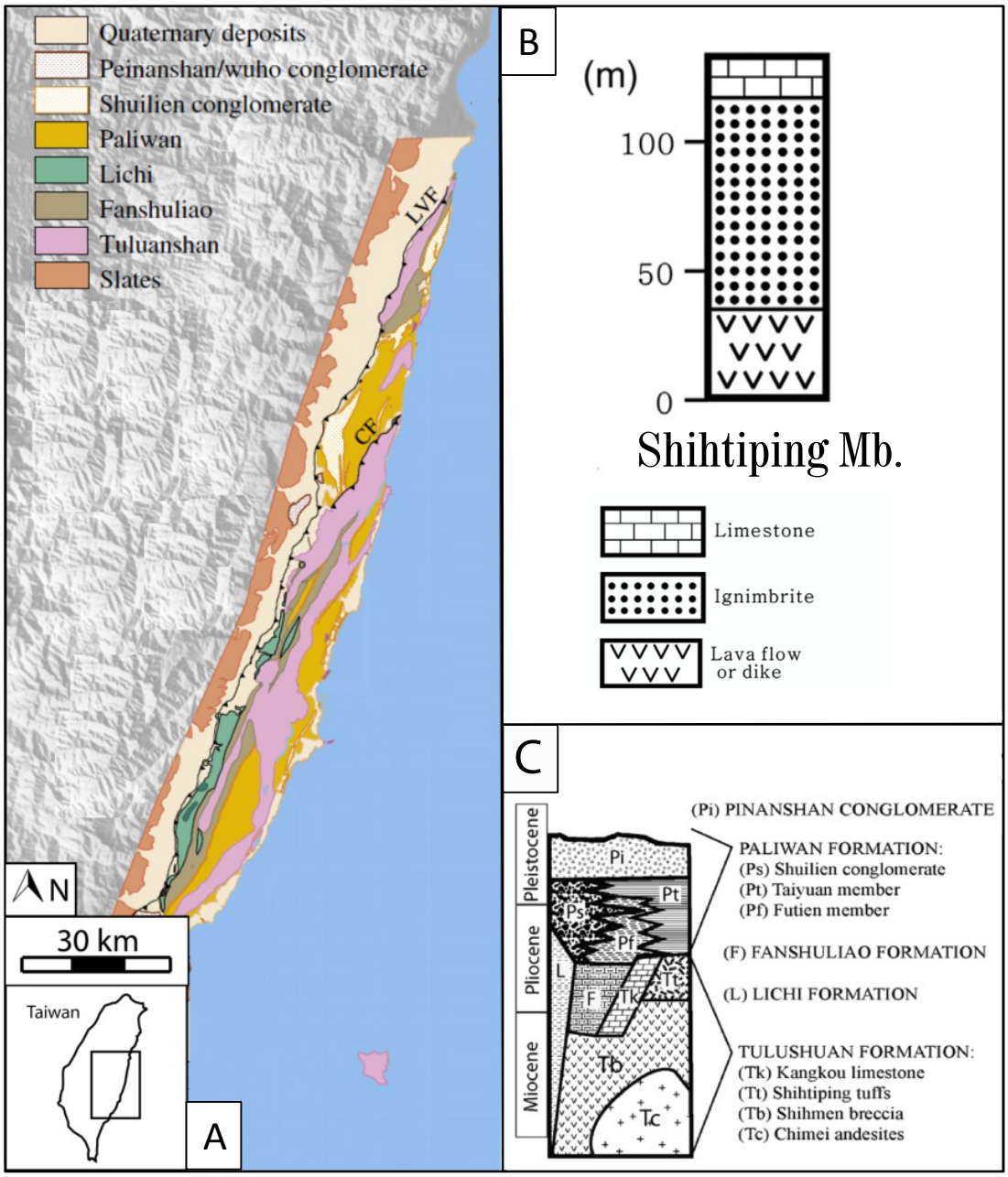

Figure 3.3: A) Geological map of Eastern Taiwan. Coastal Range is separated from the Central Range by the Longitudinal Valley Fault (LVF). CF: Chimei Fault. Modified from Thomas et al. (2014a). B) Illustration of the logged Shihtiping area by Song and Lo (2002). C) Representation of the stratigraphy of the Coastal Range. Modified from Cavailhes and Rotevatn (2018).

3.4 Structure and stratigraphy of the Shihtiping study area

Shihtiping is located in The Coastal Range which represents the northern tip of the Luzon Volcanic Arc (Fig. 3.1). The coastal area of Shihtiping is irregular and heavily affected by fracture networks and faults (Fig. 3.4A). A syncline-anticline pair (N-S to NNE-SSE) characterizes the area, consisting of gentle, parallel folds, with a distance of c. 300 m (Fig. 3.4B) (Cavailhes and Rotevatn, 2018). This thesis will focus on deformation bands, faults and fractures will therefore not be described in detail. The Tuluanshan Formation forms the basis of this study and consists of accreted island arc volcanic- and volcaniclastic rocks (Fig. 3.3).

The deformation bands in Shihtiping are light-colored relative to the host rock, tabular structures of millimeter-scale width, with a displacement of millimeter to centimeter-scale Cavailhes and Rotevatn (2018). Cavailhes and Rotevatn (2018) described the deformation bands in Shihtiping based on the Aydin et al. (2006) classification: orientation of the band relative to bedding, observable shear offset, porosity differences relative to the host rock and dominant deformation mechanism. Three different types of deformation bands were identified by Cavailhes and Rotevatn (2018): transverse-sense compactional shear bands, reverse-sense compactional shear bands and pure compaction bands.

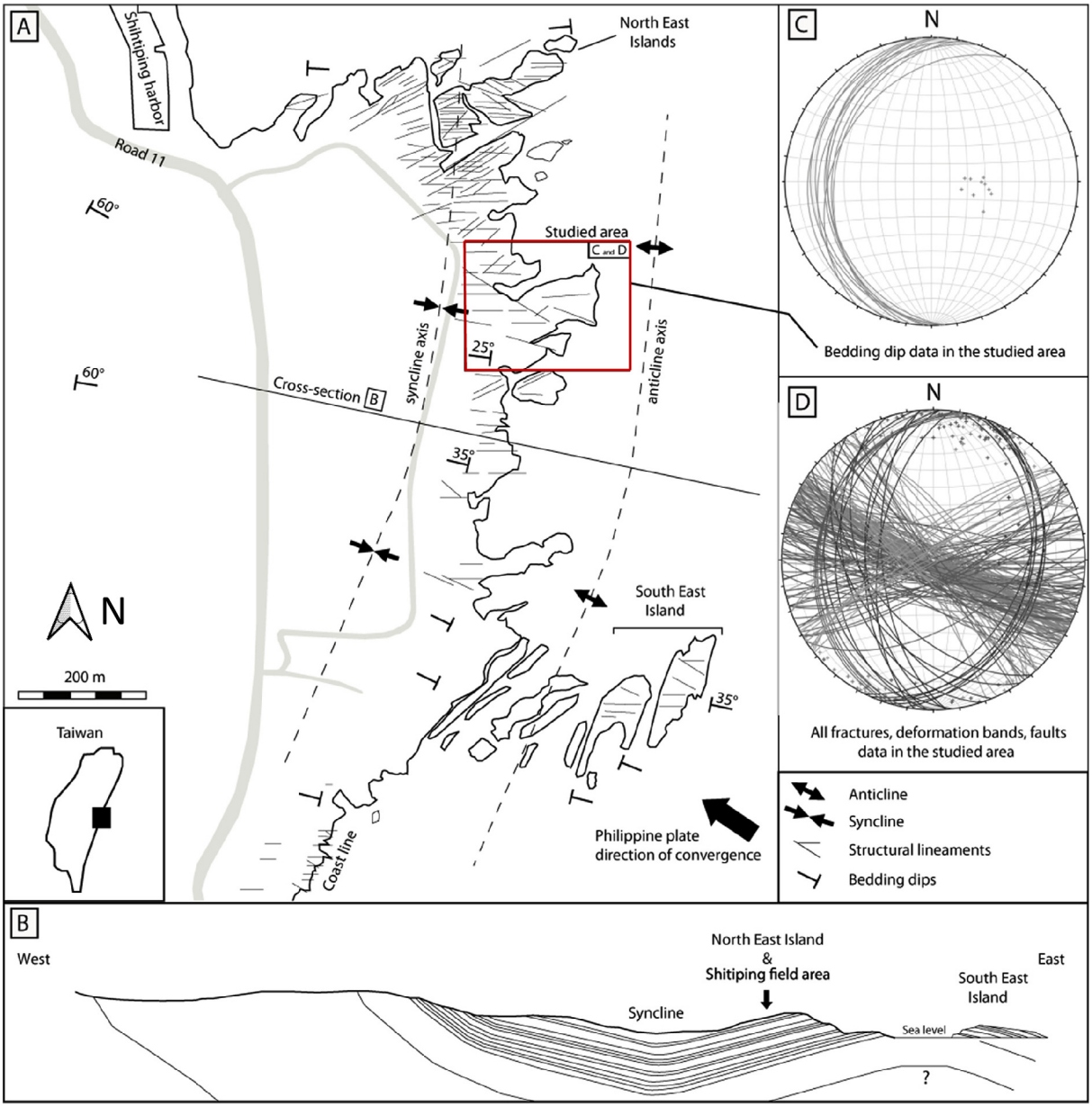

Figure 3.4: A) Structural sketch of the main structures in the Shihtiping area in the Coastal Range of Taiwan. B) Simplified W-E cross-section of the Shihtiping study area. C) The dip of the beds in the study area (red box) is shown in the lower hemisphere stereonet. D) The orientation of all fractures, deformation bands and faults in the study area is shown in the lower hemisphere stereonet. Modified from Cavailhes and Rotevatn (2018).

4 Data and methodology

This chapter provides an overview of the data and methods used in this thesis. The data used in this thesis were collected during two field seasons in Shihtiping, Taiwan, November 2016, and March 2017 by Jervidalo (2018) and Kjenes (2018). Structural data and images from deformation bands and faults were selected based on availability, exposure, and their differences in nature (Jervidalo, 2018, Kjenes, 2018). This study combines close-up photos of deformation bands and photos collected by UAV (unmanned aerial vehicle). The methodological workflow is shown in Figure 4.1. For a more detailed workflow see Appendix IV.

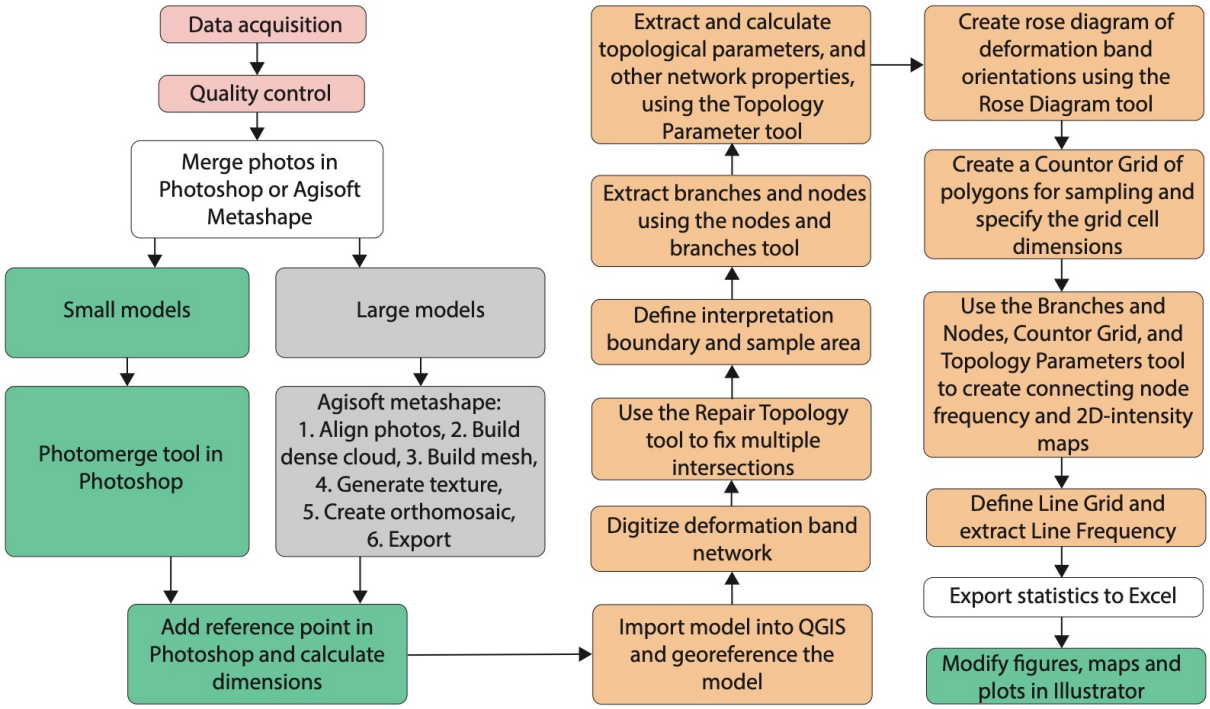

Figure 4.1: Simplified flow chart of the workflow used in this study. Red indicates the selection and quality assurance of photos. Green indicates the work done in Adobe Illustrator and Photoshop. Grey indicates work in Agisoft Metashape, and orange indicates work in QGIS.

4.1 Topology

A deformation band network will in two dimensions consist of an arrangement of branches and nodes. The proportions of I-nodes, Y-nodes and X-nodes (described in Subchapter 2.5) are the basis of topology, and topological characteristics can easily be extracted even with limited access to the network as a whole (Sanderson and Nixon, 2015). A network may consist of several deformation bands with a range of lengths and orientations with the potential to form an interconnected network. In structural geology, topology is used to describe spatial relationships such as connectivity and continuity in a network (Manzocchi, 2002, Sanderson and Nixon, 2015).

4.1.1 Connectivity

Quantifying connectivity can be done using the proportion of the nodes and branches. A branch will always be connected by a node on each side. I-nodes, Y-nodes, and X-nodes contributing to one, three, and four branches, respectively. The number of branches (N_B) can be derived from the equation:

$$N_B = \frac{1}{2}(N_I + 3N_Y + 4N_Y)$$

Where N_B = number of branches, N_I = number of I-nodes, N_y = number of Y-nodes, and N_x = number of X-nodes (Sanderson and Nixon, 2015).

The degree of connectivity in a deformation network is defined by the average connections per branch (C_B) (Sanderson and Nixon, 2015). The average number of connections per branch is a parameter from 0 - 2, considering that a branch can maximum have a number of two connecting nodes. A branch is either isolated (I-I branches) with no connections, partly connected (C-I) branches with one connection, or fully connected (C-C) branches having two connecting nodes. An isolated network consisting of I-I branches will have a $C_B = 0$, whereas fully connected networks consisting of X- and Y-nodes will have a connectivity (C_B) of 2 (Sanderson and Nixon, 2015). The average connections per branch can be calculated from the equation:

$$C_B = \frac{3N_Y + 4N_X}{N_B}$$

An effective way to display the level of connectivity is through ternary node- and branch diagrams (Fig. 4.2C). Connectivity has a direct link to the different types of branches and nodes. Deformation networks with a low level of connection will have a high proportion of I-I branches and will plot near the I-I corner and the I-node corner of the ternary diagrams (Fig. 4.2C). Networks that plot close to the C-C corner of the ternary diagram have a high proportion of interconnected branches (Fig. 4.2). Networks with few isolated branches will have higher Y- and X-nodes ratios and will plot in X and Y corner of the ternary diagram (Fig. 4.2C) (Sanderson and Nixon, 2015).

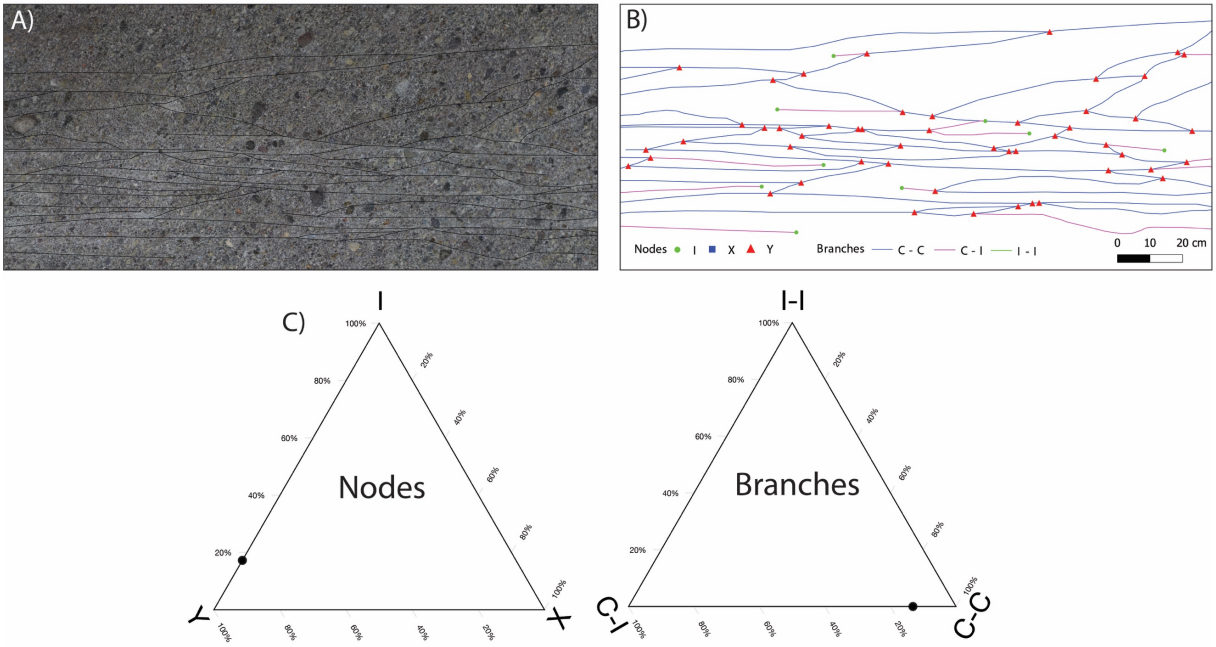

Figure 4.2: Figure illustrating how to display connectivity through ternary node- and branch diagrams from field photos. A) Digitalization of a deformation band network from a field photo. B) Topological data extracted from the network using the NetworkGT toolbox. C) The nodes and branches plotted in a ternary diagram.

4.1.2 Spatial visualization of networks

The extraction of geometric and topological properties for deformation networks provides an efficient way to analyze the spatial variability within the network (Nyberg et al., 2018). Contour grid mapping is a quantitative and useful approach for visualizing spatial variation in deformation band networks. Different parameters can be extracted from contour grid maps, such as deformation band intensity and frequency, connecting node frequency, and connections per branch. Creating multiple contour grid maps for different networks makes it possible to compare contrasts in different network properties. The deformation band intensity (m^{-1}), also known as 2D-intensity, is defined by total trace length (m) divided by sample area (m^2) (Mauldon et al., 2001, Sanderson and Nixon, 2015). Total trace length (m) is the calculated sum

of the length of branches (I-I, I-C, C-C) (Mauldon et al., 2001). Note that branches intersecting with the sample area's boundary form an E-node, and the branches are counted as "half branches." The connecting node frequency (m^{-2}) is divided from the number of connecting Y- and X-nodes inside the sample area (m^2) (Sanderson and Nixon, 2015). Deformation band frequency (m^{-2}) is defined by the number of branches within the sample area (m^2) (Sanderson and Nixon, 2015). Line samples are used to produce linear frequency, defined by the number of bands intersecting the line. The statistics are extracted from the attribute table in QGIS (Appendix II)

4.2 Data acquisition and processing

Data from the Cuesta study area was collected with an unmanned aerial vehicle (UAV) (model Phantom Dji 3) and a Nikon D3100 SLR camera. Significant time was spent going through 678 close-ups of deformation band networks in detail, to remove photos with distortion and bad quality. All the images were then merged together and georeferenced. Based on this, two faults, four sinistral deformation band networks (SN), three dextral deformation band networks (DN) and two incipient deformation band networks (IDBN) (Fig. 4.3) were selected for further investigations and topological analyses. Interpretations of deformation structures were performed on different scales, from drone images to close-up pictures, which captures details on a millimeter-scale.

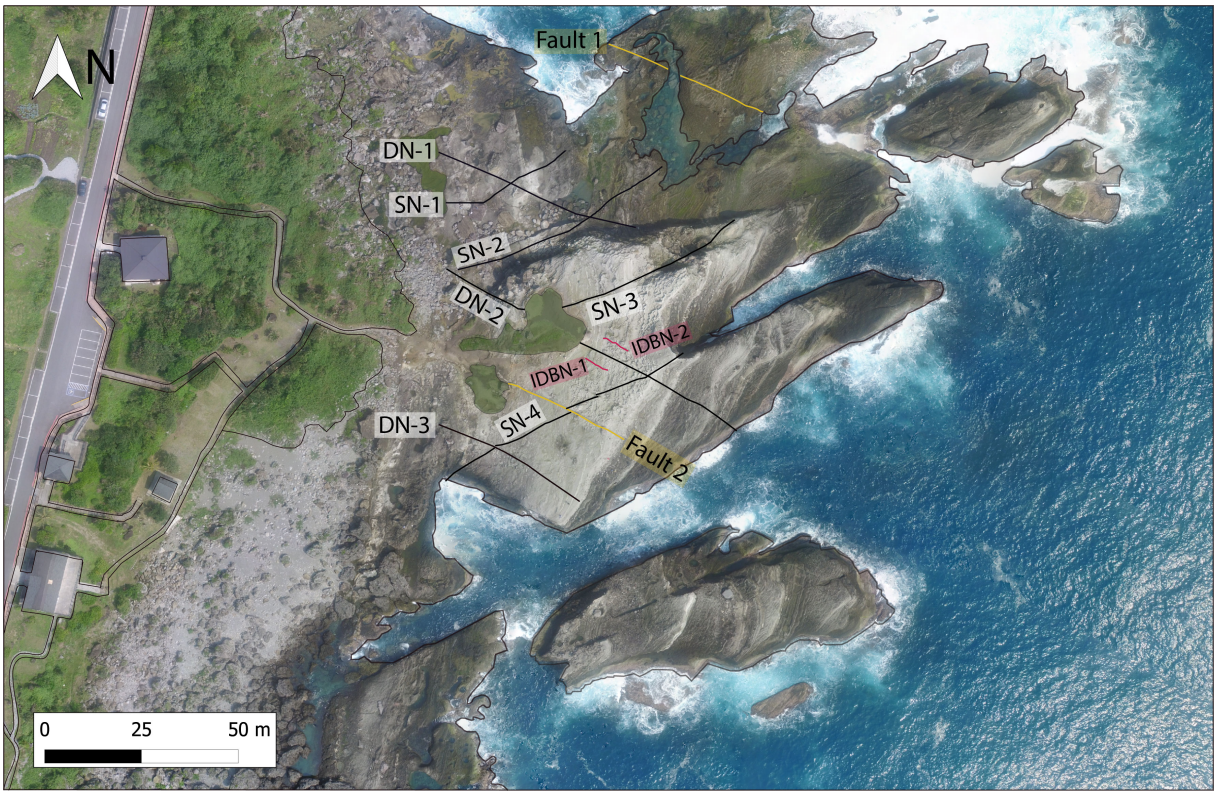

Figure 4.3: UAV photo of the studied area and the deformation band network localities. SN = Sinistral network and DN = Dextral network, outlined in black. Fault 1 (northern fault) and Fault 2 (southern fault) are marked in yellow. IDBN = Incipient deformation band networks, outlined in pink.

4.2.1 The use of virtual outcrops

Analyzing the evolution of the Earth often requires on-site exploration. Nevertheless, gaining access to the field area is not always achievable (e.g. during pandemics, wars and restricted areas). Virtual outcrops allow us to visit the field area without being physically present. The use of three-dimensional (3-D) data is becoming increasingly common in many areas of geosciences (e.g. geology, geomorphology, hydrology, volcanology, natural hazards, and mining) (Buckley et al., 2019). This rapid increase in usage is driven by new innovations in hardware and software, including unmanned aerial vehicles (UAV) that make it easier to collect and process large amounts of data (Buckley et al., 2019).

A virtual outcrop (Fig. 4.4) model was provided to gain an overview of the field area and locate and study deformation structures on a larger scale. The virtual outcrop model is based on photographs previously collected by UAV in March 2017. The photographs were processed, merged, and georeferenced using Agisoft Photoscan 1.3.2, resulting in a photo orthomosaic covering approximately 35100 m^2 of the Cuesta study area. The workflow showing how to create the model is attached in Appendix IV.

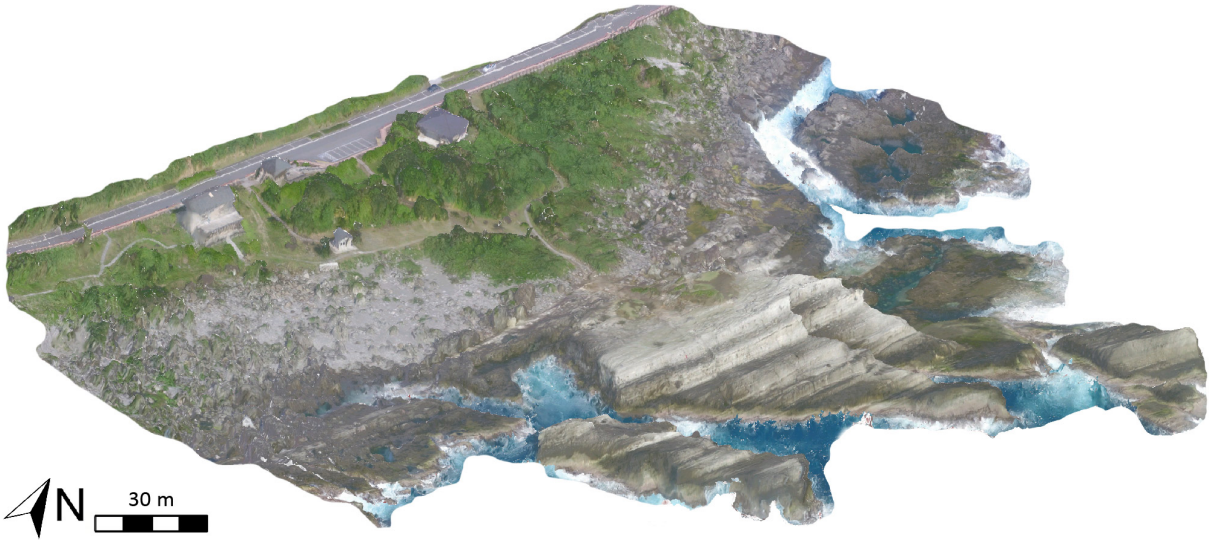

Figure 4.4: Virtual outcrop model of the Cuesta study area from UAV photos.

4.2.2 Merging images and georeferencing

Photos of good quality and distribution were merged together and georeferenced to create contiguous images of the deformation band networks. Depending on the number of photos, Adobe Photoshop and Agisoft Metashape were used to merge the photos (workflow used for photo merging can be found in Appendix IV). A prerequisite when using these types of software is that the photos are taken with a constant height and camera angle with good overlap. Agisoft Metashape can handle a large number of photos at the same time and provides geometrically corrected images with a uniform scale and high resolution. The program was applied to make orthomosaics for more extensive networks. A network consisting of fewer photos (ten or less) was stitched together in Adobe Photoshop. This is more efficient and gives better results for small networks. The models from the merged photos must be georeferenced before interpretation in a software. This is because camera images do not contain any GPS data. The models from Adobe Photoshop and Agisoft Metashape were georeferenced in the same way. First step is to import the models into Adobe Photoshop and to add reference points. Then the dimension between the reference points, pixels, and scale of the models is calculated. The calculated points and dimensions can then be uploaded and georeferenced using the georeferencing tool in QGIS. The orthomosaics were later used to make topological maps over the selected deformation band networks.

4.2.3 Topological analysis using QGIS and NetworkGT

Photos and orthomosaics of the selected deformation band networks are mapped and digitized with QGIS, an open-source Geographic Information System (GIS). The sampling, analysis, and spatial mapping of topological attributes was done in the QGIS plugin, Network GT (toolbox) described by Nyberg et al. (2018). Figure 4.5 shows the Network GT workflow from input data to spatial visualization of the networks.

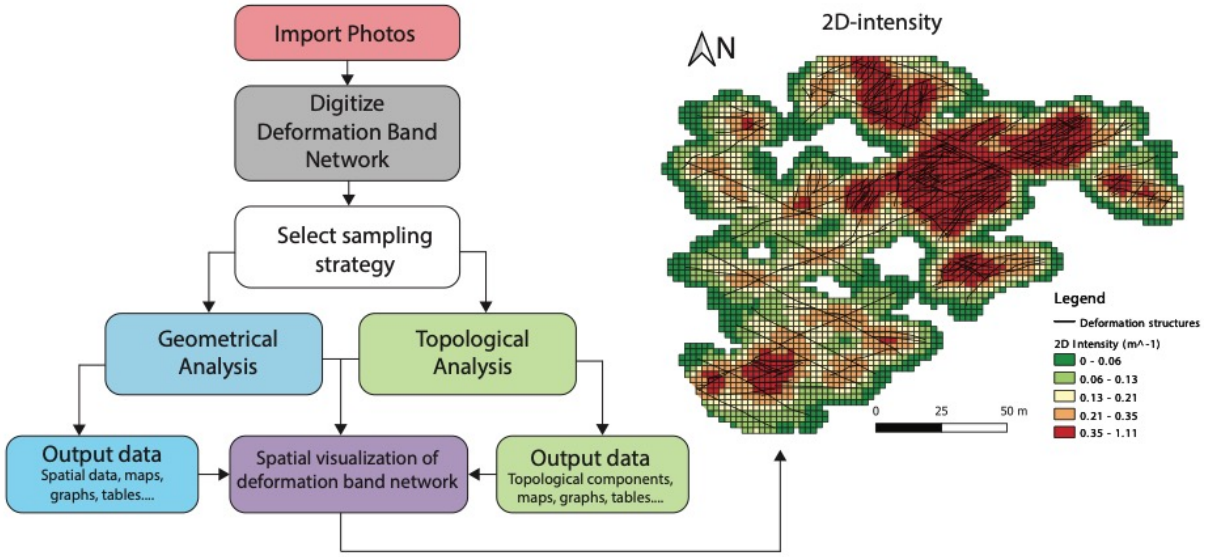

Figure 4.5: Flowchart showing the simplified NetworkGT workflow from input data to spatial visualization of the deformation networks. Modified from Nyberg et al. (2018).

Extracting topological and geometrical characteristics can be done, even with limited access to the deformation network as a whole (Sanderson and Nixon, 2015). The sampling strategy depends on the scale and the purpose of the analysis (Watkins et al., 2015). Collecting and quantifying topological data from deformation networks in the field can be difficult. Digitizing the networks is therefore often a preferred method for efficient topological and geometric data collection. All individual deformation bands or clusters were traced with a polyline. After all the deformation bands was interpreted and traced, a sample area polygon closes the area of interest. Areas covered with vegetation or processing errors are omitted from the sample area. Taking sub-samples of areas are possible by circle sampling or by creating new polygons over the area of interest. Applying the Repair Topology tool (Fig. 4.6A) after digitizing the networks helps resolve common topological errors. The Repair Topology tool automatically fixes inconsistent digitization like underlapping and overlapping of lines (Nyberg et al., 2018). To reduce the number of digitization errors, manual quality control is still required.

There are a several different ways to display the results of geometrical and topological analyses, e.g. triangular plots (showing the level of connectivity), different density maps, and line sampling/frequency plots (Sanderson and Nixon, 2015, Nyberg et al., 2018). The branches and Nodes tool (Fig. 4.6B) identify and extract branches (I-I, C-I, C-C) and nodes (I, Y, X) from the network. The extracted branches and nodes can be plotted in ternary diagrams for topological characterization (Fig. 4.2). The network grid sampling is done using the Contour Grid tool (Fig. 4.6C), which produces a map of the spatial variation within a deformation band

network. NetworkGT generates a square grid where the grid size and sample area are specified by the user. The grid cell size varies depending on the network and the level of detail desired. To avoid orientation bias, each cell in the grid consists of a center point with a circle drawn around it. From the network grid sampling, topological and geometrical variations within a deformation band network can be visualized. This is done through a series of intensity maps, such as 2D-intensity, connecting node frequency, and node distribution. The Line Grid tool (Fig. 4.6D) is used to extract data in one-dimension from a scanline. Deformation band frequency can be calculated by counting the deformation bands intersecting the line. This information can be imported to Excel to make graphs over the deformation band frequency across the entire network. To prevent under-sampling of deformation bands, the scanlines are oriented perpendicular to the trend of the deformation bands (Sanderson and Nixon, 2015, Nyberg et al., 2018). By combining topological and geometrical data, a wide range of information can be extracted, e.g. the average branch lengths in a network and connections per branch (connectivity in a network) (Sanderson and Nixon, 2015). All parameters, formulas, and abbreviations used are listed in Appendix I.

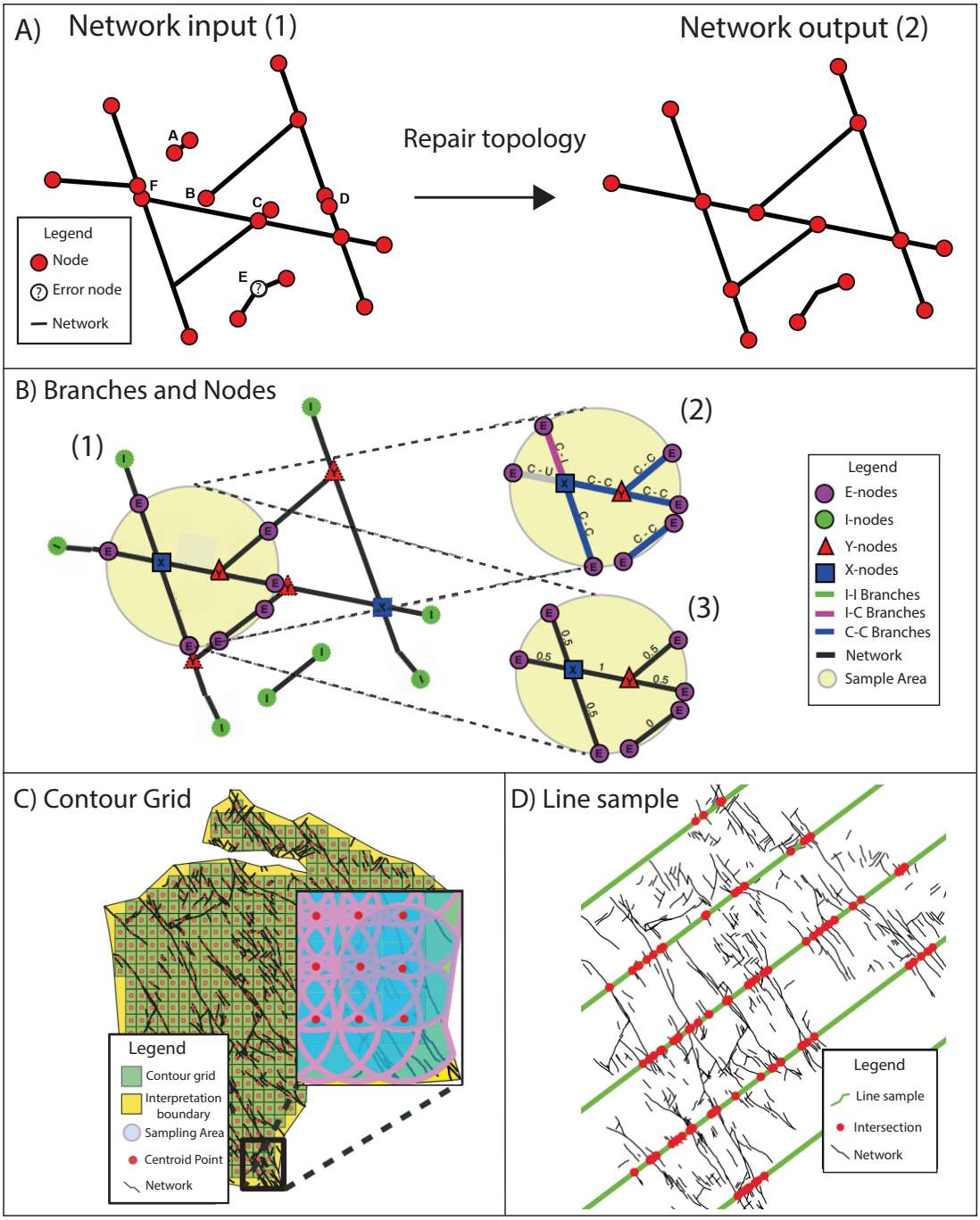

Figure 4.6: Overview of different tools in NetworkGT. A) Repair topology tool: (1) Network input with common topological digitizing errors. (2) Network output where the tool removes error nodes, extends and trims polylines. B) The branches and nodes tool. The nodes of the network are classified as isolated (I) or connecting (Y or X) nodes, in addition to edge nodes (E) that intersect the sample area. The branches are classified based on the nodes as isolated (I-I) branches with no connections, partly connected (C-I) branches with one connection, or fully connected (C-C) branches having two connecting nodes. Branches with E-nodes are counted as half branches. C) Contour Grid tool generates countless sub-samples of the network. Each grid cell has a circle sample area, where the size is defined by the user. D) The line grid tool generates lines across the network and count the number of intersections along the lines. Modified after Nyberg et al. (2018).

4.3 Uncertainties and sources of error

The topological interpretation of the UAV imagery has its limitations. The resolution allows structural mapping on meter-scale and does not distinguish deformation bands and brittle fractures. Therefore, mapping on a larger scale includes main structural lineaments and not only deformation bands. There are some uncertainties related to the close-up photos from the field. The outcrops are situated in a slightly tilted succession and are never completely horizontal. The photos can, to some extent, be angled or elevated in relation to each other. This can cause some uncertainties regarding the branch orientation and length and generate errors or gaps when merging images in Agisoft Metashape and Adobe Photoshop. However, no surface is in nature perfectly horizontal.

Digitization of the deformation band networks in QGIS can lead to sources of error in all types of images. The uncertainty is lower for the smaller models, due to higher quality and the limited area they cover. The sources of error increase with larger models, related to the quality of merging and the extent to which the deformation bands are exposed. The possibility of deformation bands being overlooked increases in the larger models, considering a large number of bands. Thin deformation bands can be difficult to see in the photos, depending on differences from the host rock. Areas covered with vegetation, sediments, or of low quality are omitted from the interpretation boundary. These gaps without data are seen as uncertainties as the continuation of the bands is not seen. Using the Repair Topology tool in NetworkGT, the quality of the deformation band digitization increases, but manual quality control should be done in addition. Thick clusters introduce the problem of several deformation bands, where it is difficult to determine the number of bands in the cluster. In such cases, only the outer edges of the cluster are traced. Furthermore, the data in this thesis only offers a 2D-analysis of the network, and the architecture and connectivity may vary in the subsurface.

5 Results

The studied volcaniclastic rocks host cataclastic deformation band networks, and the networks are of sinistral and dextral movement. A total of eleven deformation band networks have been studied in detail (Fig. 4.3). The deformation band networks were selected based on photo quality and their difference in nature. The deformation band network arrays range from incipient networks to deformation band networks in fully developed faults. Topological analyses of all networks were undertaken, which is an effective way of analyzing deformation band terminations (nodes) and connectivity. See Appendix II for full datasets of all topological and geometrical data.

5.1 Structures and stratigraphy of the study area

The study area comprises a well-exposed wave-cut platform in a tilted succession (26°) (Fig 5.1A). The studied lithology at Cuesta holds a variety of folded pyroclastic rocks and tuffs. Figure 5.1 shows the stratigraphy of the studied cross-section at Cuesta, and Figure 5.2 displays a stratigraphic log of the same succession. Song and Lo (2002) described the host rock in the study area, and their classification is adopted herein. The following volcaniclastic rocks have been recognized (Fig 5.1B-D): tuffaceous sandstone, ignimbrites and, polygenic conglomerate.

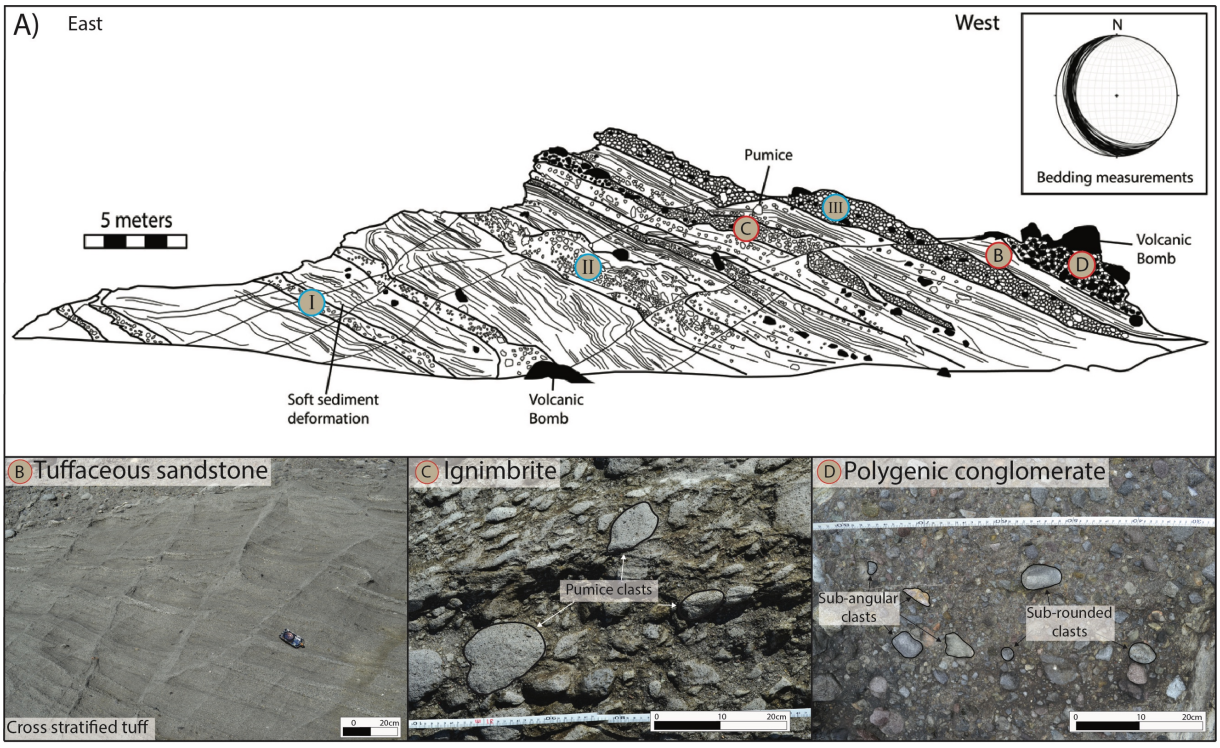

Figure 5.1: A) Illustration of the stratigraphy in the study area (Fig. 4.3). Rose diagram demonstrates the orientation of the tilted beds. Red circles correspond to the lithologies in B, C and D. Three reference layers marked with blue circles as (i), (ii) (iii) serve as correlation points between the stratigraphic log (Fig 5.2) and the outcrop illustration. Modified from Kjenes (2018). B) Tuffaceous sandstone with cross-stratification. C) Ignimbrite with white and greyish pumice clasts. D) Polygenic conglomerate with sub-angular to sub-rounded clasts.

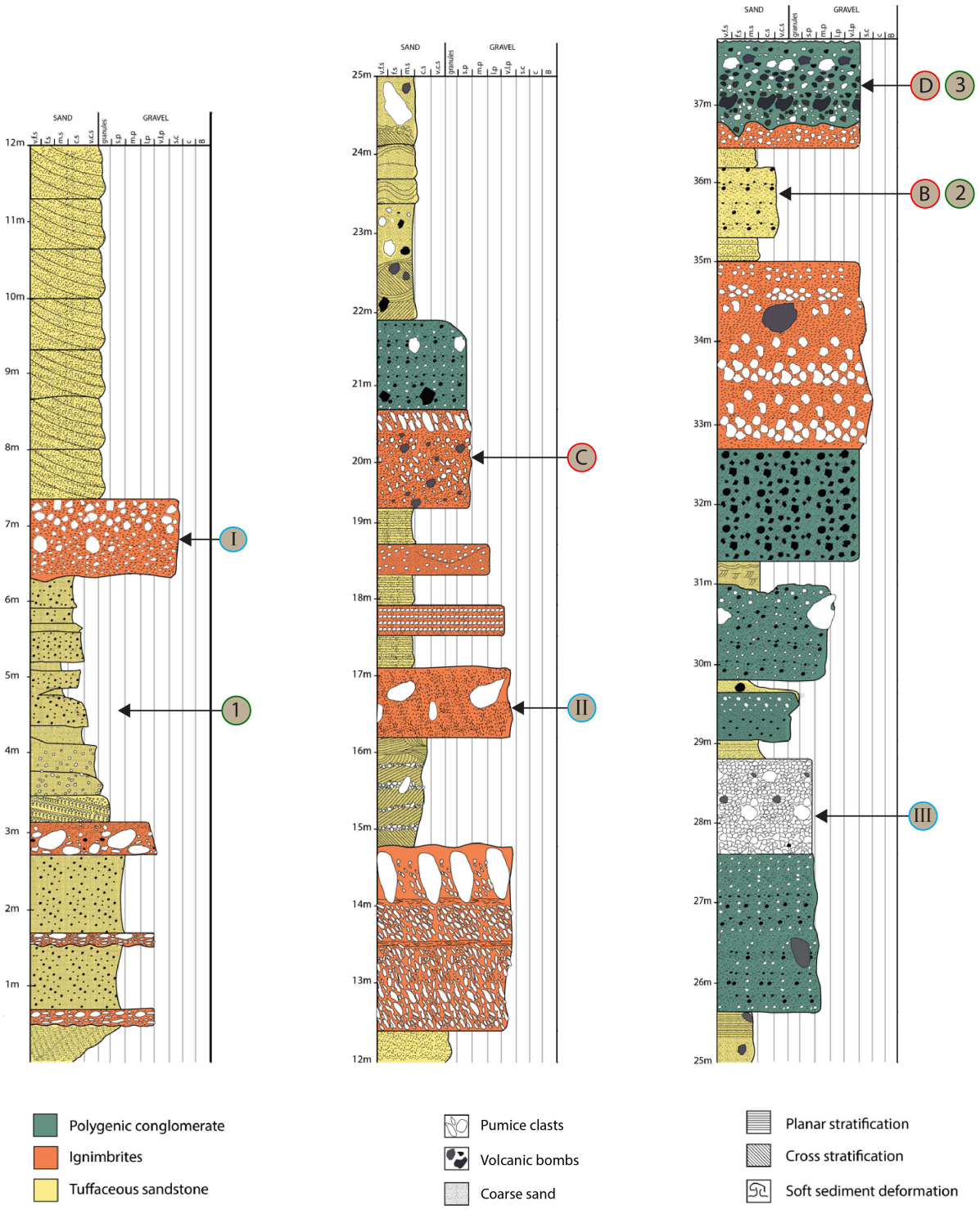

Figure 5.2: Stratigraphic log of the Shihtiping Tuff member. The stratigraphic log starts at the base of the outcrop (Fig 5.1A) in the east and continues stratigraphically up section towards the west. Modified after Kjenes (2018). Blue circles marked with (i), (ii), (iii) correspond to reference layers in Figure 5.1A. Red circles marked with B, C, D correspond to the lithologies shown in Figure 5.1A. Green circles marked with 1, 2, 3 correspond to deformation band geometry in Figure 5.3.

The Cuesta study area is situated within the Tuluanshan Formation. Stratigraphical logging (Fig. 5.2) of the study area has been carried out earlier through Martin Kjenes and Hanna Serina Jervidalo's master theses (Kjenes, 2018, Jervidalo, 2018). Description of the host rocks in the study area is based on Kjenes (2018) and Jervidalo (2018) findings, in addition to the study by Song and Lo (2002).

Tuffaceous sandstone (Fig. 5.1B) is fine- to coarse-grained and contains a variety of sedimentary structures (e.g. planar stratification, cross stratification, soft sediment deformation features). The tuffaceous sandstone units in the studied succession show thicknesses of 10 - 30 cm, but thicker units interbedded with ignimbritic material are observed. Song and Lo (2002), Kjenes (2018), and Jervidalo (2018) interpreted the tuffaceous sandstone to consist of crystal tuff due to larger amounts of magmatic minerals and lithic fragments. ***Ignimbrites*** (Fig. 5.1C) are recognized by their abundance of white (mostly) and grey pumice clasts. The thickness of the ignimbrite layers varies from 10 cm to several meters. The clasts can be as large as 64 cm, but generally around 5 - 15 cm. The pumice clasts are matrix-supported by coarse tuffaceous sandstone. It is not uncommon with thin layers of sandstone in-between the ignimbrite units. ***Polygenic conglomerate*** (Fig. 5.1D) consists primarily of sub-angular to sub-rounded clasts between 3 - 12 cm of lapilli origin. Larger volcanic bombs and pumices over 12 cm occur locally. The polygenic conglomerate appears in centimeters to meters thick layers. The conglomerate is mostly clast supported, with a matrix of tuffs.

5.1.2 The geometry of deformation bands at Cuesta

The deformation bands may occur as individual bands but more common as clusters and networks (Fig. 5.3). The thickness of the deformation bands varies depending on the lithology. Single deformation bands vary from 0.3 to 10 mm in thickness but rarely exceed 3 mm. Clusters (Fig. 5.3C) of deformation bands range in thickness from 5 mm to 8 cm. The presence and thickness of deformation bands can change abruptly along the strike when entering a new host rock. Clusters can link up or spread to networks in the transition to a new host rock. Common characteristics for the studied deformation bands are connecting structures, as ramp- and eye structures (Fig. 5.3C). Ramp structures form a step-like pattern between parallel overlapping segments, while eye structures form between two closely collinear segments (Antonellini and Aydin, 1994). A network of linked deformation bands tends to form an anastomosing pattern and can, together with ramp and eye structures, be recognized at different scales.

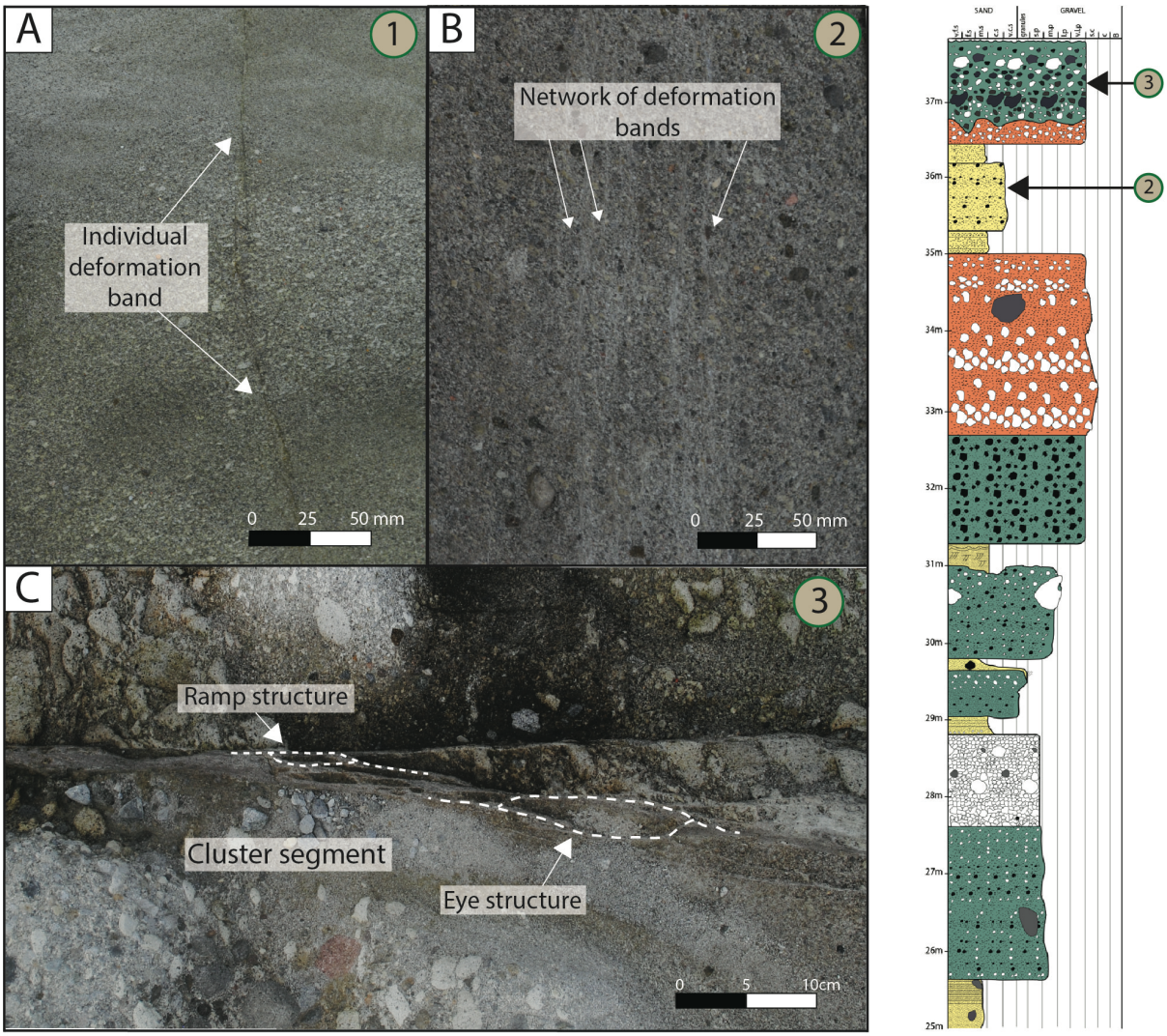

Figure 5.3: Overview of the geometry of the deformation bands at Cuesta. Green circles marked 1, 2, 3 correspond to the location in the stratigraphic log (Fig 5.2). A) Individual deformation band. B) Network of deformation bands. C) Clusters of deformation bands. Ramp structures and eye structures forms when deformation band segments link up.

5.2 Structural overview: Geometry and topology

The study area consists of a folded succession with NNE striking folds. The sample area covers about 11855 m^2. Deformation bands and faults are distributed widely in the study area (Fig. 5.4). Observable deformation structures (deformation bands and faults), both dextral (0° - 90°) and, sinistral (90° - 180°) are shown in Figure 5.4 and, their orientations are plotted in a rose diagram. There is greater variation in the orientation of the dextral structures (30° - 80°) than the sinistral structures (110° - 120°).

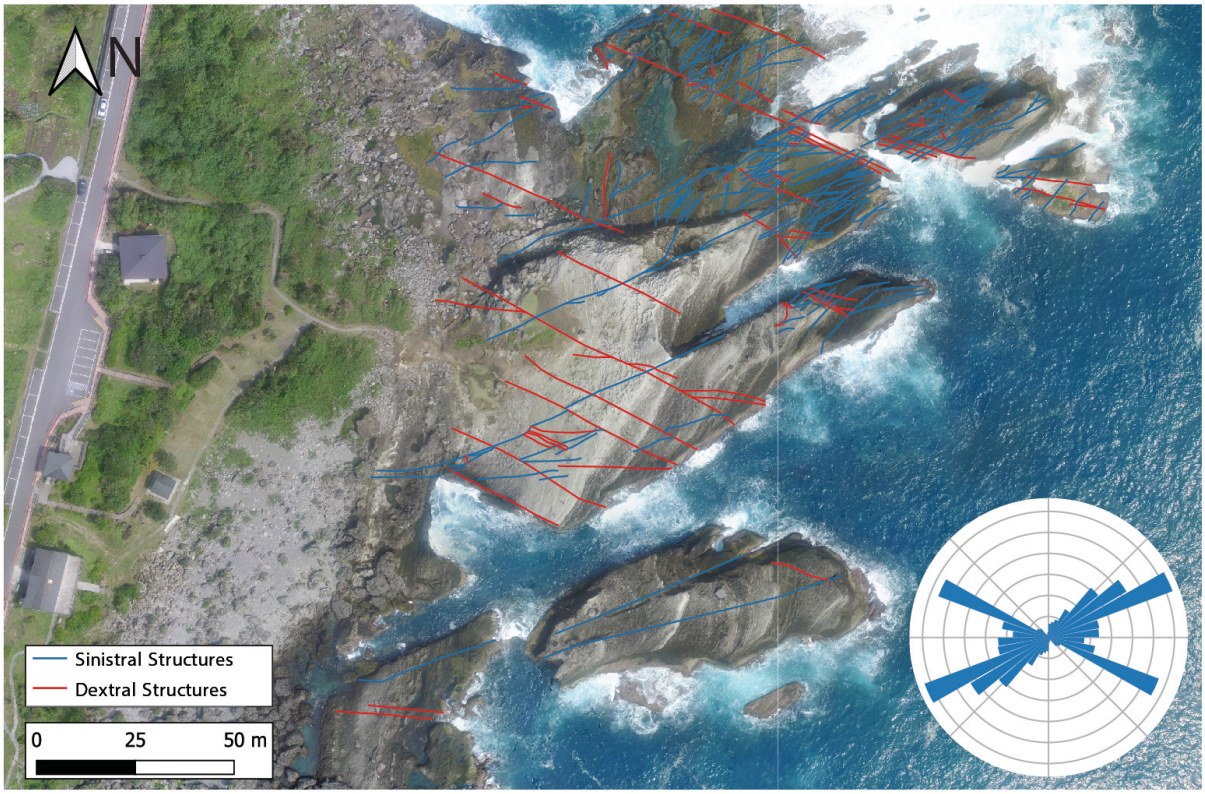

Figure 5.4: UAV imagery of the study area. Observable structural lineaments are outlined. Sinistral and dextral structures are marked in red and blue, respectively. The rose diagram shows two dominating trends, ENE-WSW oriented for the sinistral structures, and WNW-ESE oriented for the dextral structures.

The majority of the structures are situated NE in the study area. The nodal plot (Fig 5.5E) illustrates a relatively even distribution of nodes. 284 I-nodes, 157 Y-nodes, and 136 X-nodes, excluding an additional 51 edge nodes (E-nodes). Note the high proportion of X-nodes, compared to deformation band networks further in this chapter. The branch plot (Fig 5.5F) reveals that the study area is dominated by partly connected (C-I) branches, with one connection per branch, and fully connected (C-C) branches, with two connecting nodes per branch.

Contour plots of 2D-intensity, connecting node frequency (Y-nodes and X-nodes), and X-nodes are used to visualize the spatial variation of deformation structures at the Cuesta (Fig. 5.5). The 2D-intensity (Fig. 5.5B) varies from 0.12 to 1.11 m^{-1}, connecting node frequency from 0.01 to 0.2 m^{-2}, and number of X-nodes from 2 to 13. Areas with a high 2D-intensity and high connecting node frequency (Fig. 5.5C) commonly consist of several small branches that interact, while areas with a lower intensity and frequency usually consist of longer branches. At Cuesta, there is a clear connection between 2D-intensity and connecting node frequency, which indicates a higher number of connecting nodes in high-intensity areas (Fig 5.5B and C). The intensity distribution of X-nodes (Fig. 5.5D) displays a similar trend as 2D-intensity (Fig. 5.5B) and connecting node frequency (Fig. 5.5C). The structures at Cuesta have an average

connection per branch of 1.56, where the maximum degree of connectivity is 2 (Nyberg et al., 2018).

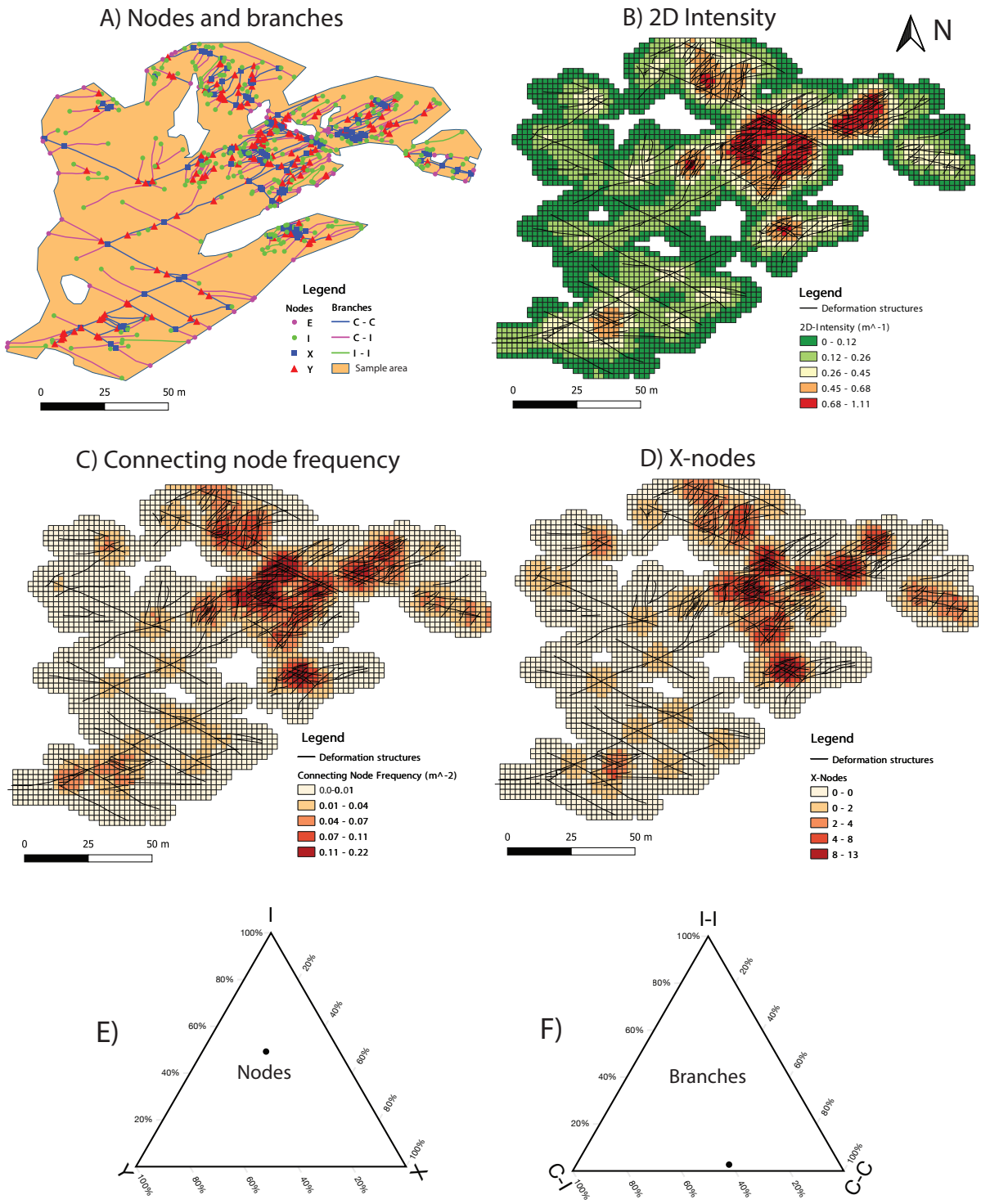

Figure 5.5: Observable deformation structures (deformation bands and faults) and various contour maps. Note a clear connection between 2D-intensity and connecting node frequency. A) Observable structural lineaments classified into branches and nodes. B) 2D-intensity (m^{-1}) variation. C) Connecting node frequency (m^{-2}). D) Number of X-nodes. E) and F) Distribution of nodes and branches for Cuesta, node classification plotted on an I, Y, and X ternary diagram, and branch classification plotted on an I–I, C–I, and C–C ternary diagram.

5.3 Geometry and topology of deformation band networks

The deformation band networks vary in distribution, thickness, and the number of bands in the network. The studied length of the networks is between 2 and 14 m along the strike, and the thickness varies from 15 to 61 cm. The deformation bands in the studied networks are generally light-colored relative to the host rock.

The deformation band networks occur in different stages, from fully developed faults, mature networks and, incipient deformation band networks (Jervidalo, 2018). The structural behavior of the faults is affected by local lithology, where the faults are dominated by deformation bands or by brittle deformation (slip-surfaces and shear fractures). Strike-slip faults are distinguished from mature deformation band networks based on larger displacements (>50 cm) (Jervidalo, 2018). This thesis targets deformation bands occurring in the studied outcrops. Fractures and faults are mainly described for context. The orientation, deformation band intensity and connecting node frequency have been calculated for all networks. In addition, one deformation band network (deformation band network SN-4) was analyzed at various scales to document potential inconsistencies caused by variable resolution.

Out of eleven studied deformation band networks, eight have been selected for showcase in this chapter: two deformation band networks in fully developed faults, four mature deformation band networks and two incipient deformation band networks (Table 5.1). The remaining data can be found in Appendix II and III.

Table 5.1: Names and abbreviations of investigated deformation band networks in this thesis.

Type of deformation band network			
In fully developed faults		Mature deformation band network	Incipient deformation band network
Fault 1	Section 1.1	DN-2 (Dextral network 2)	IDBN1 (Incipient deformation band network 1)
	Section 1.2	DN-3 (Dextral network 3)	
Fault 2	Section 2.1	SN-1 (Sinistral network 1)	IDBN2 (Incipient deformation band network 2)
	Section 2.2	SN-4 (Sinistral network 4)	

5.3.1 Deformation band networks in fully developed faults

Fully developed faults have a relatively clear and consistent fault core (sensu Caine et al., 1996). Two sinistral, ENE-WSW trending faults (Fig. 5.6A) have been mapped in the study area, feature offsets ranging from 0.5 m to 2.6 m. The faults are associated with one or more continuous slip-surfaces accommodating shear displacement. A distinct damage core (sensu Caine et al., 1996, Peacock et al., 2017) is present in some lithologies, while less defined or not fully developed in others.

Fault 1, the northern fault (Fig. 5.6A) is situated on the top of the wave-cut platform at the Cuesta. The fault has a total trace length of 33 m, with a maximum shear displacement of 1.83 m and a minimum of 1.20 m (Jervidalo, 2018). The fault core ranges from 3.1 cm to 45.6 cm. The deformation band systems are divided into two sections (Section 1.1 and Section 1.2) to ensure high quality of the studied deformation band networks. Section 1.1 (Fig. 5.6Ci) covers 1.71 m of Fault 1 and is dominated by thick clusters in SE covering the entire fault core. The cluster thickness is between 1.5 and 8.1 cm, which is relatively thick compared to clusters in other networks examined in this thesis. According to Shipton and Cowie (2001) classification, the cluster in Section 1.1 is a class 3 cluster, defined as a complex anastomosing slip-surface with many single and multi-strand deformation bands (Fig. 5.6F). Further along the fault, the clusters splay out as a network of deformation bands.

Section 1.2 (Fig. 5.6Cii) is a continuation of Section 1.1 (Fig. 5.6Ci) and extends 2.45 m along Fault 1. In total, 4.16 m of the fault has been examined in detail. Section 1.2 starts in SE as a network of deformation bands and has a variable geometry towards NE. Most of the deformation bands are concentrated around the fault core, as clusters or networks of bands. Individual bands are observed outside the defined core, but occur infrequently. The orientation of Section 1.1 and 1.2 is plotted in a rose diagram (Fig. 5.6B), showing a clear ENE-WSW trend for the deformation bands, parallel to the fault. A digitized map of the deformation band network can be seen in Figure 5.7 and Figure 5.8.

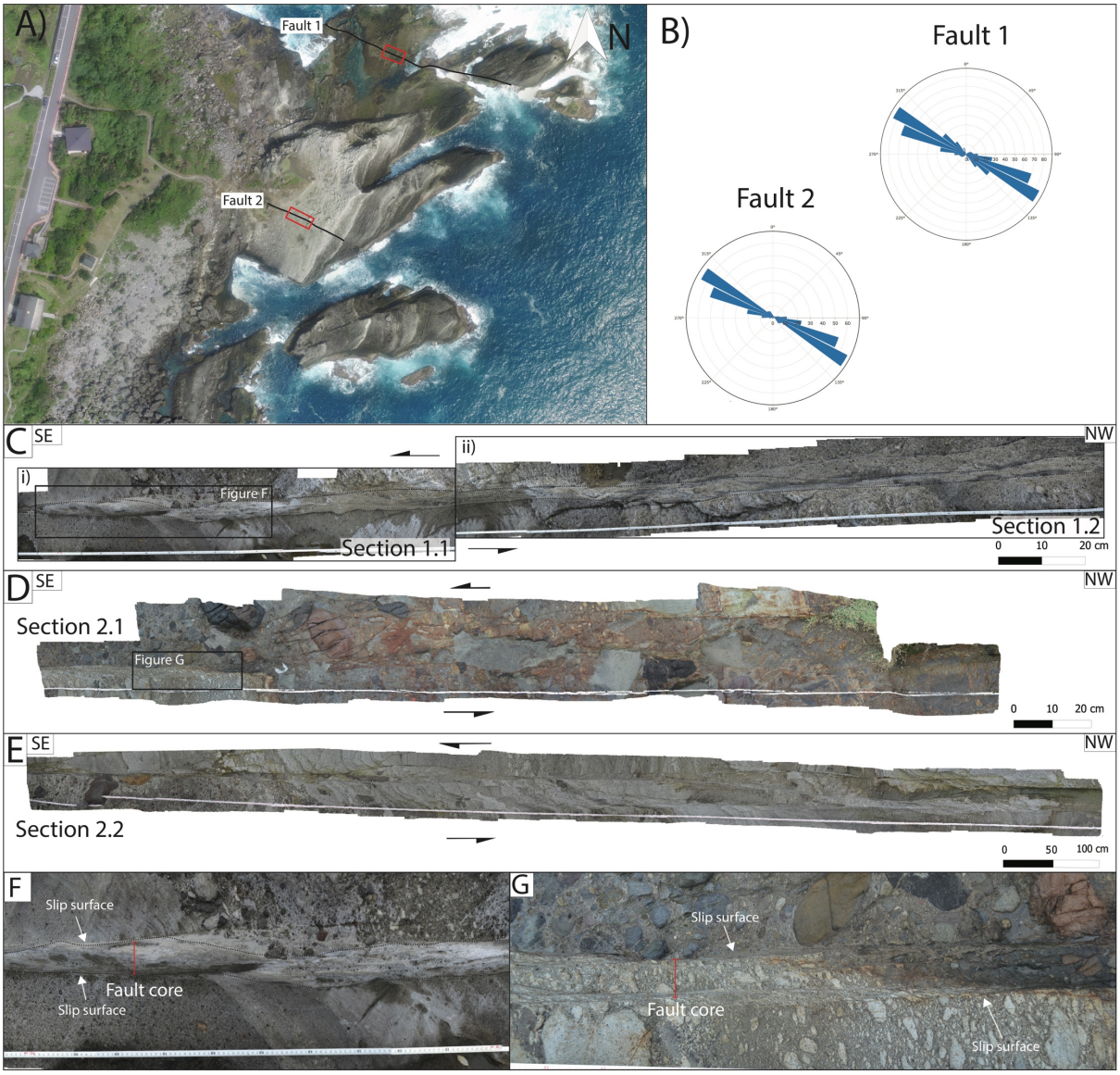

Figure 5.6: Overview figure of Fault 1 and Fault 2. A) Unmanned Aerial Vehicle (UAV) photo of the study area. Fault 1 (northern fault) and Fault 2 (southern fault) are marked as black lines, red boxes indicate where the close-up photos were taken. B) Rose diagram showing deformation band orientations of Fault 1 and Fault 2. C) Close-up photos of Fault 1 divided into Sections 1.1 (Ci) and 1.2 (Cii). Arrows are showing the sinistral movement. D) Close-up photos of Fault 2, Section 2.1. E) Close-up photos of Fault 2 Section 2.2. F) Class 3 cluster from Section 1.1, with tightly packed deformation bands and anastomosing slip-surfaces G) Class 3 cluster from Section 2.1.

The deformation band network of Fault 1 is presented together with the connecting node frequency maps, 2D-intensity maps, and graphs illustrating the deformation band frequency in Figure 5.7 and 5.8. Note the different values for connecting node frequency and 2D-intensity for Sections 1.1 and 1.2. The thick cluster in Section 1.1 can be recognized in both the 2D-intensity map (Fig. 5.7D) and the connecting node frequency map (Fig. 5.7C) as an area of higher deformation band intensity and connecting node frequency, respectively. However, the cluster does not stand out in the deformation band frequency plot (Fig. 5.7E). A clear correlation is recognized between the 2D-intensity and the fault core in Fault 1, shown as a high-intensity

zone (Fig. 5.7D and Fig. 5.8D). The fault core has a maximum 2D-intensity of 14958 m^{-1} in Section 1.1 and 3891 m^{-1} in Section 1.2. The connecting node frequency maps present a similar trend as the 2D-intensity maps, where the highest connection is observed in the fault core.

The southern fault (Fault 2, Fig. 5.6) has a total trace length of 37 m, with a maximum shear displacement of 2.60 m and a minimum of 1.70 m (Jervidalo, 2018). The fault core shows a thickness between 3.5 and 53.5 cm. Two sections (Section 2.1 and Section 2.2) are examined in detail and displayed in Figure 5.9 and 5.10. Both sections consist of individual deformation bands, clusters, and networks of bands. The two sections show a variable structural style of the fault.

Section 2.1 consists of one main segment in SE (Fig. 5.9), concentrated around the fault core, and splits out into two segments towards NW. Several fractures and minor slip-surfaces are widely distributed within the section. The deformation band network in Section 2.1 is 6.2 m in length and 61 cm in width. The deformation bands in SE occur as clusters or networks of bands and are mainly concentrated in the fault core. Individual bands occur occasionally. Using the classification from Shipton and Cowie (2001), the cluster is classified as a class 3 cluster (Fig. 5.6G). Towards NW, the network spread, and the fault core is less defined. The deformation bands in Section 2.1 vary in thickness from 3 to 10 mm, and the bands form clusters in centimeter-wide zones. The deformation band network morphology is recognizable in the connecting node frequency map and 2D-intensity map (Fig. 5.9). The main segment in SE has a high total branch length per square meter, referring to a higher connecting node frequency. The highest peak in the deformation band frequency plot (Fig. 5.9E) corresponds to a delimited area with fine tuffaceous sandstone.

Section 2.2 (Fig. 5.10) shows a different structural style than Section 2.1, where the deformation band is widely disrupted throughout the section. The network covers an area of 2.6 m^2 and consists of networks of bands, with individual clusters in NW. The thickness of the individual deformation bands within the network can be as thick as 10 mm, with a network width extending 50 cm. Towards NW, it is an area where two segments link together, characterized by a high deformation band intensity. A clear correlation is recognized between the linked area and the peak in the deformation band frequency plot (Fig. 5.10E). The connecting node frequency map has a positive correlation to the 2D-intensity map, with the highest connection where segments are linked together.

The compiled data for branches and nodes for Fault 1 and Fault 2 is presented in Figure 5.11. Fault 1 has a total of 955 nodes and 1125 branches with a high proportion of isolated nodes (39.7%) and connected Y-nodes (57.2%). A result of this is a deformation band network consisting mainly of partly connected (C-I) and fully connected (C-C) branches. The average connection per branch is relatively low with a connectivity of 1.64 C_b. There is not a significant difference between the distribution of nodes and branches in Section 1.1 and 1.2 (Fig. 5.11).

Fault 2 consists of 1232 nodes and 1575 branches and is dominated by connecting Y-nodes (70.86%) and fully connected (C-C) branches (Fig. 5.11). This combination results in a higher connectivity than Fault 1, with an average connectivity of 1.71 C_b. The lowest connectivity is measured in Section 2.1 at 1.55 C_b, reflecting low connectivity compared to the rest of the network in Fault 2. Section 2.1 also displays the highest proportion of I-nodes at 46.1%. Nevertheless, Section 2.2 has high connectivity (1.89 C_b) which results in high average connectivity for the network in Fault 2 as a whole. An overall low proportion of X-nodes has been observed in both Fault 1 and Fault 2 (Fig. 5.11).

A positive correlation is observed comparing the triangle diagrams in Figure 5.11 and the connecting node frequency map for Fault 1 (Fig. 5.7C and Fig. 5.8C). The network in Fault 1 has connecting nodes that extend across the entire studied area. A moderate positive correlation is recognized in the connecting node frequency map for Fault 2, where there is a patchier composition of connecting nodes.

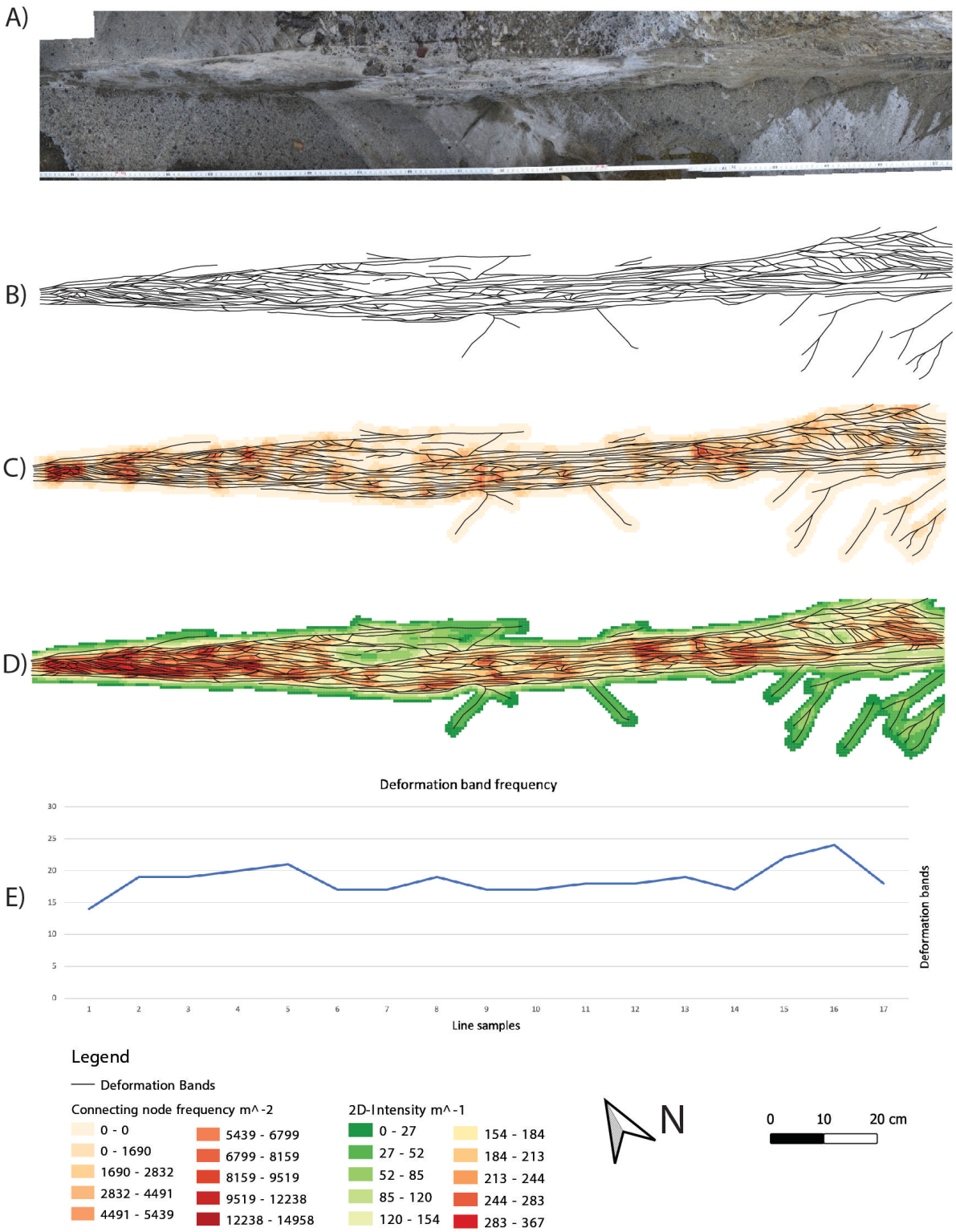

Figure 5.7: Deformation band network along Section 1.1 (Fault 1), with frequency graph and different contour maps. A) Close-up photo of Section 1.1, shown in Figure 5.6Ci. B) Digitized deformation band network of Section 1.1. C) Connecting node frequency map (m^{-2}). D) 2D-intensity map (m^{-1}), intensity variation within Section 1.1. E) Deformation band frequency plot, displaying the variation of deformation bands across Section 1.1 A line sample was taken every 10 cm along the entire Section 1.1.

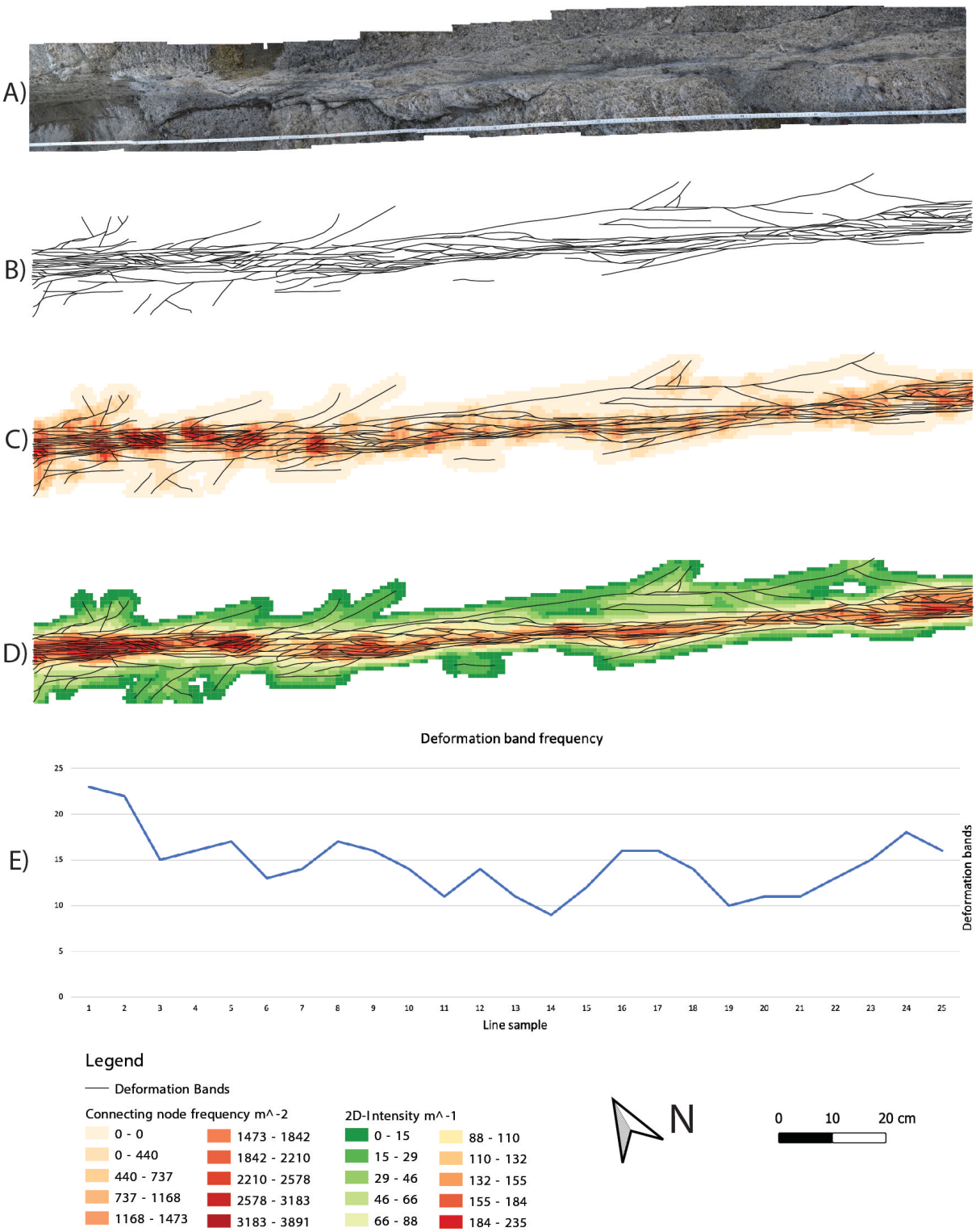

Figure 5.8: Deformation band network along Section 1.2 (Fault 1), with frequency graph and different contour maps. A) Close-up photo of Section 1.2, shown in Figure 5.6Cii. B) Digitized deformation band network of Section 1.2. C) Connecting node frequency map (m^{-2}). D) 2D-intensity map (m^{-1}), intensity variation within Section 1.2. E) Deformation band frequency plot, displaying the variation of deformation bands across Section 1.2. A line sample was taken every 10 cm along the entire Section 1.2.

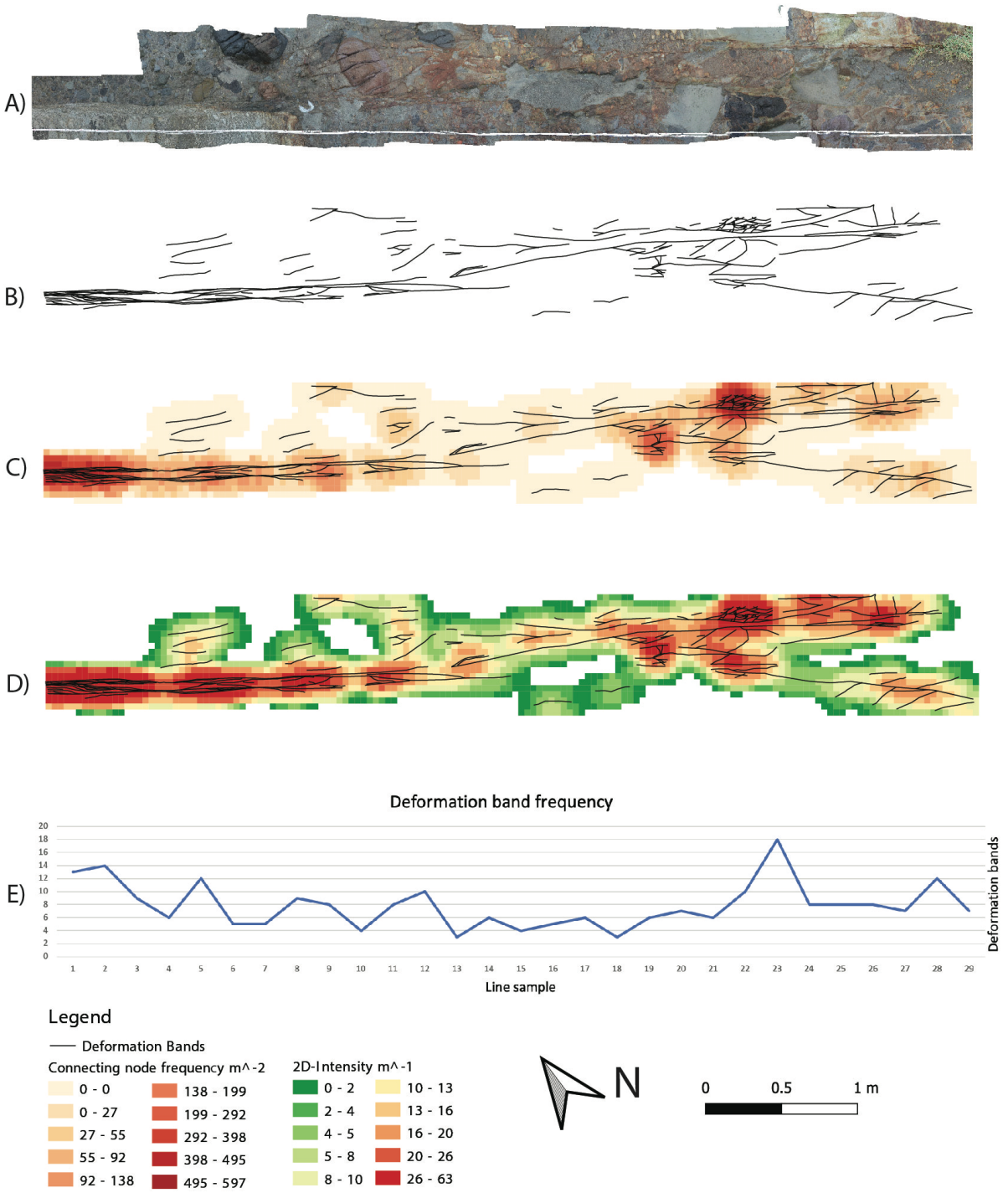

Figure 5.9: Deformation band network along Section 2.1 (Fault 2), with frequency graph and different contour maps. A) Close-up photo of Section 2.1, shown in Figure 5.6D. B) Digitized deformation band network of Section 2.1. C) Connecting node frequency map (m^{-2}). D) 2D-intensity map (m^{-1}). E) Deformation band frequency plot, displaying the variation of deformation bands across Section 2.1. A line sample was taken every 20 cm along the entire Section 2.1.

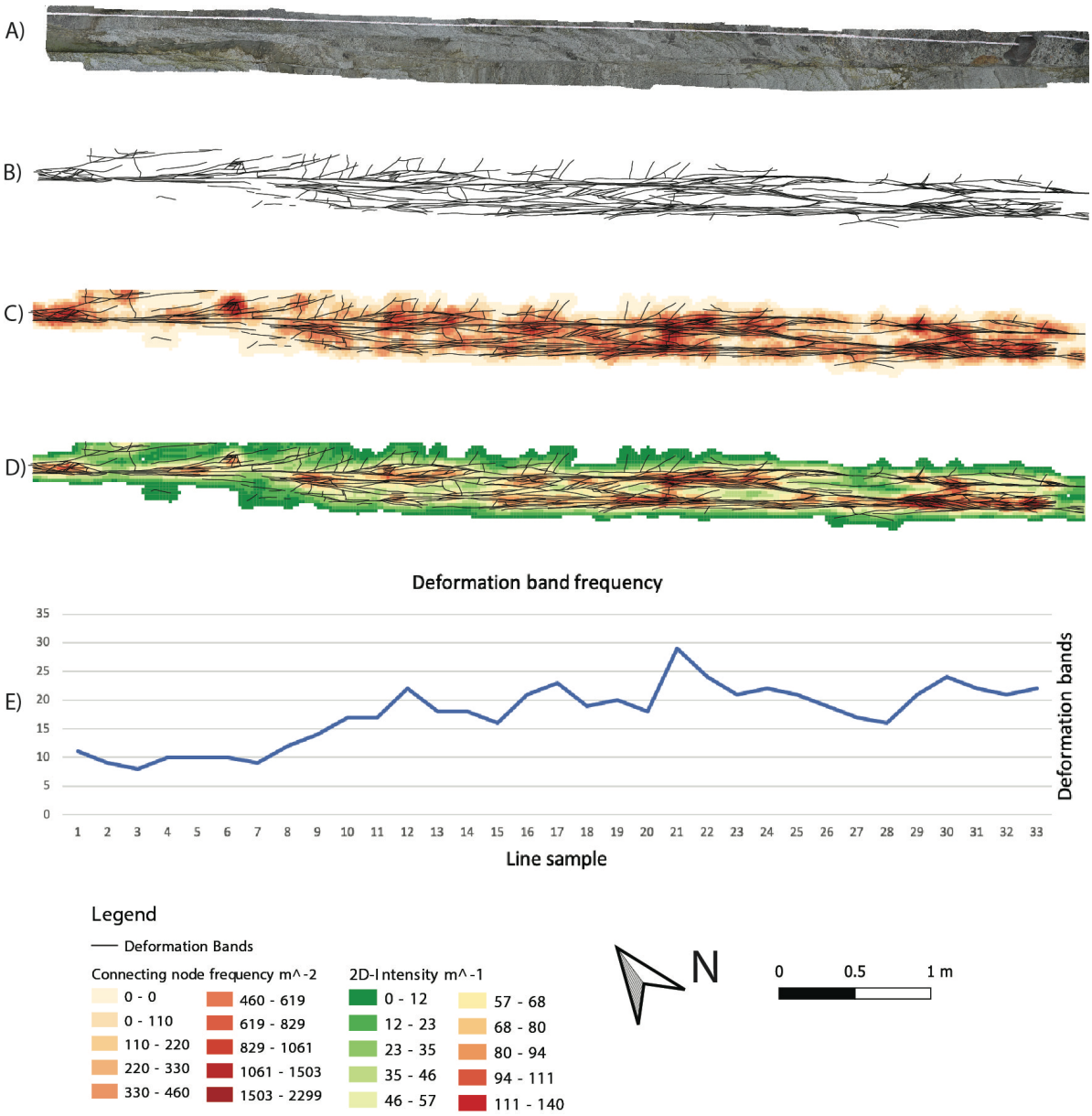

Figure 5.10: Deformation band network along Section 2.2 (Fault 2), with frequency graph and different contour maps. A) Close-up photo of Section 2.2, shown in Figure 5.6E. B) Digitized deformation band network of Section 2.2. C) Connecting node frequency map (m^{-2}). D) 2D-intensity map (m^{-1}). E) Deformation band frequency plot, displaying the variation of deformation bands across Section 2.2. A line sample was taken every 20 cm along the entire Section 2.2.

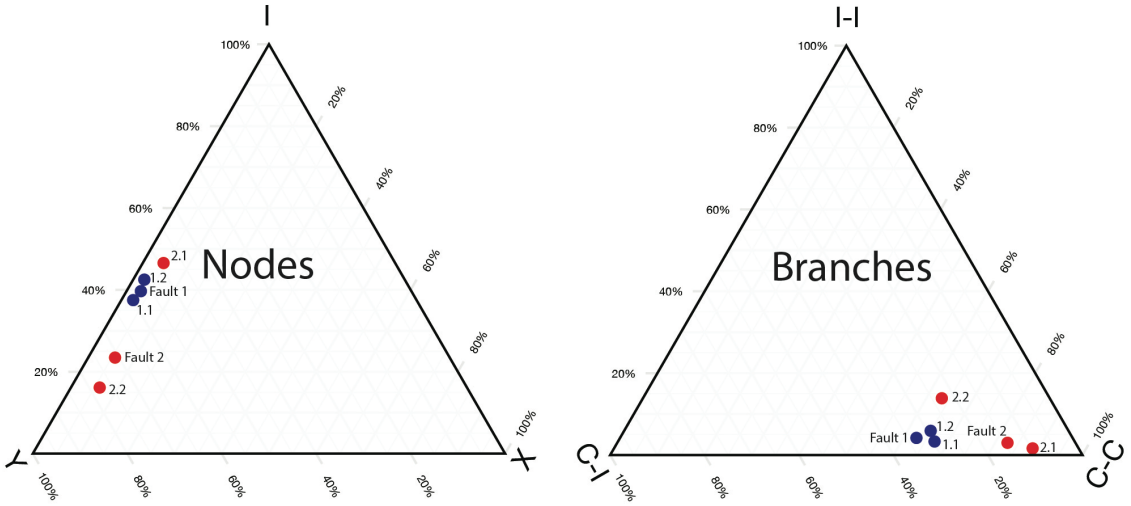

Nodes	Fault 1 ●	Fault 2 ●
I - Nodes	379	289
Y - Nodes	547	873
X - Nodes	29	70
Total	955	1232
Branches		
I - I	47	47
C - I	372	226,5
C - C	706	1301,5
Total	1125	1575

Figure 5.11: Ternary plot displaying the node and branch distribution of Fault 1 (Section 1.1 and 1.2) in blue and Fault 2 (Section 2.1 and 2.2) in red. The table shows the number of nodes and branches in Fault 1 and Fault 2, respectively.

5.3.2 Mature deformation band networks

Mature deformation band networks generally comprise clusters and interconnected networks of bands, where individual bands can occur in association to the networks. Mature networks consist of both sinistral (SN) and dextral (DN) networks, with an orientation of 0° - 90° and 90°- 180°, respectively. The studied length of the mature deformation band networks is between 1.8 and 11.2 m. Well exposed networks of high quality are described below: two dextral networks (DN-2 and DN-3) and two sinistral networks (SN-1 and SN-4).

Deformation band network DN-2

Deformation band network DN-2 exhibits a dextral shear movement and is located towards the center of the study area, close to SN-2 and SN-3 (Fig. 4.3). The succession comprises three lithologies: polygenic conglomerate, tuffaceous sandstone, and ignimbrites. The network measures 2.1 m in length and a width between 2 and 50 cm (Fig. 5.12) and includes individual bands, clusters, and networks of bands. Deformation bands are present throughout the succession, but their intensity and thickness vary by lithology (Fig. 5.12C). Individual

deformation bands have a thickness of c. 2 mm, while clusters can become as thick as 2 cm. The morphology of the network changes throughout the succession. The network starts as four individual bands in the polygenic conglomerate, develops as a cluster in the tuffaceous sandstone unit, and spreads as a network with as many as 12 bands in the ignimbrite unit. Total cumulative thickness in the different lithologies is measured in line 2, 5, and 9 (Fig. 5.12C), with respectively 2.9 cm in the polygenic conglomerate, 4.2 cm in the tuffaceous sandstone, and 29.7 cm in the ignimbrite.

The majority of the deformation bands are oriented NW. The bands are not evenly distributed within the network and show great variation in the studied succession (Fig. 5.12). Line samples (Fig. 5.12D) reveal an increase in deformation band frequency towards SE. Although DN-2 shows greater total thickness in the ignimbrite unit compared to the tuffaceous sandstone, the deformation band frequency does not change significantly. There is a clear correlation between deformation band intensity and connecting node frequency, meaning a higher amount of connecting nodes in high-intensity areas. The greatest variety is found in the ignimbrite unit, where deformation band intensity is high (102 - 169 m^{-1}) at the beginning of the unit and gradually decreases as the network spreads. The connecting node frequency follows a similar trend (Fig. 5.12B).

Figure 5.13 shows the distribution of nodes and branches in the network. The network has 162 nodes and 184 branches and has a relatively high number of I-nodes and fully connected (C–C) branches. Considering the high number of I-nodes, the network's average connections are moderate, with a connectivity of 1.67 C_b (average connections per branch).

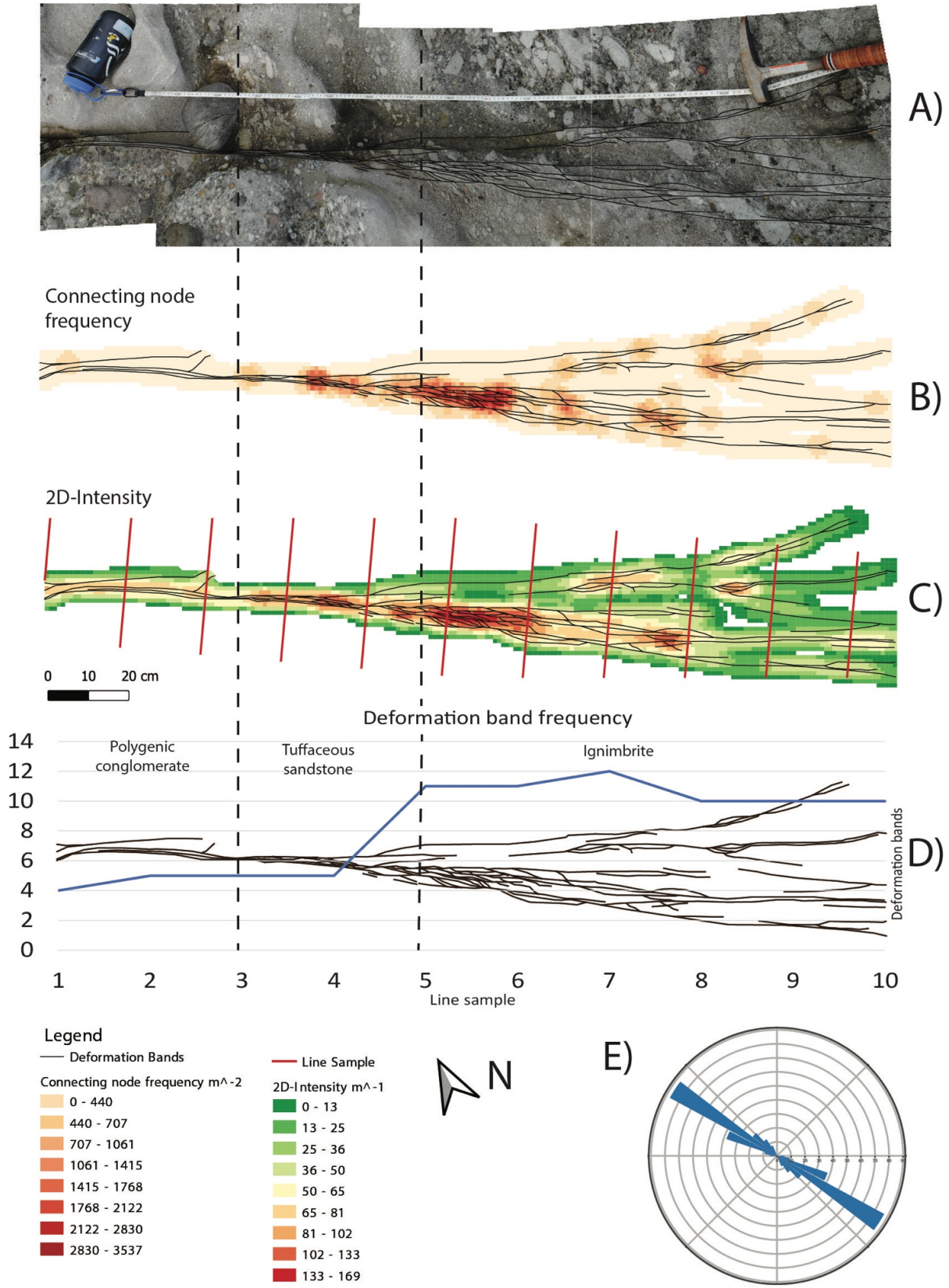

Figure 5.12: Outline of deformation band network DN-2 and different contour maps, graphs and rose diagram displaying topological and geometrical characteristics. The location of DN-2 is shown in Figure 4.3 A) The DN-2 deformation band network. B) Connecting node frequency. C) 2D-intensity map, intensity variation within the deformation band network. Line sample, counting deformation bands intersecting the line (red). D) Deformation band frequency plot, displaying the variation of deformation bands across the network. E) Rose diagram presenting the orientation of the deformation bands.

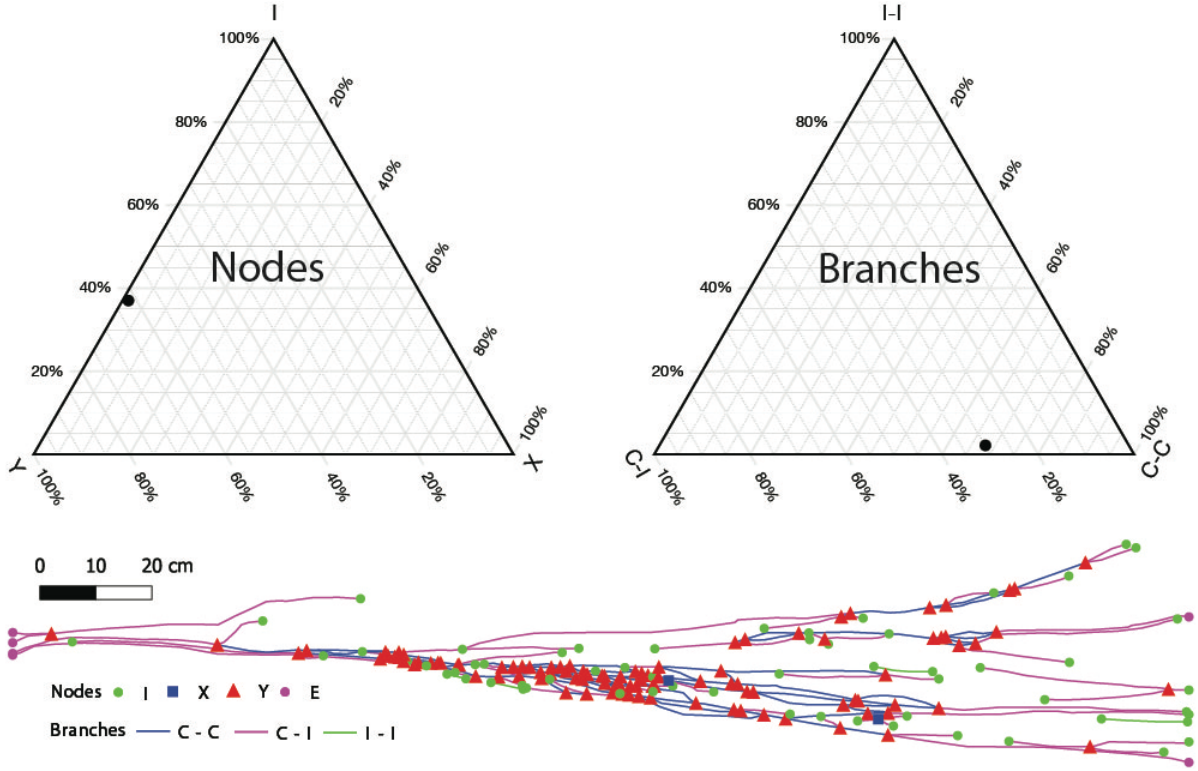

Figure 5.13: Ternary plots showing node and branch distribution in DN-2, based on the underlying network.

Deformation band network DN-3

Deformation band network DN-3 is located south of Fault 2 in connection to SN-4 (Fig. 4.3). The majority of the deformation band in DN-3 is oriented ENE - WSW (Fig. 5.14D). The section comprises tuffaceous sandstone, ignimbrites, and polygenic conglomerate. The network is 4.6 m long, with varying width depending on lithology (Fig. 5.14A). The network's morphology changes throughout the succession. The network starts as a wide network of bands in the tuffaceous sandstone in NE and narrows towards the SW. Total cumulative thickness is measured in the different lithologies (Fig. 5.14C), with 33.7 cm in the tuffaceous sandstone (line 4), 13.2 cm in the ignimbrite (line 11), and 8.9 cm in polygenic conglomerate (line 17). The bands thickness is approximately the same over the whole network (0.5 - 0.8 mm). Thicker clusters (≤1 cm) are only observed in the ignimbrite unit.

The 2D-intensity is mainly less than 40 m^{-1} with higher values restricted to the ignimbrite unit (Fig. 5.14C). The connecting node frequency is between 0 m^{-2} and 619 m^{-2}. The maximum values are recorded in the ignimbrite unit (Fig. 5.14B). Overall, there is significant variation in deformation band intersecting the lines samples (Fig. 5.14E), where the number varies from 2 to 10 intersections. The lowest number of bands is found in line 14 in the polygenic

conglomerate unit, with only two intersections. In comparison, the highest number of bands is found in line 12 in the ignimbrite unit with ten intersections. The number of intersections in the ignimbrite unit is overall high, but there is great variation along the network. The node and branch data (Fig. 5.14F) shows a network dominated by Y-nodes and fully connected (C-C) branches. A low proportion of I-nodes and I-I branches has been noted. Considering that a branch can maximum have two connecting nodes, the network's average connections are moderate, with a connectivity of 1.72 C_b.

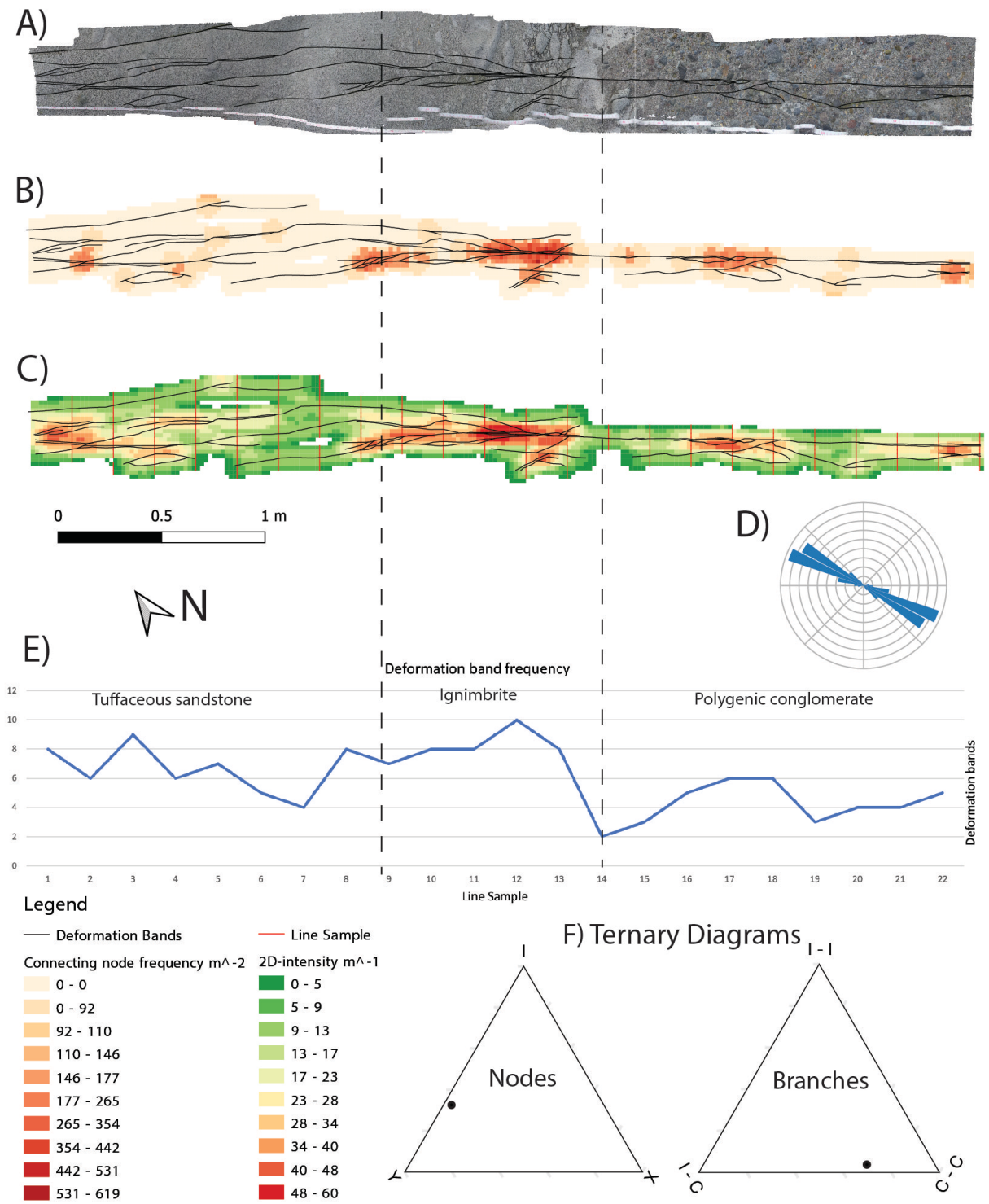

Figure 5.14: The digitized deformation band network DN-3 and various contour maps, graphs and rose diagram displaying topological and geometrical similarities. A) Outlined DN-3 deformation band network. B) Connecting node frequency. C) 2D-intensity map, with line samples counting deformation bands intersecting the line (red). D) Rose diagram presenting the orientations of the deformation bands. E) Deformation band frequency plot. F) Ternary diagram displaying node and branch distribution in DN-3.

Deformation band network SN-1

Deformation band network SN-1 exhibits a sinistral shear offset and is located south of Fault 1 in connection to DN-1 (Fig. 4.3). The displayed section extends over three lithologies: ignimbrite, tuffaceous sandstone, and polygenic conglomerate (Fig. 5.15). The network is 1.8 m long, with a maximum width of 15 cm. However, the width of the network is highly dependent on lithology (Fig. 5.15A). The network appears interconnected, with mainly multi-band networks and clusters. The highest number of bands is associated with the ignimbrite and tuffaceous sandstone unit (Fig. 5.15A). The network in the polygenic conglomerate unit is narrow and comprises a few individual bands. This is reflected in the total cumulative thickness in the different lithologies, measured in line 8, 14 and 31 (Fig. 5.15C), respectively 10.7 cm in the ignimbrite unit, 13.2 cm in the tuffaceous sandstone, and 2.4 cm in the polygenic conglomerate unit. The thickness of individual deformation bands varies (0.3 - 1.5 mm), and bands in the ignimbrite unit occasionally form clusters in centimeter-wide zones.

The deformation bands are mainly oriented ENE-WSW (Fig. 5.15D). The 2D-intensity map shows intensities ranging from 2.7 m^{-1} to 33.8 m^{-1} (Fig. 5.15C), and the connecting node frequency map ranges from 17 m^{-2} to 122 m^{-2} (Fig. 5.15B). High values in the 2D-intensity map are restricted to the ignimbrite and tuffaceous sandstone units. The high 2D-intensities coincide with the connecting node frequencies (Fig. 5.15B). Line samples (Fig. 5.15E) reveal significant variation in the number of intersections along the network. In the ignimbrite unit towards the NE, the network is characterized by an increased number of deformation bands intersecting the lines. The peak value is located in line 14 in the tuffaceous sandstone unit, with a frequency of 23 bands. Further, in the tuffaceous sandstone unit, the frequency decreases before it flattens out in the polygenic conglomerate. Low deformation band frequency in polygenic conglomerates is recognizable in other networks, e.g. DN-2 (Fig. 5.12) and DN-3 (Fig. 5.14). The network has a total of 193 nodes and 239 branches, with a high number of Y-nodes and fully connected branches (Fig. 5.15F). The network's average connections per branch are 1.78 C_b.

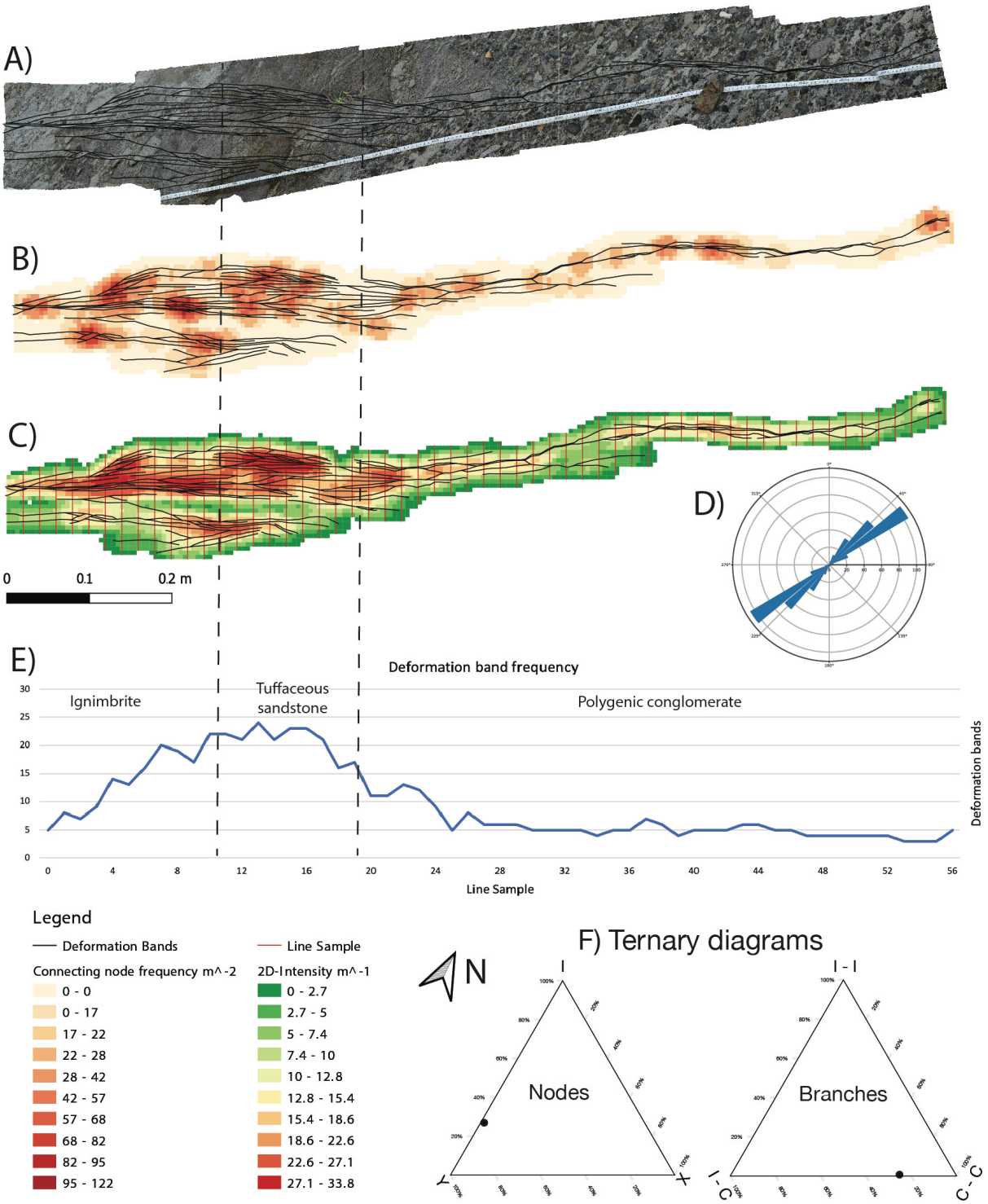

Figure 5.15: Deformation band network SN-1 and different contour maps, graphs and rose diagram displaying topological and geometrical characteristics. A) The digitized SN-1 deformation band network (outlined in black). B) Connecting node frequency. C) 2D-intensity map with line samples counting deformation bands intersecting the line (red). D) Rose diagram presenting the orientation of the deformation bands. E) Deformation band frequency plot, displaying the variation of deformation bands. F) Ternary diagram presenting the node and branch distribution in SN-1.

Deformation band network SN-4

Network SN-4 is a high-resolution model composed of 105 close-up images (Fig. 5.16A). The high resolution makes it possible to capture more details along the entire length of the network. The deformation band network is oriented NW-SE (Fig. 5.16E), is 11.2 m long, and covers an area of approximately 5.37 m^2. Three different scales were chosen to document potential inconsistencies caused by variable resolution: 1:1, 1:4, and 1:8:

- The 1:1 map is the finest map without losing resolution/quality and captures deformation bands down to 0.3 mm width. On this scale, a total trace length of 84.2 m was mapped.
- The resolution of the 1:4 map captures bands down to 1 mm width, and the network has a total trace length of 62.8 m.
- The 1:8 map captures bands and clusters down to 5 mm width, and individual bands within clusters are not possible to detect. The total trace length of the 1:8 map measures 43.3 m.

The deformation band intensity and connecting node frequency vary notably for the different maps in the SN-4 network (Fig. 5.16B, C, D). The 1:1 map has the highest 2D-intensities, ranging from 0 m^{-1} to 198.4 m^{-1}, and the highest connecting node frequency varying from 0 m^{-2} to 5158 m^{-2} (Fig. 5.16B). Note different intervals for the deformation band intensity and connecting node frequency in the 1:1, 1:4, and 1:8 maps. The 1:4 map shows deformation band intensities between 0 m^{-1} and 136.6 m^{-1} and connecting node frequency between 0 m^{-2} to 2947 m^{-2} (Fig. 5.16C). The 1:8 map has deformation band intensities ranging from 0 m^{-1} to 100.8 m^{-1} and connecting node frequency varying from 0 m^{-2} to 1965 m^{-2}. The connecting node frequencies vary on different scales, with less connectivity in the 1:4 and 1:8 maps compared to the 1:1 map. The greater frequencies are restricted to where deformation bands crosscut and abut against one another. The deformation band intensity does not change significantly on different scales. The areas of low and high intensity at the 1:1 scale (Fig. 5.16B) correlate well with the same areas on the 1:4 scale (Fig. 5.16C) and the 1:8 scale (Fig. 5.16D), but the intensity values are decreasing with lower resolution.

The node and branch data extracted from the deformation band networks are shown in Figure 5.16F. The network in the 1:1 map has a total of 857 nodes and 968.5 branches, with a connectivity of 1.65 C_b. The 1:1 map shows a high proportion of Y-nodes (56.8%) and fully connected branches (68.1%). The network in the 1:4 map has a total of 356 nodes and 387.5 branches, with a connectivity of 1.59 C_b. The 1:4 map consists mainly of I-nodes (44.4 %) and Y-nodes (49.2%), and fully connected branches (62.2%). The lowest proportion of nodes and

branches is found in the 1:8 map network with 189 nodes and 203.5 branches. The ternary diagram for SN-4 (Fig. 5.16F) demonstrates that the network in the 1:8 map has a higher proportion of X-nodes and partly connected branches (I-C) compared to the 1:1 and 1:4 map. This results in a network with a connectivity of 1.57 C_b. Overall, the maps on different scales show a low proportion of X-nodes and isolated branches (I-I). The connectivity declines with lower resolution, but at the same time the proportion of X-nodes increases. This correlates well with the connecting node contour maps, demonstrating a reduction in connectivity with lower resolution (Fig. 5.16).

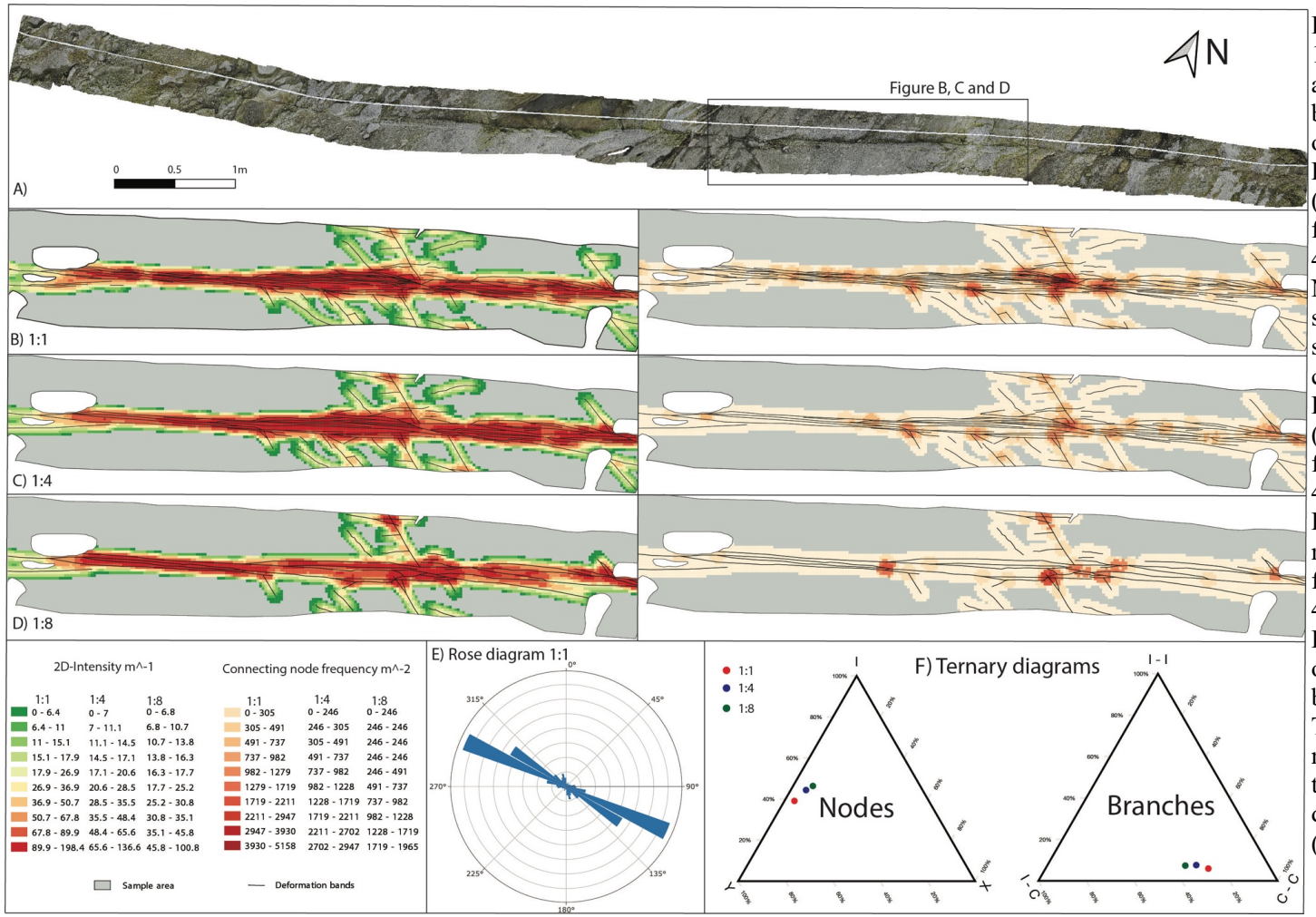

Figure 5.16: A) SN-1 comprises 105 close-up images merged into a high-resolution model. The black box marks the placement of figures B, C, and D. B) Deformation band intensity map (left) and connecting node frequency map (right) of the SN-4 network mapped at 1:1 scale. Note, grid size 0.01x0.001 m and sampling radius 0.03 m are the same for all networks, but the contour intervals vary. C) Deformation band intensity map (left) and connecting node frequency map (right) of the SN-4 network mapped at 1:4 scale. D) Deformation band intensity map (left) and connecting node frequency map (right) of the SN-4 network mapped at 1:8 scale. E) Rose diagram showing the orientations of the deformation bands mapped at 1:1 scale. F) Ternary diagrams displaying the node and branch distribution of the SN-4 network mapped at different scales: 1:1 (red), 1:4 (blue), and 1:8 (green).

5.3.3 Incipient deformation band networks

Incipient deformation band networks (or isolated deformation bands) typically comprise single deformation bands and can be studied along their full length (Fig. 5.17). These bands have low displacement with a maximum displacement no larger than a few centimeters. The length of the incipient networks is between 3.38 and 3.52 m from tip to tip. Depending on lithology, the thickness of the bands and the cumulative thickness varies. The thickness of the deformation bands is from 1 mm in tuffaceous sandstone to 3 mm in ignimbrite, while the cumulative thickness can be up to 35 cm. Linkage points between individual bands occur frequently. Individual bands are bounded by soft- or hard- linkage, where soft-linked bands are represented by I-nodes, whereas hard-linked bands are represented by Y-nodes (Fig. 5.17). Areas of linkage will have higher 2D-intensity due to several bands. Two incipient deformation band networks (IDBN) are presented in detail (Fig. 5.17), focusing on thickness, connectivity, linkage, and intensity. Additional data are in Appendix II.

Incipient deformation band network 1 (IDBN1) (Fig. 5.17A and B) is situated on the western flank of the Cuesta, a few meters from incipient deformation band network 2 (IDBN2). The deformation band network exhibits a sinistral shear movement and is oriented NW. The incipient network measures a length of 3.52 m from tip to tip and a maximum cumulative thickness of 10 cm. Five linkage points represent where deformation bands are bounded together. Four hard-linked zones are observed where individual bands physically meet (Fig. 5.17). Zone 1 and 5 (Fig. 5.17A) demonstrate hard-linked zones where a somewhat linear deformation band bends and joins with a neighboring deformation band. The latter deformation band terminates shortly after the intersection point. This results in a Y-node in the intersection point and an I-node where the other deformation band terminates. Zone 3 and 4 (Fig. 5.17A) show examples of hard-linked systems where two approaching deformation bands curve and connect at two points, forming a ramp structure/eye structure. Consequently, two Y-nodes represent the two connection points. One soft-linked system is observed in IDBN1 in zone 2 (Fig. 5.17A). At this point, the tips of two subparallel deformation bands overlap. No physical connection between the two deformation bands will produce two I-nodes as a replacement for a Y-node.

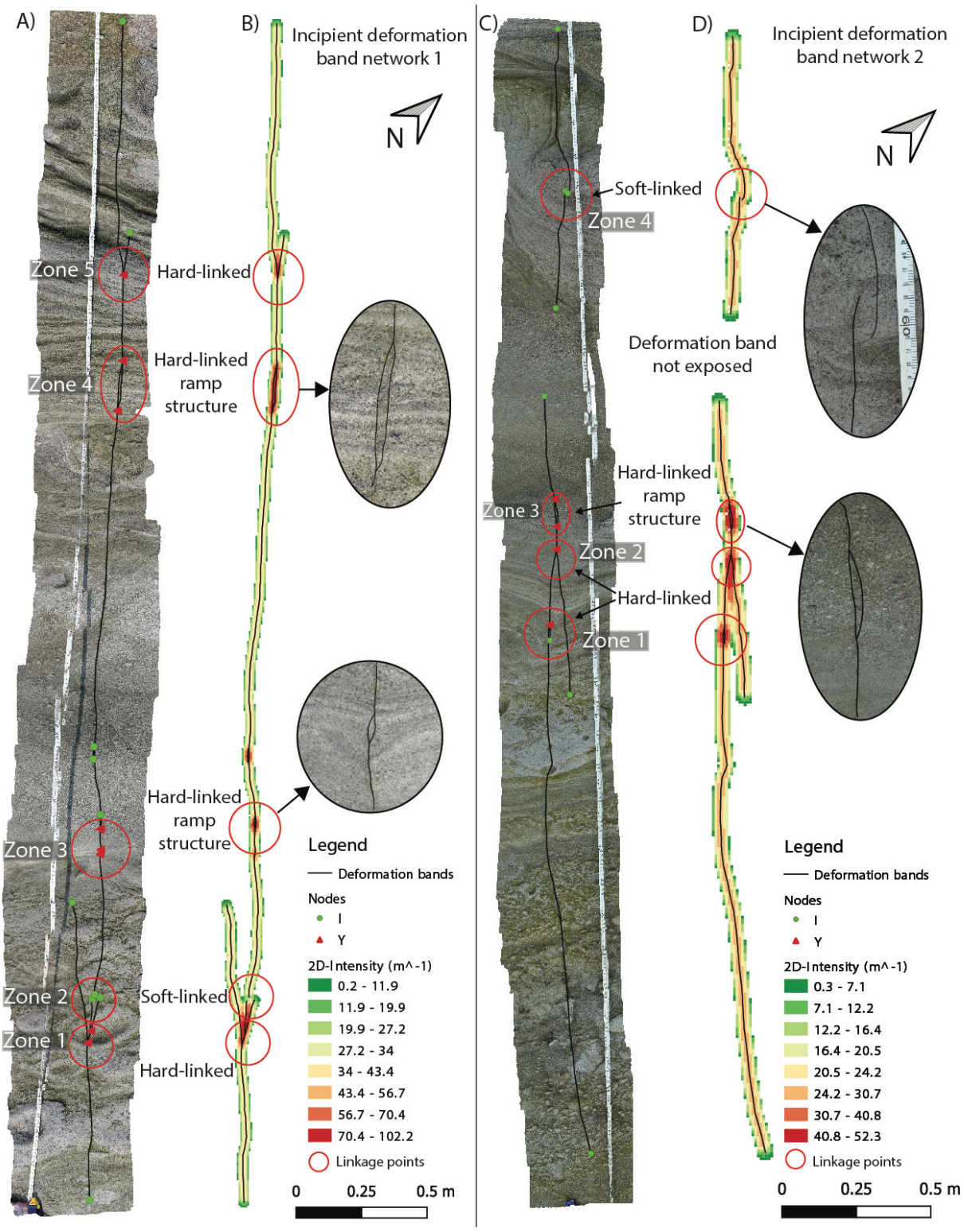

Figure 5.17: Figures summarizing the incipient deformation band network 1 (IDBN1) and 2 (IDBN2). The location of the incipient networks is shown in Figure 4.3. A) Orthomosaic of incipient deformation band network 1, with node distribution. Red circles indicate linkage points. B) 2D-intensity map (IDBN1). The red circles indicate the same linkage points as in A. C) Orthomosaic of incipient deformation band network 2, with node distribution. Red circles indicate linkage points. D) 2D-intensity map (IDBN2). The red circles indicate the same linkage points as in C.

Incipient deformation band network 2 (IDBN2) (Fig. 5.17C and D) is 3.38 m long and is located close to IDBN1. Equivalent to IDBN1, the bands exhibit a sinistral shear movement and is oriented NW. The maximum cumulative thickness of IDBN2 is 6.5 cm. In Figure 5.17C and D, four linkage systems are recognized, three hard-linked systems and one soft-linked system. Zone 1 and 2 display hard-linked zones where a straight deformation band curve and connect with a nearby deformation band. The two hard-linked systems (Fig. 5.17C) are represented by a Y-node at the intersection point and an I-node where the other deformation band terminates. The linkage system in Zone 3 (Fig. 5.17C) shows a ramp structure, where the connection of deformation bands forms two Y-nodes. In contrast, the soft-linked system in zone 4 forms an "open eye" structure (Fig. 5.17C). In this case, the deformation bands tips overlap and curve but never physically connect to form a hard-linked eye/ramp structure.

6 Discussion

This chapter addresses the topological characteristics of deformation band networks in volcaniclastic rocks from Shihtiping, Taiwan, and how the topology compares to other structural networks. The evolution of a deformation band network is discussed by using the documented topology. Additionally, controls on deformation band frequency, implications for fluid flow and how resolution affect nodal characteristics will be discussed.

6.1 Topological characteristics of deformation band networks in volcaniclastic rocks

A deformation band network consists of numerous bands with a wide range of orientations and lengths, which can potentially form an interconnected network. Topological analyses of the deformation band networks have been completed, focusing on characterizing the connectivity and arrangement of bands within the network. The topology defines the connection relationship using nodes and branches (Fig. 6.1), a dimensionless parameter that are invariant to scale and strain in the network (Manzocchi, 2002, Sanderson and Nixon, 2015). The proportion of nodes and branches provides the basis for describing the connectivity in the studied deformation band networks. In addition, contour maps of connecting node frequency (m^{-2}) and 2D-intensity (m^{-1}) are used to visualize the spatial distribution of the connectivity in the networks. Digitization of eleven deformation band networks were completed for topological characteristics.

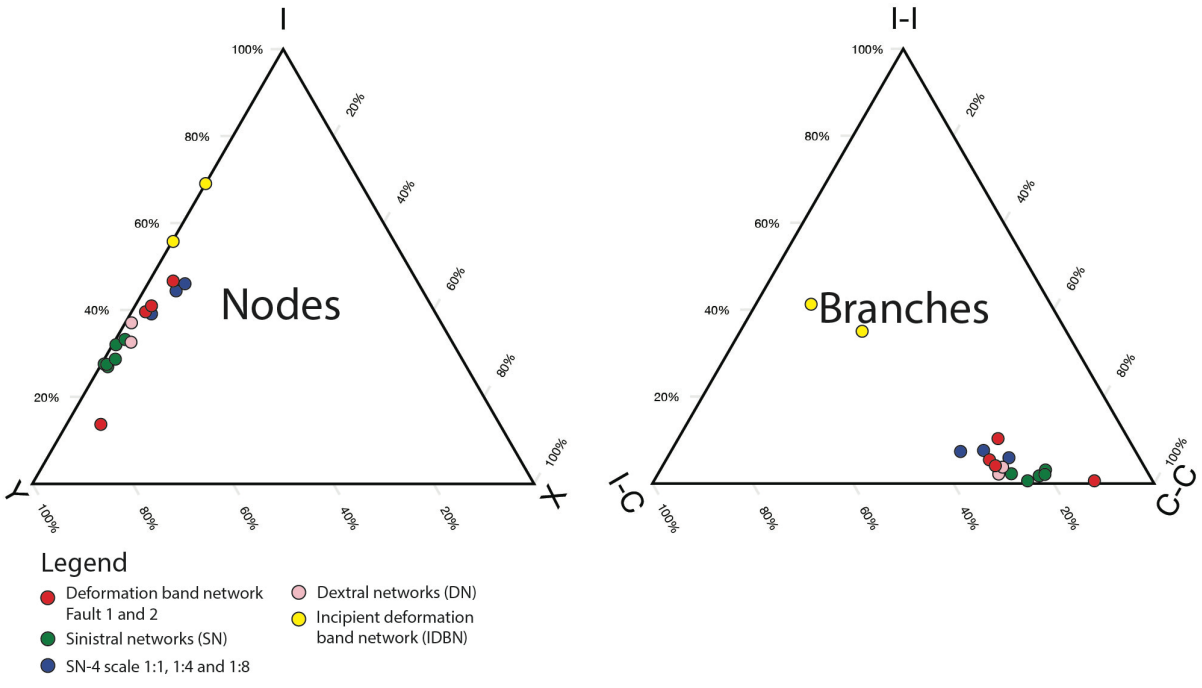

Figure 6.1: Node and branch ternary plots showing the topology of all the collected data in this thesis. The node plot displays the proportion of I-, Y-, and X-nodes within the studied deformation band networks. The branch plot shows the proportion of isolated I-I branches, partly connected (I-C) branches and fully connected (C-C) branches within the studied deformation band networks. Note that the topological data from Figure 5.5 are excluded, as it contains both faults and deformation bands.

Deformation band networks in Shihtiping appear almost exclusively with fully connected (C-C) branches and connecting Y-nodes. The distribution of nodes shows a very similar topological trend for all deformation band networks, where all plots along the I-Y axis (Fig. 6.1). Consequently, this suggests that the interconnected networks generally exhibit high average connectivity. The observed topology displays a high proportion of Y-nodes and a low proportion of X-nodes. This coincides fairly well with other studies that suggest that deformation bands tend to bifurcate and link, rather than to crosscut one another (Aydin and Johnson, 1978, Fossen and Hesthammer, 1997). The proportion of connecting nodes (mostly Y-nodes) shows a positive correlation with the 2D-intensity, suggesting that increased strain will cause deformation bands to interact and bifurcate (Figs. 5.12, 5.14, 5.15). This is supported by Wilson et al. (2020), which also shows an increase in Y-nodes with increased intensity. Studies from Fossen and Hesthammer (1997) demonstrate that increased strain is associated with dense networks. Increased strain causes more connection of deformation bands during growth, resulting in a significant number of Y-nodes in dense networks. A high proportion of Y-nodes are also reported from deformation band network analyses in Utah by Manzocchi (2002) and Awdal et al. (2020) (Fig. 6.3).

The nodal analysis of the networks shows a low proportion of X-nodes (Fig. 6.1). Deformation bands tend to form two Y-nodes with a small offset instead of one X-node. The orientation of deformation bands does not change significantly within the networks (Figs. 5.6, 5.12, 5.14, 5.15) and occur more or less parallel to the strike direction. With more variable orientations across the networks, more X-nodes would have been expected where the deformation bands intersect. This is not considered a valid explanation for the low X-nodes proportion, but it could explain the high Y-node proportion. Manzocchi (2002) and Awdal et al. (2020) plot a nodal distribution with a higher X-node proportion than the majority of networks in this study (Fig. 6.3). The difference in X-node distribution could be explained by lithological differences. While Manzocchi (2002) and Awdal et al. (2020) plot deformation bands exclusively from sandstone in Utah, and UK, respectively, this study plots deformation bands from volcaniclastic rocks with changing lithological properties. Nevertheless, more nodal analyses of deformation bands in volcaniclastic rocks should be carried out to confirm this. Sampling methods can also

play an important role in nodal distribution. All deformation band networks in this study were digitized from map views (horizontal sections). Awdal et al. (2020) plots deformation bands from both horizontal and vertical sections and reports a higher proportion of X-nodes in the vertical sections, thus lower proportion of X-nodes in the horizontal sections. How deformation bands propagate in the subsurface can explain the high proportion of X-nodes from Awdal et al. (2020) and will be an important factor for the connectivity of the network as a whole in three-dimensions. It is important to take the stress axis into account when making such a comparison. In a horizontal section in an extension regime (e.g. Awdal et al., 2020)), sigma 1 will be perpendicular to the plane of observation. In this study, sigma 1 is parallel to the horizontal plane (plane of observation). In a comparison of deformation band networks, it is relevant to consider what is the purpose of the analysis. For instance, the nodal analyses from Awdal et al. (2020), focus on deformation bands and ladder networks. An increasing X-node proportion is expected with the existence of ladder structures which occasionally crosscut the deformation bands and thereby making X-nodes. The number of X-nodes in a network may be related to resolution (Morley and Nixon, 2016) and will be discussed in Subchapter 6.6.

The proportion of I-nodes is generally lower than the Y-node proportion, but higher than the X-node proportion (Fig. 6.1). The exception is the incipient deformation band networks which contain more I-nodes than Y-nodes (Fig. 6.1). This is expected when the incipient deformation band networks consist of few individual bands with low connectivity (Fig. 5.17). Nevertheless, a fair number of I-nodes are found in the mature deformation band networks and the deformation band networks in fully developed faults. A lower proportion of I-nodes would have been expected in a more developed network, as increased strain is associated with more interactions and connected branches (Morley and Nixon, 2016). The dominant linking system in the network largely determines the distribution of nodes. Soft-linked and hard-linked deformation bands described by Fossen and Hesthammer (1997) can (to some extent) explain nodal distribution. Soft-linked deformation bands will contribute to more I-nodes, while hard-linked deformation bands generally will contribute to more Y-nodes. Although, hard-linked horse-tailing systems (Fossen and Hesthammer, 1997) where a single deformation band splays into series of bands that eventually die out are observed. Such a linkage system will result in more I-nodes where the bands terminate. The sampling method used in this thesis must also be taken into consideration, in relation to the nodal distribution. Sampling bias due to censoring effect occurs when a deformation band exceeds the boundary of the sample area. When the

deformation band extends beyond the sample area boundary it is not counted as I-nodes, but as an E-node (described in Chapter 4).

Contour plots from the deformation band networks show a positive correlation between 2D-intensity (m^{-1}) (strain) and connecting node frequency (m^{-2}) (Figs. 5.7; 5.10, 5.12, 5.14, 5.15). This suggests that areas with high strain will have a high connectivity. There is also a positive correlation between 2D-intensity and node proportion, where an increased number of nodes is expected in high strain areas. The proportion of fully connected (C-C) branches and Y-nodes results in high connectivity networks (Sanderson and Nixon, 2015). However, the network connectivity (measured as connections per branch) shows some variations in the studied networks, with a range from 1.55 - 1.89 C_b. The topological and geometrical findings from this thesis support the theory by Fossen and Hesthammer (1997) that increased strain will cause deformation bands to grow, link, and form more densely spaced networks.

6.2 Sequential growth of deformation band networks in volcaniclastic rocks, and how it affects topology

The connectivity of deformation networks develops with time and maturity (Morley and Nixon, 2016). Quantifying the topological and geometrical characteristics may strengthen our understanding of deformation band network development in volcaniclastics rocks. During fault displacement and damage zone widening, strain increases, and deformation band networks change their characteristics and geometry (Shipton and Cowie, 2001). Aydin and Johnson (1978) apply a three-step model to explain the sequential development from a single deformation band towards clusters of bands and, finally, into faults. The degree of interconnectivity may therefore be related to how faults grow in highly porous rocks. A similar model based on Aydin and Johnson (1978) is proposed for the sequential development of faults in volcaniclastic rocks.

Stage 1 - Initial stage

The studied incipient deformation band networks (Subchapter 5.3.3) may represent the first stages of fault development in volcaniclastics. The incipient deformation band networks are characterized by one to three deformation bands and can be studied along their full length. The lengths of isolated bands range from a few centimeters to hundreds of meters, with a maximum displacement of a few centimeters (Fossen and Hesthammer, 1997). According to Fossen and Hesthammer (1997) definition, isolated deformation bands do not interfere with other bands in map view, and nearest tip points are more than c. 40 cm away from one another. By definition,

these bands would be I-node dominated. The exception to this rule is where isolated deformation bands form a multisegmented system. Here the distance between the deformation band tips is closer than c. 40 cm forming a linkage system (Fig. 5.17). A system of mainly soft-linked deformation bands of overlapping tips contributes to an I-node dominated system. A hard-linked system occurs where individual bands physically connect and will form a Y-node. Observations from this study show a combination of soft- and hard-linked systems (Fig. 5.17), where linkage represents zones between individual bands at an earlier stage of development. The fact that isolated deformation bands can extend over long lengths with low displacement increases the bands chance to interact and link up. At the first stage in the fault evolution, the type of linkage and interaction are the most important factors for topology and formation of an interconnected network.

Stage 2 - Intermediate stage

The incipient deformation band networks evolve into a much more complex system in the intermediate fault stage. This stage can be exemplified through the mature deformation band networks (Subchapter 5.3.2). The deformation bands links through hard- or soft-links forming cluster zones of bands (Fossen and Hesthammer, 1997). These zones consist of numerous deformation bands with varying intensity and connectivity (Figs. 5.12, 5.14; 5.16). The existing damage zone becomes more comprehensive as the strain increases over time (Shipton and Cowie, 2003). From the initial stage, the damage zone grows with the development of new deformation bands inside and outside the existing damage zone (Schueller et al., 2013). Splaying and bifurcation of bands are common at this stage resulting in a variable cumulative thickness of the deformation band networks. Laboratory experiments conducted by Mair et al. (2000) show a strong positive correlation between applied axial strain and the number of deformation bands in a cluster. A single deformation band only accommodates a finite amount of displacement/strain due to the mean grain size within the deformation bands attains a stabilized value independent of axial strain (Mair et al., 2000). Mair et al. (2000) introduce a conceptual model for the evolution of deformation band zones where strain can move between bands. In comparison to elastic crack models (e.g. Das and Scholz, 1981, Kostrov and Das, 1988), this model is based on the presumptions that deformation bands have increased shear stress in their tip-points and in the regions parallel to the deformation bands. The tip-points may be weakened by induced microcracking (Teufel, 1981). Frictional sliding along the deformation band accommodates strain in these regions. Increased friction will eventually cause the initial band to lock up, and it becomes energetically favorable to begin a new deformation band in the

weakened region instead of continuing on the existing band (Mair et al., 2000). The new deformation band repeats the process leading to additional deformation band formation. Favoring the formation of new bands will increase the number of bands and simultaneously cause increased linking and splaying of bands. This model can explain why mature deformation band networks are dominated by Y-nodes and C-C branches with high connectivity (Fig. 6.1). However, lithological differences along the network will greatly affect the deformation band architecture. This is supported by the observations in Figure 5.12 and Figure 5.15, where deformation band networks in tuffaceous sandstone and ignimbrite units are generally wider and consist of several bands. Simultaneously, the deformation band network in the polygenic conglomerate is characterized by a narrow network with few bands. A patchy slip-surface develop locally in some lithologies of the deformation band network.

Stage 3 - Fully developed faults

At the final stage, patchy slip-surfaces in zones of deformation bands start to propagate and link to form the structure defined as a fully developed fault (Shipton and Cowie, 2001). A certain amount of strain (number of deformation bands) is necessary for a slip-surface to nucleate across the deformation band zone (Antonellini and Aydin, 1994). However, the development varies depending on host rock properties (Fossen et al., 2018). The formation of a distinctive fault core and through-going slip-surfaces typically marks the final stage of fault zone establishment. Fault formation accumulates slip-surfaces that are much larger than clusters of bands, and the cluster becomes a part of the established damage zone (Fossen et al., 2018). Simultaneously, new deformation bands develop within and outside the damage zone, resulting in an expanded damage zone. Nevertheless, the architecture of the studied deformation band networks in the fault damage zone (Fault 1 and Fault 2) demonstrates large variations probably due to lithological differences. As a result, the 2D-intensity and Y-node proportions vary along the fault. The fault core in Figure 5.7, 5.8, and 5.10 is associated with the highest number of bands and highest intensity (m^{-1}) of all studied deformation band networks. A high deformation band intensity indicates a complex network, while a high connecting node frequency indicates a highly connected network (Morley and Nixon, 2016). The connectivity of the deformation band networks at this stage varies but is generally high (over average).

Figure 6.2 summarizes the proposed fault evolution model in volcaniclastic rocks with emphasis on the topological arrangement of deformation bands. The deformation mechanisms in the studied rocks appear to be accommodated by granular flow and cataclastic flow

(translation, rotation, and fracturing of grains) (Cavailhes and Rotevatn, 2018). Granular flow is often part of the early-stage deformation, in the form of shear-induced compaction by grain reorganization (Wong et al., 1997, Rotevatn et al., 2008). Furthermore, grain fracturing enlarges by shearing and development of single cataclastic deformation bands. The sequential fault evolution from single cataclastic deformation bands to clusters of deformation bands and finally to a through-going slip-surface (Fig. 6.2) are equivalent to previous studies (Aydin and Johnson, 1978, Shipton and Cowie, 2001).

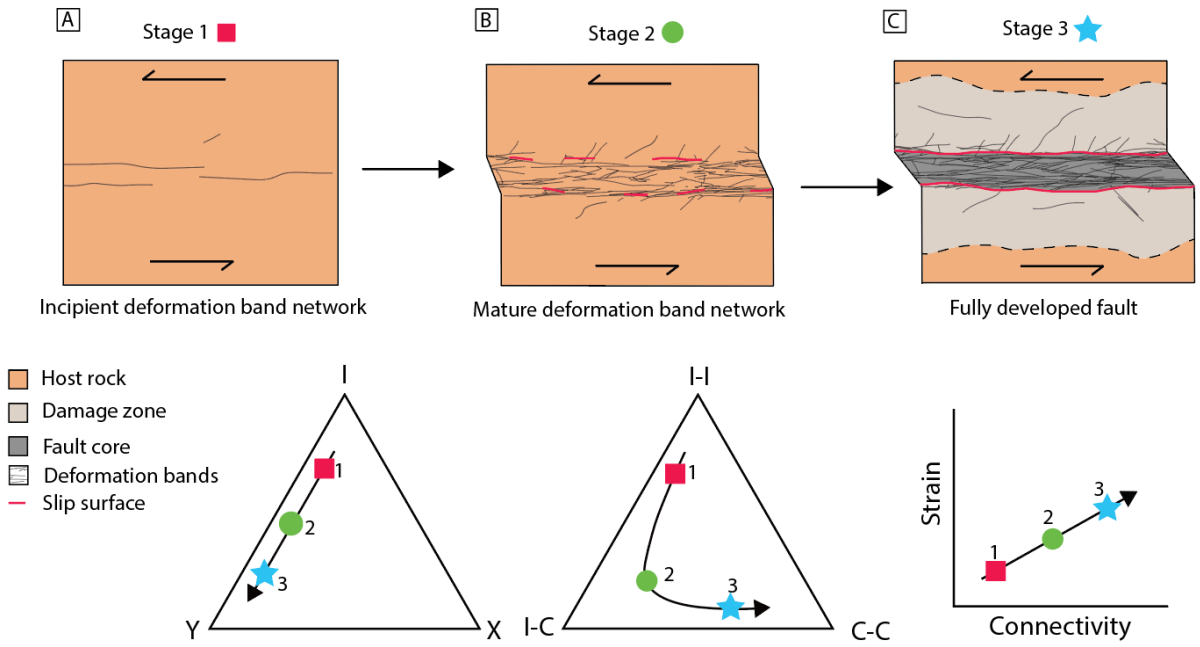

Figure 6.2: Proposed schematic model over the different stages (1-3) of fault evolution in volcaniclastic rocks. The illustration showcasing the sequential growth of a deformation band network to a fully developed fault (A-C). Increased strain causes bands to link up and contributes to a more interconnected network. The ternary plots and arrows display how the topological character changes with increased strain. A) Slightly deformed host rock with a few individual deformation bands. B) Increased strain produces more deformation bands and patchy slip-surfaces. C) A fully developed fault with a distinctive fault core and through-going slip-surface.

The results from this thesis coincide with the proposed model to some extent. The nodal distribution of the studied incipient deformation band networks (stage 1) is dominated by I-nodes and have no X-nodes, while branches are dominated by I-I branches and I-C branches (as expected) (Fig. 6.1). Stage 1 (incipient deformation band network) has a lower connectivity than stage 2, with an average connectivity of 1.31 C_b (average connections per branch). The difference between the deformation bands in the mature networks (stage 2) and fully developed faults (stage 3) is limited. Mature deformation band networks still have a high number of I-nodes, but are in general Y-node dominated, with some X-nodes. Branches in the mature

networks (stage 2) are dominated by C-C branches (Fig. 6.1). The average connectivity for all mature networks is 1.72 C_b. The deformation band in fully developed faults (stage 3) shows a similar distribution of nodes and branches regarding the mature networks. The exception is the deformation band network in Fault 2 (Fig. 5.10), which shows a higher average connectivity (1.89 C_b) than the rest of the networks. The deformation band network in Fault 2 fits the proposed model but does not form a basis for comparison. The topological variations may be due to the changing lithology across the studied networks, which makes comparison difficult.

Another reason for the limited difference between mature deformation band networks and the faults may be that the deformation in the faults occurs through further strain-softening/slip, and not by the formation of new deformation bands. This will cause little or no change in the connectivity between the mature networks and the faults. However, the topological characteristics of a deformation band network will develop from an I-node and I-I branch network to a Y-node and C-C branch dominated network with higher connectivity (Fig. 6.2).

6.3 How does the topology of a deformation band network in volcaniclastic rocks compare to other structural networks?

The deformation band networks presented in this study share some topological similarities with other structural networks (e.g. faults, joints and other deformation band networks). The proportion of I-, Y- and X-nodes can be plotted in ternary diagrams and be used to characterize the different networks (Manzocchi, 2002, Mäkel, 2007) (Fig. 6.3). Figure 6.3 shows that X-nodes rarely dominate any structural network (deformation bands, joints, fractures and faults). Observations from this thesis, combined with those from Manzocchi (2002), Awdal et al. (2020) and Wilson et al. (2020) show that deformation band networks contain the highest Y-node proportion of any structural network. However, the majority of the deformation band networks in this thesis have a slightly lower Y-node (higher I-node) proportion than reported from Manzocchi (2002), Awdal et al. (2020) and Wilson et al. (2020) (Fig. 6.3).

In comparison with deformation band networks (Fig. 6.3), the fault networks contain more Y-nodes than X-nodes and plots along the I-Y axis of the ternary diagram (Fig. 6.3). Nevertheless, the faults generally contain more I-nodes than the majority of the deformation bands. The deformation band networks in this thesis plots between the faults and the deformation band networks analyzed by Manzocchi (2002) and Awdal et al. (2020). Faults evolve in response to increasing strain and their network geometry change as faults grow, interact and link

(Cartwright et al., 1995, Ackermann et al., 2001, Walsh et al., 2003). Duffy et al. (2017) demonstrate how the topology develops with respect to increasing strain and how maturity and connectivity of fault networks change during progressive deformation. The topological changes can be exemplified through the evolution of single-phase and multi-phase fault networks (Duffy et al., 2017).

In the single-phase, a set of several small, isolated faults develop into a network of fewer, longer and subparallel faults. This development causes minimal cross-strike connection, which does not favor the development of connection nodes (Duffy et al., 2017). The connecting nodes that develop are restricted to splaying and fault linkage (Duffy et al., 2017). At low strain, the fault network is isolated with subparallel configuration of the fault segments, resulting in a fault network composed of only I-nodes and I-I branches (Fig. 6.3B) (Duffy et al., 2017). As strain accumulates, the faults start to link up and the nodal topology shows an increase in the proportion of Y-nodes. However, the fault network is still I-node dominated because smaller faults remain isolated in the stress shadow of larger faults (Walsh et al., 2003, Duffy et al., 2017). Even at the largest strain, the proportion of X nodes is low (Duffy et al., 2017).

The multi-phase fault networks are more complex and involve a second phase of faulting. The geometry of multi-phase fault networks is characterized by the development of new faults that gradually link by a progressive increase in strain (Duffy et al., 2017). At low strain the network comprises sets of isolated, weakly developed faults, and the topology is characterized by only I-nodes. With increased strain the number of Y-nodes increases due to fault linkage where new faults are oriented obliquely to the pre-existing faults, resulting in a more connected network (Fig. 6.3A) (Duffy et al., 2017). The topological evolution of the second phase is driven by the development of Y-nodes, and a lesser degree of X- nodes.

Fault growth is associated with strain-softening mechanisms, where the faults are weaker than the undeformed host rock (Shipton and Cowie, 2003). This means that it is energetically favorable for the fault to continue along the slip-surface instead of forming new faults. Unlike faults, are deformation bands associated with strain-hardening mechanisms, and promotes formation of new bands (Mair et al., 2000), which increases the possibility of linkage. Therefore, the fault networks will hardly be as connected as deformation band networks.

The greatest variation in topological characteristics is found in networks consisting of joints (Fig. 6.3). Fracture network (e.g. joints, veins, faults) normally include higher proportions of Y-nodes relatively to X-nodes (Sanderson and Nixon, 2015), but the joint networks from Manzocchi (2002) can be I-, Y-, or X-node dominated (Fig. 6.3). Joints are the result of brittle deformation where there is no relative displacement (Peacock, 2001). This may explain the high proportion of X-nodes in relation to other structural networks (Fig 6.3F), as the X-nodes in the joint networks sometimes are preserved. Although, preservation problems can explain the varying topological characteristics in the joint network. When an active fault accumulates displacement, the younger joint usually stops at the older joint, resulting in two Y-nodes instead of one X-node (Morley and Nixon, 2016). However, there is need for a more consistently applied and quantitative analysis that makes it easier to compare the topological characteristics of the different structural networks.

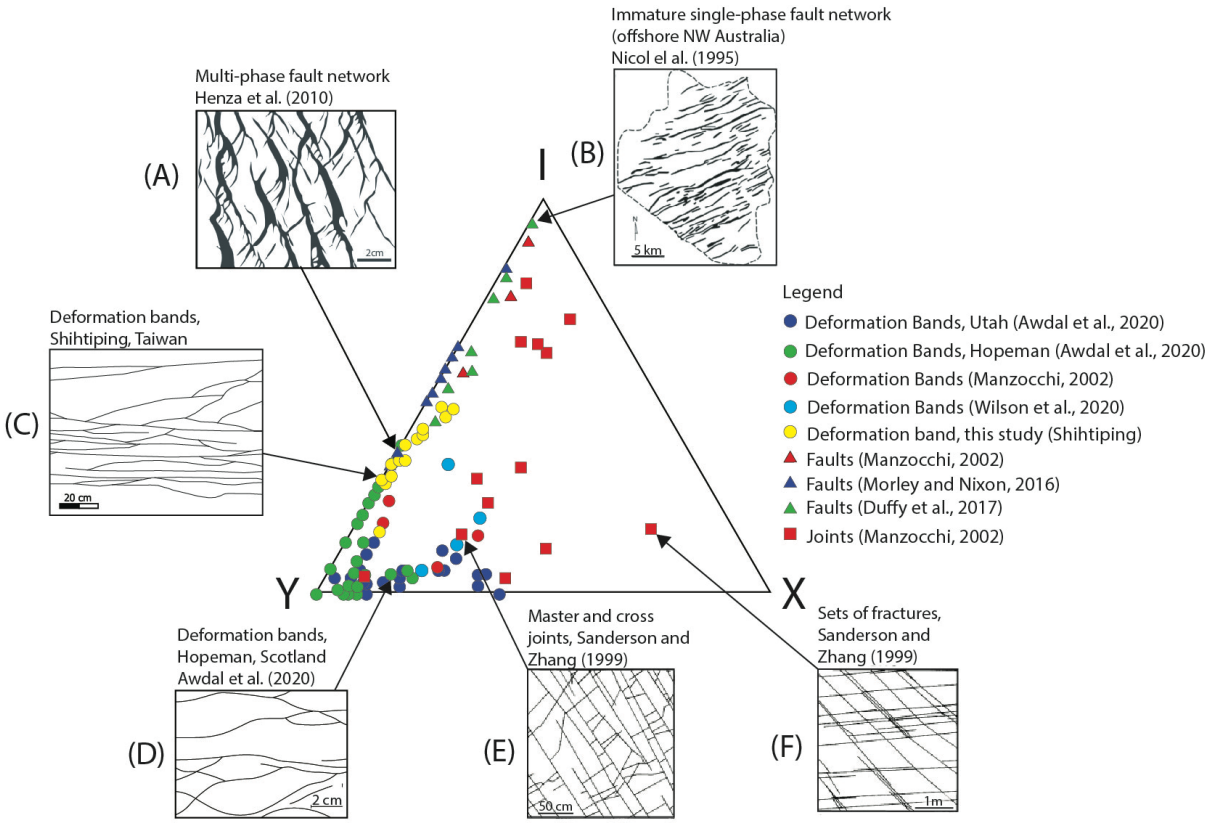

Figure 6.3: Ternary diagram of the proportion of node types for different types of structural networks: Three different types of networks from Manzocchi (2002), deformation band networks from Awdal et al. (2020) and Wilson et al. (2020), faults networks from Morley and Nixon (2016) and Duffy et al. (2017), in addition to the deformation band network from this study. A) Multiphase fault network (Henza et al., 2010). B) Single-phase rift network with subparallel isolated faults from offshore Australia (Nicol et al., 1995). C) Deformation band network from Shihtiping. D) Deformation band network from Hopeman, Scotland (Awdal et al., 2020). E) Joint network with sets of master and cross joints (Sanderson and Zhang, 1999). F) Joint network with sets of cross-cutting joints (Sanderson and Zhang, 1999).

6.4 Controls on deformation band frequency in layered volcaniclastic rocks

The studied deformation band networks occur in three lithologies: ignimbrite, tuffaceous sandstone, and polygenic conglomerate. The different lithologies show very different distribution when it comes to the deformation band frequency and cumulative thickness (e.g. Figs. 5.12 and 5.15). Observations of deformation bands crossing different lithologies in layered sedimentary sequences can contribute to the understanding of how lithology affects deformation band style and distribution (Fossen et al., 2007). As mentioned earlier, increased strain will lead to the formation of new deformation bands (Mair et al., 2000). However, the distribution of deformation bands is highly sensitive to host rock properties, including porosity, grain size, grain shape, cement, and mineralogy (Wong et al., 1997, Fossen et al., 2007, Eichhubl et al., 2010, Cavailhes and Rotevatn, 2018).

Deformation bands are restricted to porous granular rocks (Aydin and Johnson, 1978, Aydin and Johnson, 1983, Antonellini et al., 1994, Fossen et al., 2007, Ballas et al., 2015). The formation of deformation bands involves a substantial proportion of grain rotation and translation that requires a certain amount of porosity (Fossen et al., 2007). If the porosity is too low, brittle deformation as tension fractures and slip-surfaces will preferentially form (Fossen et al., 2007). Porosity regulates the deformation mechanism of granular rocks (Aydin et al., 2006, Ballas et al., 2015), and studies show that porosity variations of only a few percent can result in remarkable differences concerning deformation band density and distribution patterns (Fossen et al., 2007).

Line frequency measurements from the results show that the polygenic conglomerate units comprise fewer deformation bands compared to the tuffaceous sandstone and the ignimbrite units (e.g. Figs. 5.12 and 5.15). Host rock porosity measurements in Shihtiping by Kjenes (2018) and Jervidalo (2018) show significant variations in the different lithologies and may be the reason for the variation in deformation band frequency. The polygenic conglomerate units exhibit a lower average porosity (9.57%) compared to the tuffaceous sandstone (27.2%) and the ignimbrite units (30.18%). The tuffaceous sandstone and the ignimbrite units have higher porosity and favor deformation by forming deformation bands, whereas low-porosity rocks deform mainly by brittle fracturing. The deformation band networks in the tuffaceous sandstone and the ignimbrite units are typically constituted by a wide zone consisting of numerous deformation bands (Fig. 6.4). In contrast, the polygenic conglomerate units generally are

associated with few bands and a low cumulative thickness (Fig. 6.4). The presence of expansion fractures is also more prevalent in the polygenic conglomerate units.

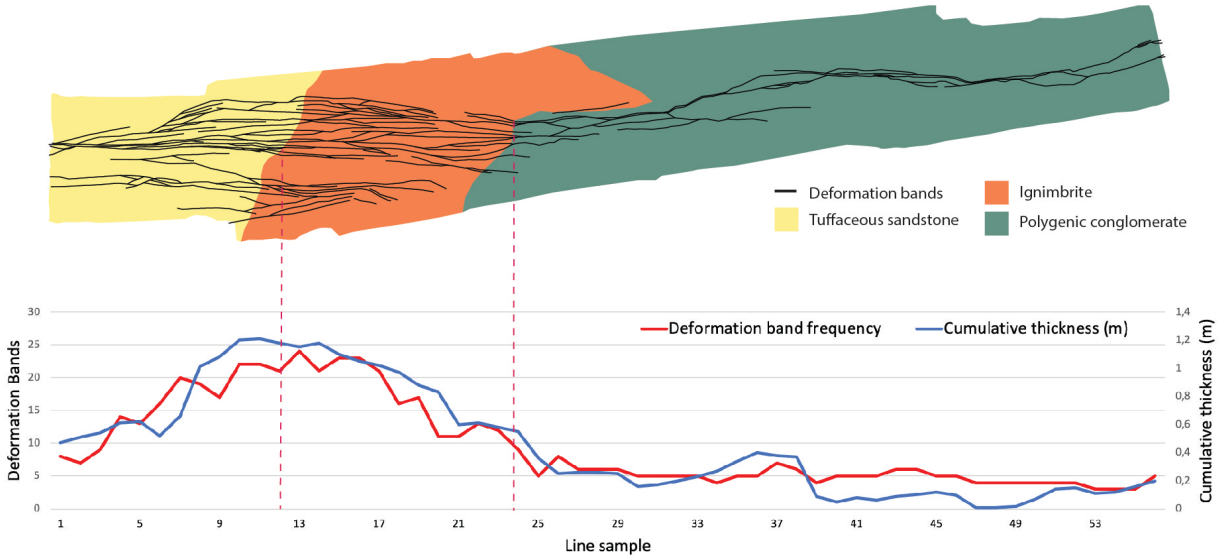

Figure 6.4: Demonstrates how the cumulative network thickness (blue graph) and the number of deformation bands (red graph) varies along Network SN-1. Yellow = tuffaceous sandstone (average porosity of 27.2%). Orange = ignimbrite unit (average porosity of 30.18%). Green = polygenic conglomerate (average porosity of 9.57%).

Figure 6.4 demonstrates how porosity and lithology controls the number of bands and cumulative thickness in a deformation band network. This trend is found in several of the studied networks (e.g. Figs. 5.12 and 5.15). The cumulative thickness and number of deformation bands in a network is an important factor for the permeability and therefore their effect on fluid flow (Fossen et al., 2007) (see Subchapter 6.5 for more details).

6.5 Implications for fluid flow in volcaniclastic reservoirs

Deformation bands are common strain localization in deformed porous rocks and tend to have lower porosity and permeability than their host rock (Antonellini and Aydin, 1994, Fisher and Knipe, 2001, Lothe et al., 2002). The reservoir potential of volcaniclastic rocks is less documented in terms of hydrocarbon exploration, CO_2 storage, hydrothermal energy, and groundwater resources, compared to carbonate and siliciclastic systems (Annunziatellis et al., 2008, Zhu et al., 2011, Lenhardt and Götz, 2011). In recent years, volcaniclastic reservoirs as new sources of petroleum resources have become a hot topic in petroleum exploration. Even though volcanic rocks cannot produce hydrocarbons, they can still act as reservoirs for oil and gas under the right conditions. The geometry and architecture of deformation bands and small-

scale fracture networks often fall beneath seismic resolution, and therefore prediction of subsurface flow is complicated (Rotevatn et al., 2009a). Understanding the deformation mechanisms affecting volcaniclastic rocks can contribute to more knowledge about the subsurface fluid flow in these rocks. The studied volcaniclastic succession could be a good analog for subsurface reservoirs/aquifers.

Deformation bands are considered to act as conduits or barriers to the flow of fluids (Knipe et al., 1997, Gibson, 1998, Aydin, 2000, Fossen and Bale, 2007, Torabi et al., 2013, Ballas et al., 2015). However, proving deformation bands influence on fluid flow in reservoirs is difficult and an ongoing subject of study. The majority of deformation bands shows a reduction in permeability in comparison with the host rock. A single deformation band can cause a reduction in permeability between two to four orders of magnitude, while thicker clusters can show reductions up to six orders of magnitude (Antonellini and Aydin, 1994, Fossen and Bale, 2007). It is common to assume that deformation bands do not have a significant effect on reservoir performance, except for high-intensity networks, with good interconnection and very low permeability (Fossen et al., 2007, Rotevatn et al., 2009b, Rotevatn et al., 2013, Ballas et al., 2015, Fossen et al., 2018). Nevertheless, the orientation, arrangement, and connectivity of deformation bands within a network may have a controlling effect on flow pattern and reservoir sweep (Fossen and Bale, 2007, Rotevatn et al., 2013, Fossen et al., 2018). The results from this thesis can give valuable insights into the deformation band properties and variations within networks, through parameters as connectivity, intensity, and distribution.

It is crucial to quantify the connectivity and intensity of the network, as it generates parameters that can be used to assess the potential for fluid flow in a reservoir (Manzocchi, 2002, Morley and Nixon, 2016). The majority of previous studies use topology on fault and joint networks, where high connectivity normally represents a more permeable zone (Dimmen et al., 2017, Procter and Sanderson, 2018). In contrast, high connectivity zones of deformation bands may act as a baffle for fluid flow and do not represent increased permeability (Fossen and Bale, 2007). Observations from this thesis show deformation band networks with high connectivity (Fig. 6.1). Deformation band networks with high intensity (increased strain) shows more closely spaced deformation bands, a more interconnected network, and development of clusters (Figs. 5.7, 5.8, 5.10 and 5.15). The number of deformation bands and their cumulative thickness will also affect the fluid flow in a high connectivity network. Networks with high deformation band frequency will often have a greater cumulative thickness and therefore act better as a fluid flow

barrier. The line measurements (Figs. 5.7; 5.10, 5.12, 5.14, 5.15) display a significant variation of deformation bands perpendicular to the strike. Fossen and Bale (2007) discuss fluid's ability to divert through, between, or around deformation bands when the connectivity, frequency, and cumulative thickness is low. For this reason, it is reasonable to assume that a deformation band network with high connectivity and cumulative thickness will have the potential to channelize fluids along strike or act as a baffle to fluid flow (Fossen et al., 2005). However, deformation band's influence on fluid flow depends strongly on their internal permeability relative to the host rock (Rotevatn and Fossen, 2011, Rotevatn et al., 2013, Fossen et al., 2018). Low permeability contrast between the host rock and the deformation band will, under most conditions, have insignificant effects on fluid flow (Rotevatn and Fossen, 2011). In comparison, networks with high permeability contrasts can considerably affect fluid flow (Rotevatn et al., 2009a, Rotevatn and Fossen, 2011).

Aforementioned, deformation bands practical effect on permeability is highly dependent on clusters and cumulative thickness of the deformation band networks. Consequently, the incipient deformation band networks will have a limited impact on fluid flow, as they rarely comprise more than three deformation bands. Clusters and deformation bands in tight networks, on the other hand, may exhibit a high sealing capacity. Accordingly, the mature networks will have a limited effect on fluid flow, whereas bands forming in the fault area may act as a baffle to fluid flow. However, the porosity, clast content, and fault architecture will vary along the fault as volcaniclastic rocks often comprise layered successions. Depending on the deformation mechanism, the fault could potentially function as baffles in some lithologies and conduits for fluid flow in others. The varying architecture caused by the great heterogeneities in the succession impacts permeability along and across the fault. This study favors topological analyses of deformation band networks. Direct permeability and porosity measurements must be implemented for establishing deformation bands influence on fluid flow in the subsurface.

6.6 Resolution, relevance of topological characterization

Deformation bands appear very differently with different resolutions, and how nodes are interpreted may depend on the resolution of the collected datasets. In a petroleum field setting, the detection of deformation bands falls below seismic resolution. The prediction of small-scale structures such as deformation bands is possible by analog field studies in combination with an in-depth understanding of the reservoir's geology (Zuluaga et al., 2016). Therefore, it is important to have knowledge of how resolution affect the relationship of deformation bands. Field studies by Aydin and Johnson (1978) report that individual deformation bands often are physically connected, but rarely crosscut each other. However, an increased number in X-nodes are observed with lower resolution (Fig. 5.16 and 6.5A). Figure 6.5 addresses some of the problems associated with resolution and node identification.

Manzocchi (2002) and Awdal et al. (2020) plots deformation band networks with a higher X-node proportion than the deformation band networks in this study (Fig. 6.3). Disregarding lithological differences, resolution may explain the different node distribution. Morley & Nixon (2016) suggest that the discrepancy between X-nodes at different resolutions may be due to a more subjective node identification when the data resolution is low (Fig. 6.5). The networks studied in this thesis come from high-resolution images, where you can see details down to a millimeter level. The deformation bands often appear to crosscut each other on a meter scale, but at millimeter-scale, small offsets are often revealed (Fig. 6.5B). Consequently, the X-node proportion will be lower and may explain the high X-node proportion by Manzocchi (2002) and Awdal et al. (2020). Studies of multi-phase fault networks share some similarities where the networks show a high proportion of cross-cutting faults, but still contain low proportions of X-nodes (Duffy et al., 2017). In this case, the X-nodes are not preserved due to displacement on the fault, resulting in two Y-nodes. Applying Morley and Nixon (2016) division of Y-nodes can give a more correct impression of the X-node distribution in a deformation band network. This is done by dividing the Y-nodes into abutting nodes (Ya), splaying nodes (Ys), and crossing nodes (Yc/X) (Morley and Nixon, 2016). This may lead to less misinterpretation of closely spaced Y-nodes as X-nodes at low resolution (Morley and Nixon, 2016, Duffy et al., 2017).

The connectivity of a deformation band network is also affected by the resolution of the data. The ternary diagram (Fig. 6.5A) shows an increasing I-node proportion with lower resolution. An increase in I-nodes will result in a network with more isolated tips, which will reduce the

connectivity. How the deformation bands link together will largely determine the distribution of I-nodes. Deformation bands link through soft- or hard-linkage (Fossen and Hesthammer, 1997), where I-nodes represent soft-linked bands, and hard-linked bands are represented by Y-nodes (Fig. 5.17). At high resolution, the deformation bands appear to link through hard-linkage, but when the resolution becomes poorer, the physical link between the bands often disappears, and they act as soft-linked systems. This may explain the increased proportion in I-nodes and the decreased connectivity in deformation band network SN-4 (1.65 C_b for 1:1, 1.59 C_b for 1:4, and 1.57 C_b for 1:8) at a lower resolution. This coincides with the analysis of fault network by Nixon et al. (2012) where the network appears very unconnected at low resolutions. To fully understand how topological variations are related to resolution, more comparisons are needed.

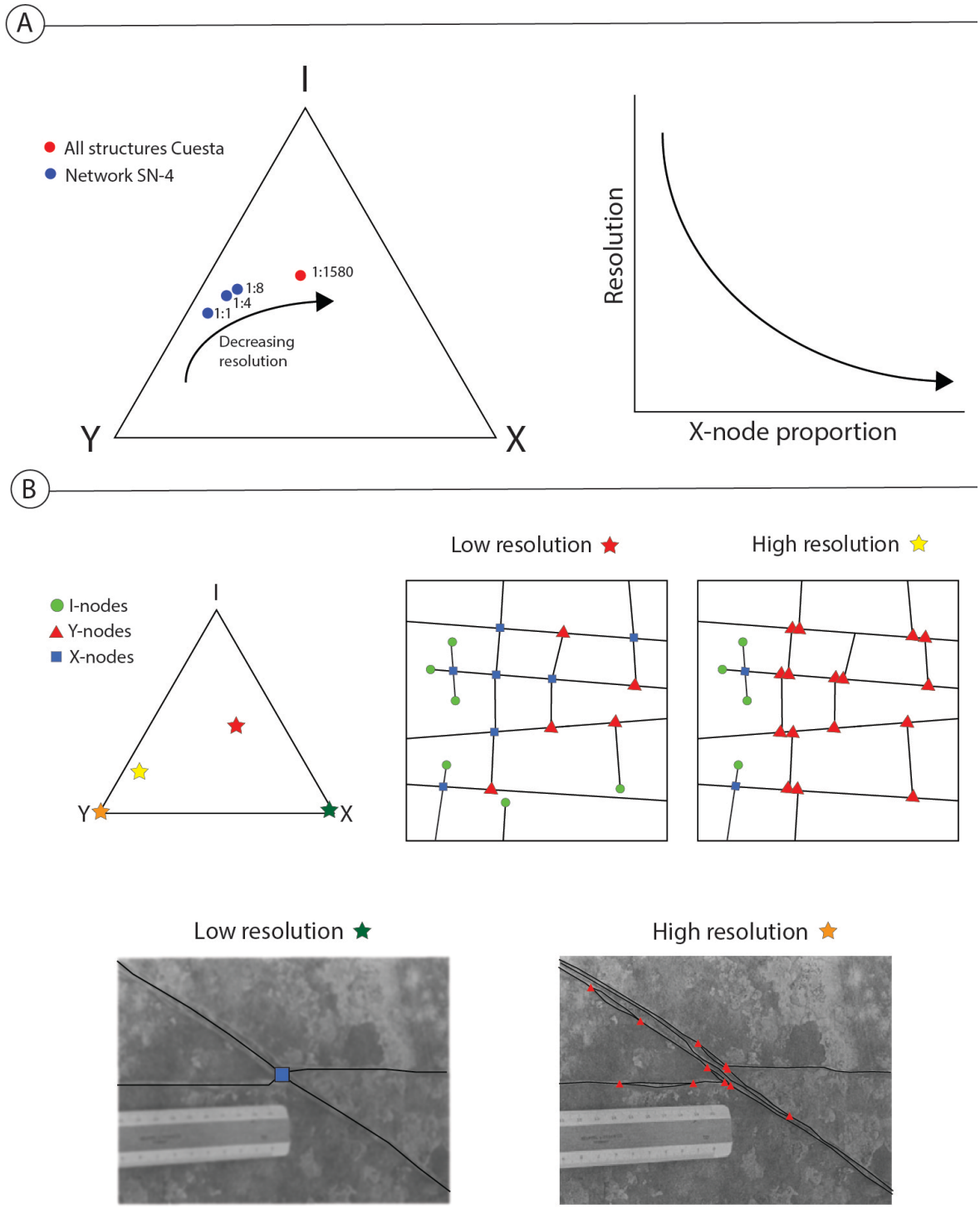

Figure 6.5: The figure present some of the problems associated with resolution and node identification. A) Ternary diagram of I-, Y-, and X-node proportions illustrating the connectivity with decreasing resolution for deformation band network SN-4 (Fig. 5.16) and all structures in the study area (Fig. 5.5). There is a clear trend, where more X-nodes are interpreted with decreasing resolution. The graph illustrates the trend with more X-nodes with lower resolution. B) Synthetic network showing misinterpretation of closely spaced Y-nodes as X-nodes at low resolution. Interpreted set of conjugate deformation bands from Aydin (1978), showing how resolution affects identified nodes. Ternary diagram showing the node topology of the synthetic network and the set of conjugate deformation bands.

7 Conclusions and further work

7.1 Conclusions

This thesis aims to quantify and improve the knowledge of network properties of deformation bands in volcaniclastic rocks. The aims were reached by performing geometrical and topological analyses of high-resolution outcrop photos of deformation band networks in porous volcaniclastic rocks from Shihtiping, South-Eastern Taiwan. From the results and the discussion presented in this thesis, the following conclusions are drawn:

- The topological characteristics of deformation band networks in volcaniclastic rocks have in this study been shown to be dominated by Y-nodes and fully connected (C-C) branches. Nevertheless, there is a slightly higher I-node proportion in the deformation band networks in volcaniclastic rocks compared to networks in sandstones. Cross-cutting deformation bands (X-nodes) rarely occur, but an increasing trend of X-nodes is observed with decreasing resolution. Overall, this results in networks of high average connectivity.
- Compared to other structural networks, this study's deformation band networks have a high proportion of Y-nodes and display limited variation in nodal distribution. This relates to how the deformation bands grow and link together. The topology of fault networks shows a similar nodal distribution and plots along the I-Y axis. X-nodes rarely dominate any structural network.
- The topological evolution of deformation band networks indicates that connectivity develops with maturity. Increased strain is associated with an increased number of deformation bands and connections. Incipient deformation band networks are dominated by I-nodes and low connectivity. Meanwhile, mature deformation band networks and deformation band networks in fully developed faults are dominated by Y-nodes and C-C branches, with high connectivity.
- Topological and geometrical analyses of the deformation bands show that bands' intensity and connectivity are vulnerable to heterogeneities across the network. The variable (deformation band) intensity may influence the fluid flow. High-intensity zones contain more bands and could have the potential to channel fluids and act as barrier or baffle to fluid flow. However, several factors such as deformation band thickness, distribution, geometry, connectivity and the petrophysical properties must be taken into account regarding the band's effect on fluid flow.

7.2 Future work

This study mainly focuses on topological analyses of deformation band network properties in volcaniclastic rocks. Building on this, there are several unanswered questions and suggestions for further work. Some suggestions for improving the understanding of deformation band networks (in volcaniclastic rocks) are listed below:

- The topological analyses in this study are done on two-dimensional data from horizontal outcrops. Investigate the three-dimensional geometry of deformation band network could be done by CT scanning of rock samples or cores. This method will provide the opportunity to study the topology in three dimensions, where branches and nodes will be seen as planes and lines.
- Carry out fieldwork where the focus is on characterize deformation bands within the different (volcaniclastic) stratigraphic units. Look into the controls of stratal properties (grain size, grain types (mineralogy), grain shapes and, porosity) on deformation and (micro) structural style.
- Fracture network's impact on fluid flow can now be investigated using the latest update of NetworkGT 1.0. It would be interesting to use this tool to investigate deformation bands (intensities, connectivity, and geometries) impact on fluid flow across a network. To do this, both host rock and deformation bands' porosity and permeability measurements should be carried out.
- There is still a limited number of studies focusing on deformation bands in volcanic rocks. To improve the understanding, laboratory experiments (e.g. Mair et al., 2000) and more field-based studies investigating the formation and evolution of deformation bands in volcaniclastic rocks should be carried out. This can contribute to fully understand the sequential growth of deformation bands in volcaniclastic rocks and how lithological properties affect deformation.

8 List of references

ACKERMANN, R. V., SCHLISCHE, R. W. & WITHJACK, M. O. 2001. The geometric and statistical evolution of normal fault systems: an experimental study of the effects of mechanical layer thickness on scaling laws. *Journal of Structural Geology,* 23**,** 1803-1819.

ANGELIER, J., CHU, H.-T. & LEE, J.-C. 1997. Shear concentration in a collision zone: kinematics of the Chihshang Fault as revealed by outcrop-scale quantification of active faulting, Longitudinal Valley, eastern Taiwan. *Tectonophysics,* 274**,** 117-143.

ANNUNZIATELLIS, A., BEAUBIEN, S., BIGI, S., CIOTOLI, G., COLTELLA, M. & LOMBARDI, S. 2008. Gas migration along fault systems and through the vadose zone in the Latera caldera (central Italy): Implications for CO2 geological storage. *International Journal of Greenhouse Gas Control,* 2**,** 353-372.

ANTONELLINI, M. & AYDIN, A. 1994. Effect of faulting on fluid flow in porous sandstones: petrophysical properties. *AAPG bulletin,* 78**,** 355-377.

ANTONELLINI, M., PETRACCHINI, L., BILLI, A. & SCROCCA, D. 2014. First reported occurrence of deformation bands in a platform limestone, the Jurassic Calcare Massiccio Fm., northern Apennines, Italy. *Tectonophysics,* 628**,** 85-104.

ANTONELLINI, M. A., AYDIN, A. & POLLARD, D. D. 1994. Microstructure of deformation bands in porous sandstones at Arches National Park, Utah. *Journal of Structural Geology,* 16**,** 941-959.

AWDAL, A., SURAMAIRY, R., SINGH, K., FABRE, G. & ALSOP, G. I. 2020. Deformation bands and their impact on fluid flow: Insights from geometrical modelling and multi-scale flow simulations in sandstones. *Journal of Structural Geology***,** 104215.

AYDIN, A. 1978. Small faults formed as deformation bands in sandstone. *Pure and Applied Geophysics,* 116**,** 913-930.

AYDIN, A. 2000. Fractures, faults, and hydrocarbon entrapment, migration and flow. *Marine and Petroleum Geology,* 17**,** 797-814.

AYDIN, A., BORJA, R. I. & EICHHUBL, P. 2006. Geological and mathematical framework for failure modes in granular rock. *Journal of Structural Geology,* 28**,** 83-98.

AYDIN, A. & JOHNSON, A. M. 1978. Development of faults as zones of deformation bands and as slip surfaces in sandstone. *Pure and Applied Geophysics,* 116**,** 931-942.

AYDIN, A. & JOHNSON, A. M. 1983. Analysis of faulting in porous sandstones. *Journal of Structural Geology,* 5**,** 19-31.

BALLAS, G., FOSSEN, H. & SOLIVA, R. 2015. Factors controlling permeability of cataclastic deformation bands and faults in porous sandstone reservoirs. *Journal of Structural Geology,* 76**,** 1-21.

BARRIER, E. & ANGELIER, J. 1986. Active collision in eastern Taiwan: the Coastal Range. *Tectonophysics,* 125**,** 39-72.

BENSE, V., VAN DEN BERG, E. & VAN BALEN, R. 2003. Deformation mechanisms and hydraulic properties of fault zones in unconsolidated sediments; the Roer Valley Rift System, The Netherlands. *Hydrogeology Journal,* 11**,** 319-332.

BÉSUELLE, P. & RUDNICKI, J. W. 2004. Localization: shear bands and compaction bands. *International Geophysics Series,* 89**,** 219-322.

BOCCALETTI, S., LATORA, V., MORENO, Y., CHAVEZ, M. & HWANG, D.-U. 2006. Complex networks: Structure and dynamics. *Physics reports,* 424**,** 175-308.

BRANDENBURG, J., ALPAK, F. O., SOLUM, J. G. & NARUK, S. J. 2012. A kinematic trishear model to predict deformation bands in a fault-propagation fold, East Kaibab monocline, Utah. *AAPG bulletin,* 96**,** 109-132.

BUCKLEY, S. J., RINGDAL, K., NAUMANN, N., DOLVA, B., KURZ, T. H., HOWELL, J. A. & DEWEZ, T. J. 2019. LIME: Software for 3-D visualization, interpretation, and communication of virtual geoscience models. *Geosphere,* 15**,** 222-235.

CAINE, J. S., EVANS, J. P. & FORSTER, C. B. 1996. Fault zone architecture and permeability structure. *Geology (Boulder),* 24**,** 1025.

CARTWRIGHT, J. A., TRUDGILL, B. D. & MANSFIELD, C. S. 1995. Fault growth by segment linkage: an explanation for scatter in maximum displacement and trace length data from the Canyonlands Grabens of SE Utah. *Journal of Structural Geology,* 17**,** 1319-1326.

CASHMAN, S. & CASHMAN, K. 2000. Cataclasis and deformation-band formation in unconsolidated marine terrace sand, Humboldt County, California. *Geology,* 28**,** 111-114.

CAVAILHES, T. & ROTEVATN, A. 2018. Deformation bands in volcaniclastic rocks–Insights from the Shihtiping tuffs, Coastal Range of Taiwan. *Journal of Structural Geology,* 113**,** 155-175.

CHAI, B. H. 1972. Structure and tectonic evolution of Taiwan. *American Journal of Science,* 272**,** 389-422.

CHANG, C., ANGELIER, J., HUANG, C. & LIU, C. 2001. Structural evolution and significance of a mélange in a collision belt: the Lichi Mélange and the Taiwan arc–continent collision. *Geological Magazine,* 138**,** 633-651.

CHANG, L.-S. 1967. A biostratigraphic study of the Tertiary in the Coastal Range, eastern Taiwan, based on smaller foraminifera (I: Southern Part). *Proceedings of the Geological Society of China,* 10**,** 64-76.

CHARALAMPIDOU, E.-M., HALL, S. A., STANCHITS, S., LEWIS, H. & VIGGIANI, G. 2011. Characterization of shear and compaction bands in a porous sandstone deformed under triaxial compression. *Tectonophysics,* 503**,** 8-17.

CHI, W.-R., NAMSON, J. & SUPPE, J. 1981. Stratigraphic record of plate interactions in the Coastal Range of eastern Taiwan. *Geological Society of China Memoir,* 4**,** 155-194.

CILONA, A., BAUD, P., TONDI, E., AGOSTA, F., VINCIGUERRA, S., RUSTICHELLI, A. & SPIERS, C. J. 2012. Deformation bands in porous carbonate grainstones: Field and laboratory observations. *Journal of Structural Geology,* 45**,** 137-157.

DAS, S. & SCHOLZ, C. H. 1981. Off-fault aftershock clusters caused by shear stress increase? *Bulletin of the Seismological Society of America,* 71**,** 1669-1675.

DAVIS, G. H., BUMP, A. P., GARCÍA, P. E. & AHLGREN, S. G. 2000. Conjugate Riedel deformation band shear zones. *Journal of Structural Geology,* 22**,** 169-190.

DIMMEN, V., ROTEVATN, A., PEACOCK, D. C., NIXON, C. W. & NÆRLAND, K. 2017. Quantifying structural controls on fluid flow: Insights from carbonate-hosted fault damage zones on the Maltese Islands. *Journal of Structural Geology,* 101**,** 43-57.

DINWIDDIE, C. L., BRADBURY, K. K., MCGINNIS, R. N., FEDORS, R. W. & FERRILL, D. A. 2006. Fault Zone Deformation Overprints Permeability of Nonwelded Ignimbrite: Chalk Cove Fault, Bishop Tuff, Bishop, California. *Vadose Zone Journal,* 5**,** 610.

DINWIDDIE, C. L., BRADBURY, K. K., MCGINNIS, R. N., STILLMAN, D. E. & FERRILL, D. A. 2012. Hydrogeologic heterogeneity of faulted and fractured Glass Mountain bedded tuffaceous sediments and ash-fall deposits: The Crucifix site near Bishop, California. *Lithosphere,* 4**,** 40-62.

DU BERNARD, X., EICHHUBL, P. & AYDIN, A. 2002a. Dilation bands: A new form of localized failure in granular media. *Geophysical Research Letters,* 29**,** 29-21.

DU BERNARD, X., LABAUME, P., DARCEL, C., DAVY, P. & BOUR, O. 2002b. Cataclastic slip band distribution in normal fault damage zones, Nubian sandstones, Suez rift. *Journal of Geophysical Research: Solid Earth,* 107.

DUFFY, O. B., NIXON, C. W., BELL, R. E., JACKSON, C. A.-L., GAWTHORPE, R. L., SANDERSON, D. J. & WHIPP, P. S. 2017. The topology of evolving rift fault networks: Single-phase vs multi-phase rifts. *Journal of Structural Geology,* 96**,** 192-202.

EICHHUBL, P., HOOKER, J. N. & LAUBACH, S. E. 2010. Pure and shear-enhanced compaction bands in Aztec Sandstone. *Journal of Structural Geology,* 32**,** 1873-1886.

EVANS, J. P. & BRADBURY, K. K. 2004. Faulting and Fracturing of Nonwelded Bishop Tuff, Eastern California. *Vadose Zone Journal,* 3**,** 602-623.

FISHER, Q. & KNIPE, R. 2001. The permeability of faults within siliciclastic petroleum reservoirs of the North Sea and Norwegian Continental Shelf. *Marine and Petroleum Geology,* 18**,** 1063-1081.

FISHER, R. V. 1961. Proposed classification of volcaniclastic sediments and rocks. *Geological Society of America Bulletin,* 72**,** 1409-1414.

FISHER, R. V. & SMITH, G. A. 1991. Volcanism, tectonics and sedimentation. *In:* FISHER, R. V. & SMITH, G. A. (eds.) *Sedimentation in Volcanic Settings.* Society for Sedimentary Geology.

FOSSEN, H. & BALE, A. 2007. Deformation bands and their influence on fluid flow. *AAPG bulletin,* 91**,** 1685-1700.

FOSSEN, H. & HESTHAMMER, J. 1997. Geometric analysis and scaling relations of deformation bands in porous sandstone. *Journal of Structural Geology,* 19**,** 1479-1493.

FOSSEN, H., HESTHAMMER, J., JOHANSEN, T. E. S. & SYGNABERE, T. O. 2003. Structural geology of the Huldra Field, northern North Sea—a major tilted fault block at the eastern edge of the Horda Platform. *Marine and Petroleum Geology,* 20**,** 1105-1118.

FOSSEN, H., JOHANSEN, T. E. S., HESTHAMMER, J. & ROTEVATN, A. 2005. Fault interaction in porous sandstone and implications for reservoir management; examples from southern Utah. *AAPG bulletin,* 89**,** 1593-1606.

FOSSEN, H. & ROTEVATN, A. 2012. Characterization of deformation bands associated with normal and reverse stress states in the Navajo Sandstone, Utah: Discussion. *AAPG bulletin,* 96**,** 869-876.

FOSSEN, H., SCHULTZ, R. A., SHIPTON, Z. K. & MAIR, K. 2007. Deformation bands in sandstone: a review. *Journal of the Geological Society,* 164**,** 755-769.

FOSSEN, H., SOLIVA, R., BALLAS, G., TRZASKOS, B., CAVALCANTE, C. & SCHULTZ, R. A. 2018. A review of deformation bands in reservoir sandstones: geometries, mechanisms and distribution. *Geological Society, London, Special Publications,* 459**,** SP459. 4.

FOSSEN, H., ZULUAGA, L. F., BALLAS, G., SOLIVA, R. & ROTEVATN, A. 2015. Contractional deformation of porous sandstone: Insights from the Aztec Sandstone, SE Nevada, USA. *Journal of Structural Geology,* 74**,** 172-184.

GIBSON, R. G. 1998. Physical character and fluid-flow properties of sandstone-derived fault zones. *Geological Society, London, Special Publications,* 127**,** 83-97.

HENZA, A. A., WITHJACK, M. O. & SCHLISCHE, R. W. 2010. Normal-fault development during two phases of non-coaxial extension: An experimental study. *Journal of Structural Geology,* 32**,** 1656-1667.

HESTHAMMER, J. & FOSSEN, H. 2001. Structural core analysis from the Gullfaks area, northern North Sea. *Marine and Petroleum Geology,* 18**,** 411-439.

HO, C. 1986. A synthesis of the geologic evolution of Taiwan. *Tectonophysics,* 125**,** 1-16.

HSIEH, M.-L., LIEW, P.-M. & HSU, M.-Y. 2004. Holocene tectonic uplift on the Hua-tung coast, eastern Taiwan. *Quaternary International,* 115**,** 47-70.

HSU, T. 1956. Geology of the coastal range, eastern Taiwan. *Bulletin of the Geological Survey of Taiwan,* 8**,** 39-63.

HUANG, C.-Y., WU, W.-Y., CHANG, C.-P., TSAO, S., YUAN, P. B., LIN, C.-W. & XIA, K.-Y. 1997. Tectonic evolution of accretionary prism in the arc-continent collision terrane of Taiwan. *Tectonophysics,* 281**,** 31-51.

HUANG, C.-Y., YUAN, P. B., LIN, C.-W., WANG, T. K. & CHANG, C.-P. 2000. Geodynamic processes of Taiwan arc–continent collision and comparison with analogs in Timor, Papua New Guinea, Urals and Corsica. *Tectonophysics,* 325**,** 1-21.

HUANG, C.-Y., YUAN, P. B. & TENG, L. S. 1988. Paleontology of the Kangkou Limestone in the middle Coastal Range, eastern Taiwan. *Acta Geologica Taiwanica,* 26**,** 133-160.

HUANG, C.-Y., YUAN, P. B. & TSAO, S.-J. 2006. Temporal and spatial records of active arc-continent collision in Taiwan: A synthesis. *Geological Society of America Bulletin,* 118**,** 274-288.

ISSEN, K. & RUDNICKI, J. 2001. Theory of compaction bands in porous rock. *Physics and Chemistry of the Earth, Part A: Solid Earth and Geodesy,* 26**,** 95-100.

JAHN, B., MARTINEAU, F., PEUCAT, J. & CORNICHET, J. 1986. Geochronology of the Tananao schist complex, Taiwan, and its regional tectonic significance. *Tectonophysics,* 125**,** 103-124.

JERVIDALO, H. 2018. *Structure and evolution of deformation-band-dominated faults in porous volcaniclastic rocks. Insights from Eastern Taiwan.* MSc. Thesis, University of Bergen.

KJENES, M. 2018. *The geometry and evolution of deformation bands in volcaniclastic rocks: insights from Eastern Taiwan.* MSc. Thesis, University of Bergen.

KNIPE, R., FISHER, Q., JONES, G., CLENNELL, M., FARMER, A., HARRISON, A., KIDD, B., MCALLISTER, E., PORTER, J. & WHITE, E. 1997. Fault seal analysis: successful methodologies, application and future directions. *In:* MØLLER-PEDERSEN, P. & KOESTLER, A. G. (eds.) *Hydrocarbon Seals: Importance for Exploration and Production.* Norwegian Petroleum Society Special Publications.

KOSTROV, B. V. & DAS, S. 1988. *Principles of earthquake source mechanics*, Cambridge University Press.

LAI, Y.-M. & SONG, S.-R. 2013. The volcanoes of an oceanic arc from origin to destruction: A case from the northern Luzon Arc. *Journal of Asian Earth Sciences,* 74**,** 97-112.

LALLEMAND, S., FONT, Y., BIJWAARD, H. & KAO, H. 2001. New insights on 3-D plates interaction near Taiwan from tomography and tectonic implications. *Tectonophysics,* 335**,** 229-253.

LATORA, V. & MARCHIORI, M. 2002. Is the Boston subway a small-world network? *Physica A: Statistical Mechanics and its Applications,* 314**,** 109-113.

LEE, J.-C., ANGELIER, J., CHU, H.-T., HU, J.-C. & JENG, F.-S. 2001. Continuous monitoring of an active fault in a plate suture zone: a creepmeter study of the Chihshang Fault, eastern Taiwan. *Tectonophysics,* 333**,** 219-240.

LENHARDT, N. & GÖTZ, A. E. 2011. Volcanic settings and their reservoir potential: An outcrop analog study on the Miocene Tepoztlán Formation, Central Mexico. *Journal of Volcanology and Geothermal Research,* 204**,** 66-75.

LEVEILLE, G. P., KNIPE, R., MORE, C., ELLIS, D., DUDLEY, G., JONES, G., FISHER, Q. J. & ALLINSON, G. 1997. Compartmentalization of Rotliegendes gas reservoirs by sealing faults, Jupiter Fields area, southern North Sea. *Geological Society, London, Special Publications,* 123**,** 87-104.

LIN, A., WATTS, A. & HESSELBO, S. 2003. Cenozoic stratigraphy and subsidence history of the South China Sea margin in the Taiwan region. *Basin Research,* 15**,** 453-478.

LIN, S. & HUANG, W. Study of Deformation Bands in Ignimbrites in Shihtiping, Eastern Taiwan. AGU Fall Meeting Abstracts, 2014.

LOTHE, A., GABRIELSEN, R., HAGEN, N. B. & LARSEN, B. 2002. An experimental study of the texture of deformation bands: effects on the porosity and permeability of sandstones. *Petroleum Geoscience,* 8**,** 195-207.

LU, C. & HSU, K. 1992. Tectonic evolution of the Taiwan mountain belt. *Petroleum Geology of Taiwan,* 27**,** 21-46.

LU, C.-Y. & MALAVIEILLE, J. 1994. Oblique convergence, indentation and rotation tectonics in the Taiwan Mountain Belt: Insights from experimental modelling. *Earth and Planetary Science Letters,* 121**,** 477-494.

MAIR, K., MAIN, I. & ELPHICK, S. 2000. Sequential growth of deformation bands in the laboratory. *Journal of Structural Geology,* 22**,** 25-42.

MALAVIEILLE, J., LALLEMAND, S. E., DOMINGUEZ, S., DESCHAMPS, A., LU, C.-Y., LIU, C.-S., SCHNURLE, P. & CREW, A. S. 2002. Arc-continent collision in Taiwan: New marine observations and tectonic evolution. *Special Papers - Geological Society of America***,** 187-211.

MALAVIEILLE, J. & TRULLENQUE, G. 2009. Consequences of continental subduction on forearc basin and accretionary wedge deformation in SE Taiwan: Insights from analogue modeling. *Tectonophysics,* 466**,** 377-394.

MANZOCCHI, T. 2002. The connectivity of two-dimensional networks of spatially correlated fractures. *Water Resources Research,* 38**,** 1-1-1-20.

MANZOCCHI, T., RINGROSE, P. S. & UNDERHILL, J. 1998. Flow through fault systems in high-porosity sandstones. *Geological Society, London, Special Publications,* 127**,** 65-82.

MAULDON, M., DUNNE, W. M. & ROHRBAUGH, M. B. 2001. Circular scanlines and circular windows: new tools for characterizing the geometry of fracture traces. *Journal of Structural Geology,* 23**,** 247-258.

MCGINNIS, R. N., MORRIS, A. P., FERRILL, D. A. & DINWIDDIE, C. L. 2009. Deformation analysis of tuffaceous sediments in the Volcanic Tableland near Bishop, California. *Lithosphere,* 1**,** 291-304.

MOLLEMA, P. & ANTONELLINI, M. 1996. Compaction bands: a structural analog for anti-mode I cracks in aeolian sandstone. *Tectonophysics,* 267**,** 209-228.

MOON, V. G. 1993. Geotechnical characteristics of ignimbrite: A soft pyroclastic rock type. *Engineering Geology,* 35**,** 33-48.

MOON, V. G. 1993b. Microstructural controls on the geomechanical behaviour of ignimbrite. *Engineering Geology,* 35**,** 19-31.

MORLEY, C. & NIXON, C. 2016. Topological characteristics of simple and complex normal fault networks. *Journal of Structural Geology,* 84**,** 68-84.

MÄKEL, G. 2007. The modelling of fractured reservoirs: constraints and potential for fracture network geometry and hydraulics analysis. *Geological Society, London, Special Publications,* 292**,** 375-403.

NICCHIO, M. A., NOGUEIRA, F. C., BALSAMO, F., SOUZA, J. A., CARVALHO, B. R. & BEZERRA, F. H. 2017. Development of cataclastic foliation in deformation bands in feldspar-rich conglomerates of the Rio do Peixe Basin, NE Brazil. *Journal of Structural Geology*.

NICOL, A., WALSH, J., WATTERSON, J. & BRETAN, P. 1995. Three-dimensional geometry and growth of conjugate normal faults. *Journal of Structural Geology,* 17**,** 847-862.

NIXON, C. W. 2013. *Analysis of fault networks and conjugate systems.* Doctoral dissertation, University of Southampton.

NIXON, C. W., SANDERSON, D. J. & BULL, J. M. 2012. Analysis of a strike-slip fault network using high resolution multibeam bathymetry, offshore NW Devon UK. *Tectonophysics,* 541**,** 69-80.

NYBERG, B., NIXON, C. W. & SANDERSON, D. J. 2018. NetworkGT: A GIS tool for geometric and topological analysis of two-dimensional fracture networks. *Geosphere,* 14**,** 1618-1634.

OGILVIE, S. R. & GLOVER, P. W. 2001. The petrophysical properties of deformation bands in relation to their microstructure. *Earth and Planetary Science Letters,* 193**,** 129-142.

OKUBO, C. H. 2012. Spatial distribution of damage around faults in the Joe Lott Tuff Member of the Mount Belknap Volcanics, Utah: A mechanical analog for faulting in pyroclastic deposits on Mars. *Journal of Geophysical Research: Planets,* 117.

ORTEGA, O. & MARRETT, R. 2000. Prediction of macrofracture properties using microfracture information, Mesaverde Group sandstones, San Juan basin, New Mexico. *Journal of Structural Geology,* 22**,** 571-588.

PAGE, B. M. & SUPPE, J. 1981. The Pliocene Lichi melange of Taiwan; its plate-tectonic and olistostromal origin. *American Journal of Science,* 281**,** 193-227.

PEACOCK, D. 2001. The temporal relationship between joints and faults. *Journal of Structural Geology,* 23**,** 329-341.

PEACOCK, D. C. P., DIMMEN, V., ROTEVATN, A. & SANDERSON, D. J. 2017. A broader classification of damage zones. *Journal of structural geology,* 102**,** 179-192.

PROCTER, A. & SANDERSON, D. J. 2018. Spatial and layer-controlled variability in fracture networks. *Journal of Structural Geology,* 108**,** 52-65.

RATH, A., EXNER, U., TSCHEGG, C., GRASEMANN, B., LANER, R. & DRAGANITS, E. 2011. Diagenetic control of deformation mechanisms in deformation bands in a carbonate grainstone. *AAPG bulletin,* 95**,** 1369-1381.

RAWLING, G. C. & GOODWIN, L. B. 2003. Cataclasis and particulate flow in faulted, poorly lithified sediments. *Journal of Structural Geology,* 25**,** 317-331.

RILEY, P. R., GOODWIN, L. B. & LEWIS, C. J. 2010. Controls on fault damage zone width, structure, and symmetry in the Bandelier Tuff, New Mexico. *Journal of Structural Geology,* 32**,** 766-780.

ROTEVATN, A., BUCKLEY, S. J., HOWELL, J. A. & FOSSEN, H. 2009a. Overlapping faults and their effect on fluid flow in different reservoir types: A LIDAR-based outcrop modeling and flow simulation study. *AAPG bulletin,* 93**,** 407-427.

ROTEVATN, A. & FOSSEN, H. 2011. Simulating the effect of subseismic fault tails and process zones in a siliciclastic reservoir analogue: Implications for aquifer support and trap definition. *Marine and Petroleum Geology,* 28**,** 1648-1662.

ROTEVATN, A., SANDVE, T., KEILEGAVLEN, E., KOLYUKHIN, D. & FOSSEN, H. 2013. Deformation bands and their impact on fluid flow in sandstone reservoirs: the role of natural thickness variations. *Geofluids,* 13**,** 359-371.

ROTEVATN, A., THORSHEIM, E., BASTESEN, E., FOSSMARK, H. S. S., TORABI, A. & SÆLEN, G. 2016. Sequential growth of deformation bands in carbonate grainstones in the hangingwall of an active growth fault: Implications for deformation mechanisms in different tectonic regimes. *Journal of Structural Geology,* 90**,** 27-47.

ROTEVATN, A., TORABI, A., FOSSEN, H. & BRAATHEN, A. 2008. Slipped deformation bands: A new type of cataclastic deformation bands in Western Sinai, Suez rift, Egypt. *Journal of Structural Geology,* 30**,** 1317-1331.

ROTEVATN, A., TVERANGER, J., HOWELL, J. & FOSSEN, H. 2009b. Dynamic investigation of the effect of a relay ramp on simulated fluid flow: geocellular modelling of the Delicate Arch Ramp, Utah. *Petroleum Geoscience,* 15**,** 45-58.

SANDERSON, D. J. & NIXON, C. W. 2015. The use of topology in fracture network characterization. *Journal of Structural Geology,* 72**,** 55-66.

SANDERSON, D. J. & ZHANG, X. 1999. Critical stress localization of flow associated with deformation of well-fractured rock masses, with implications for mineral deposits. *Geological Society, London, Special Publications,* 155**,** 69-81.

SCHUELLER, S., BRAATHEN, A., FOSSEN, H. & TVERANGER, J. 2013. Spatial distribution of deformation bands in damage zones of extensional faults in porous

sandstones: Statistical analysis of field data. *Journal of Structural Geology,* 52**,** 148-162.

SCHUTTER, S. R. 2003. Hydrocarbon occurrence and exploration in and around igneous rocks. *Geological Society, London, Special Publications,* 214**,** 7-33.

SHIPTON, Z. K. & COWIE, P. A. 2001. Damage zone and slip-surface evolution over μm to km scales in high-porosity Navajo sandstone, Utah. *Journal of structural geology,* 23**,** 1825-1844.

SHIPTON, Z. K. & COWIE, P. A. 2003. A conceptual model for the origin of fault damage zone structures in high-porosity sandstone. *Journal of Structural Geology,* 25**,** 333-344.

SIBUET, J. & HSU, S. 2004. How was Taiwan created? *Tectonophysics,* 379**,** 159-181.

SODEN, A. M. & SHIPTON, Z. K. 2013. Dilational fault zone architecture in a welded ignimbrite: The importance of mechanical stratigraphy. *Journal of Structural Geology,* 51**,** 156-166.

SOLIVA, R., SCHULTZ, R. A., BALLAS, G., TABOADA, A., WIBBERLEY, C., SAILLET, E. & BENEDICTO, A. 2013. A model of strain localization in porous sandstone as a function of tectonic setting, burial and material properties; new insight from Provence (southern France). *Journal of Structural Geology,* 49**,** 50-63.

SONG, S., LO, H. & CHEN, W. 1994. Origin of clastic dikes in the Coastal Range, eastern Taiwan with implications for sedimentary processes during the arc-continent collision. *Journal of the Geological Society of China,* 37**,** 407-424.

SONG, S.-R. & LO, H.-J. 1988. Volcanic geology of Fengpin-Takangkou area, coastal range of Taiwan. *Acta Geologica Taiwanica***,** 223-235.

SONG, S.-R. & LO, H.-J. 2002. Lithofacies of volcanic rocks in the central Coastal Range, eastern Taiwan: implications for island arc evolution. *Journal of Asian Earth Sciences,* 21**,** 23-38.

STERNLOF, K. R., KARIMI-FARD, M., POLLARD, D. & DURLOFSKY, L. 2006. Flow and transport effects of compaction bands in sandstone at scales relevant to aquifer and reservoir management. *Water Resources Research,* 42.

SUPPE, J. 1980. Imbricated structure of western foothills belt, southcentral Taiwan. *Petroleum Geology of Taiwan,* 17**,** 1-16.

TAYLOR, B. & HAYES, D. E. 1983. Origin and history of the South China Sea basin. *Geophysical Monograph Series,* 27**,** 23-56.

TENG, L. & LO, H.-J. 1985. Sedimentary sequences in the island arc settings of the Coastal Range, eastern Taiwan. *Acta Geologica Taiwanica***,** 77-98.

TENG, L. S. 1990. Geotectonic evolution of late Cenozoic arc-continent collision in Taiwan. *Tectonophysics,* 183**,** 57-76.

TENG, L. S. 1996. Extensional collapse of the northern Taiwan mountain belt. *Geology,* 24**,** 949-952.

TENG, L. S., CHEN, W.-S., WANG, Y., SONG, S.-R. & LO, H.-J. 1988. Toward a comprehensive stratigraphic system of the Coastal Range, eastern Taiwan. *Acta Geologica Taiwanica,* 26**,** 19-36.

TENG, L. S. & WANG, Y. 1981. Island arc system of the Coastal Range, eastern Taiwan. *Proceedings of the Geological Society of China,* 24**,** 99-112.

TEUFEL, L. 1981. Pore volume changes during frictional sliding of simulated faults. *Geophysical Monograph Series,* 24**,** 135-145.

THIELE, S. T., JESSELL, M. W., LINDSAY, M., OGARKO, V., WELLMANN, J. F. & PAKYUZ-CHARRIER, E. 2016. The topology of geology 1: Topological analysis. *Journal of Structural Geology,* 91**,** 27-38.

THOMAS, M. Y., AVOUAC, J.-P., GRATIER, J.-P. & LEE, J.-C. 2014a. Lithological control on the deformation mechanism and the mode of fault slip on the Longitudinal Valley Fault, Taiwan. *Tectonophysics,* 632**,** 48-63.

THOMAS, M. Y., AVOUAC, J. P., CHAMPENOIS, J., LEE, J. C. & KUO, L. C. 2014b. Spatiotemporal evolution of seismic and aseismic slip on the Longitudinal Valley Fault, Taiwan. *Journal of Geophysical Research: Solid Earth,* 119**,** 5114-5139.

TINDALL, S. & ECKERT, A. 2015. Geometric and mechanical-stiffness controls on jointing in cataclastic deformation bands. *Journal of Structural Geology,* 77**,** 126-137.

TONDI, E., ANTONELLINI, M., AYDIN, A., MARCHEGIANI, L. & CELLO, G. 2006. The role of deformation bands, stylolites and sheared stylolites in fault development in carbonate grainstones of Majella Mountain, Italy. *Journal of structural geology,* 28**,** 376-391.

TONDI, E., CILONA, A., AGOSTA, F., AYDIN, A., RUSTICHELLI, A., RENDA, P. & GIUNTA, G. 2012. Growth processes, dimensional parameters and scaling relationships of two conjugate sets of compactive shear bands in porous carbonate grainstones, Favignana Island, Italy. *Journal of Structural Geology,* 37**,** 53-64.

TORABI, A. 2014. Cataclastic bands in immature and poorly lithified sandstone, examples from Corsica, France. *Tectonophysics,* 630**,** 91-102.

TORABI, A. & FOSSEN, H. 2009. Spatial variation of microstructure and petrophysical properties along deformation bands in reservoir sandstones. 93**,** 919-938.

TORABI, A., FOSSEN, H. & BRAATHEN, A. 2013. Insight into petrophysical properties of deformed sandstone reservoirs. *AAPG bulletin,* 97**,** 619-637.

VAN DER MEER, J. J., MENZIES, J. & ROSE, J. 2003. Subglacial till: the deforming glacier bed. *Quaternary Science Reviews,* 22**,** 1659-1685.

WALDERHAUG, O. 1996. Kinetic modeling of quartz cementation and porosity loss in deeply buried sandstone reservoirs. *AAPG bulletin,* 80**,** 731-745.

WALKER, G. P. 1983. Ignimbrite types and ignimbrite problems. *Journal of Volcanology and Geothermal Research,* 17**,** 65-88.

WALKER, R., HOLDSWORTH, R., IMBER, J., FAULKNER, D. & ARMITAGE, P. 2013. Fault zone architecture and fluid flow in interlayered basaltic volcaniclastic-crystalline sequences. *Journal of Structural Geology,* 51**,** 92-104.

WALSH, J., CHILDS, C., IMBER, J., MANZOCCHI, T., WATTERSON, J. & NELL, P. 2003. Strain localisation and population changes during fault system growth within the Inner Moray Firth, Northern North Sea. *Journal of Structural Geology,* 25**,** 307-315.

WATKINS, H., BOND, C. E., HEALY, D. & BUTLER, R. W. 2015. Appraisal of fracture sampling methods and a new workflow to characterise heterogeneous fracture networks at outcrop. *Journal of Structural Geology,* 72**,** 67-82.

WILSON, J. E. 2004. *Characteristics of faults in nonwelded ignimbrites from the Pajarito Plateau and implications for fluid flow.* Doctoral dissertation, New Mexico Institute of Mining and Technology.

WILSON, J. E., GOODWIN, L. B. & LEWIS, C. J. 2003. Deformation bands in nonwelded ignimbrites: Petrophysical controls on fault-zone deformation and evidence of preferential fluid flow. *Geology,* 31**,** 837-840.

WILSON, J. E., GOODWIN, L. B. & LEWIS, C. J. 2006. Diagenesis of deformation band faults: Record and mechanical consequences of vadose zone flow and transport in the Bandelier Tuff, Los Alamos, New Mexico. *Journal of Geophysical Research,* 111.

WILSON, P. I., WILSON, R. W., SANDERSON, D. J., JARVIS, I. & MCCAFFREY, K. J. 2020. Analysis of deformation bands associated with the Trachyte Mesa intrusion, Henry Mountains, Utah: implications for reservoir connectivity and fluid flow around sill intrusions. *Solid Earth Discussions***,** 1-36.

WOLFE, J. 1981. Philippine geochronology. *Journal of Geological Society of Philippines,* 35**,** 1-30.

WONG, T. F., DAVID, C. & ZHU, W. 1997. The transition from brittle faulting to cataclastic flow in porous sandstones: Mechanical deformation. *Journal of Geophysical Research: Solid Earth,* 102**,** 3009-3025.

YU, H.-S. & CHOU, Y.-W. 2001. Characteristics and development of the flexural forebulge and basal unconformity of Western Taiwan Foreland Basin. *Tectonophysics,* 333**,** 277-291.

YUI, T., MAKI, K., LAN, C., HIRATA, T., CHU, H., KON, Y., YOKOYAMA, T., JAHN, B. & ERNST, W. 2012. Detrital zircons from the Tananao metamorphic complex of Taiwan: Implications for sediment provenance and Mesozoic tectonics. *Tectonophysics,* 541**,** 31-42.

ZHU, W., BAUD, P., VINCIGUERRA, S. & WONG, T. F. 2011. Micromechanics of brittle faulting and cataclastic flow in Alban Hills tuff. *Journal of Geophysical Research: Solid Earth,* 116.

ZULUAGA, L. F., ROTEVATN, A., KEILEGAVLEN, E. & FOSSEN, H. 2016. The effect of deformation bands on simulated fluid flow within fault-propagation fold trap types: Lessons from the San Rafael monocline, Utah. *AAPG bulletin,* 100**,** 1523-1540.

Appendix

Appendix I: Abbreviations and calculations in NetworkGT

Appendix I: Summary of parameters, abbreviations, and formulas used in the topology parameter tool in NetworkGT, modified from Nyberg et al. (2018). For a more detailed description, see: Nyberg et al. (2018) – "NetworkGT: A GIS tool for geometric and topological analysis of two-dimensional fracture networks".

Parameter	Description	Calculation
Area (A)	Sample Area	A
Number of nodes (N_n)	Number of I-, Y- and X-nodes	$N_I + N_Y + N_X$
Number of connections (N_C)	Number of X- and Y-nodes	$N_Y + N_X$
Number of edge nodes (N_E)	Number of E-nodes	N_E
Number of branches (node calculation) (N_B)	Number of branches, calculated from nodes	$\frac{N_I + 3N_Y + 4N_X}{2}$
Number of lines (N_L)	Number of lines, calculated from nodes	$\frac{N_I + 2N_Y}{2}$
Connect/line (C_L)	Connections per line	$\frac{2(N_Y + N_X)}{N_L}$
Connections/branch (C_B)	Connections per branch	$\frac{3N_Y + 4N_X}{N_B}$
Total trace length (Σ_L)	Sum of all branch lengths	ΣL
Average line length (L_C)	Average line length	$\frac{\Sigma L}{N_L}$
Average branch length (B_C)	Average branch length	$\frac{\Sigma L}{N_B}$
Connecting node frequency	Frequency of connecting nodes within the sample area	$\frac{N_C}{A}$
Branch frequency	Frequency of branches within the sample area	$\frac{N_B}{A}$
Line frequency	Frequency of lines within sample area	$\frac{N_L}{A}$
2D intensity (P_{21})	Intensity of deformation bands within a sample area	$\frac{\Sigma L}{A}$
Dimensionless intensity (P_{22})	Product of average branch length and intensity	$P_{21} \cdot L_B$
Number of branches (branch calculation) (N_B)	Number of C-C, C-I and I-I branches	$N_{CC} + N_{IC} + N_{II}$

Appendix II: Topological and geometrical and data

Appendix II: Topological and geometrical data from the study area. For deformation band network position see Figure 4.3.

Deformation band network	Circumference (m)	Area (m^2)	E	I	X	Y	No. Nodes	No. Branches	No. Lines	No. Connections	Connect/L	Average Line Length (m)
Cuesta (All structures)	1023,8643	11855.06346	51	284	136	157	577	649.5	220.5	293	2.65760	13.88831
Fault 1 nr1	22,77201	3.42548	2	149	13	153	315	330	151	166	2.19868	0.25698
Fault 1 nr2	21,18808	2.61226	78	140	57	720	917	1264	430	777	3.61395	0.26614
Fault 2 nr1	3.98610	0.48657	28	206	16	306	528	594	256	322	2.51562	0.12208
Fault 2 nr2	5,72162	0.68686	42	173	13	241	427	474	207	254	2.45411	0.17258
SN-1 (sinistral network 1)	27,09113	12.89676	28	52	3	138	193	239	95	141	2.96842	1.06164
SN-2 (sinistral network 2) DB2	3,35566	0.31007	21	48	1	101	150	177.5	74.5	102	2.73826	0.19052
SN-2 (sinistral network 2) DB2	3,91896	0.42185	22	51	1	133	185	227	92	134	2.91304	0.2095
SN-2 (sinistral network 2) DB3	6,253	0.77529	42	89	5	174	268	315.5	131.5	179	2.72243	0.26175
SN-2 (sinistral network 2) DB4	5,36013	0.53215	10	25	1	65	91	112	45	66	2.93333	0.28113
SN-3 (sinistral network 3)	25,39457	6.645400	18	78	6	188	272	333	133	194	2.91729	0.39288
SN-4 (sinistral network 4)	24,51396	4.68526	81	335	36	486	857	968.5	410.5	522	2.54324	0.20507
DN-2 (dextral network 2)	5,46654	1.19514	6	60	2	100	162	184	80	102	2.550	0.20372
DN-3 (dextral network 3)	11,07394	1.73170	20	29	3	57	89	106	43	60	2.79070	0.52843
IDBN1 (incipient network 1)	7,78809	1.13196	0	8	0	4	12	10	6	4	1.33333	0.6262
IDBN2 (incipient network 2)	7,97464	1.27117	0	10	0	8	18	17	9	8	1.77778	0.49474

Deformation band network	Average Branch Length (m)	Connect/B	Branch Freq	Line Freq	NcFreq	2D Intensity (m^-1)	Dimensionless Intensity	C - C	C - I	I - I	Total Trace Length (m)
Cuesta (All structures)	4.71497	1.56274	0.05479	0.0186	0.02472	0.25832	1.21796	366	266	17.50	3062.37326
Fault 1 nr1	0.11759	1.54848	96.33692	44.08144	48.46039	11.32805	1.33204	195	80	35	38.804
Fault 1 nr2	0.09054	1.88924	483.8723	164.60846	297.44366	43.80932	3.96645	1106.5	146.5	12	114.4413
Fault 2 nr1	0.05261	1.65320	1220.78865	526.13114	661.77432	64.22782	3.37914	399	172	23	31.25137
Fault 2 nr2	0.07537	1.63502	690.09213	301.36935	369.79621	52.01028	3.91987	307	143	24	35.72403
SN-1 (sinistral network 1)	0.42199	1.78243	18.53178	7.36619	10.93298	7.82024	3.30006	178	59.5	1,50	100.85571
SN-2 (sinistral network 2) DB2	0.07997	1.72958	572.45358	240.26925	328.95924	45.77697	3.66061	125	48.5	4	14.19401
SN-2 (sinistral network 2) DB2	0.08491	1.77533	538.10763	218.08767	317.64944	45.68961	3.87941	173	50	4	19.2741
SN-2 (sinistral network 2) DB3	0.1091	1.71791	406.94426	169.61385	230.88121	44.39653	4.84354	214	94.5	7	34.42021
SN-2 (sinistral network 2) DB4	0.11295	1.77679	210.46564	84.56209	124.02439	23.77293	2.68525	86	22.50	3.50	12.65084
SN-3 (sinistral network 3)	0.15692	1.76577	50.10987	20.01385	29.19314	7.86311	1.23386	257	69	7	52.25351
SN-4 (sinistral network 4)	0.08692	1.65410	206.71227	87.61527	111.41332	17.96762	1.56176	659.5	251.5	57.5	84.18289
DN-2 (dextral network 2)	0.09228	1.67391	153.95628	66.93751	85.34533	13.55113	1.25053	125	55	11	16.19555
DN-3 (dextral network 3)	0.21436	1.72642	61.21164	24.83114	34.6481	13.12143	2.81273	72	30	4	22.72234
IDBN1 (incipient network 1)	0.37572	1.20000	8.83423	5.30054	3.53369	3.31922	1.24710	4	4	2	3.75722
IDBN2 (incipient network 2)	0.26192	1.41176	13.37353	7.0801	6.29343	3.50280	0.91745	8	8	1	4.45264

Appendix II: Topological and geometrical data from deformation band network SN-4, interpreted on different scales.

Deformation band network (SN-4)	Circumference (m)	Area (m^2)	E	I	X	Y	No. Nodes	No. Branches	No. Lines	No. Connections	Connect/L	Average Line Length (m)
Scale 1:1	24.51396	4.68526	81	335	36	486	857	968.5	410.5	522	2.54324	0.20507
Scale 1:4	24.51396	4.68526	61	158	23	175	356	387.5	166.5	198	2.37838	0.37717
Scale 1:8	24.51396	4.68526	43	87	14	88	189	203.5	87.5	102	2.33143	0.49644

Deformation band network (SN-4)	Average Branch Length (m)	Connect/B	Branch Freq	Line Freq	NcFreq	2D Intensity (m^-1)	Dimensionless Intensity	C - C	C - I	I - I	Total Trace Length (m)
Scale 1:1	0.08692	1.65410000	206.71227	87.61527	111.41332	17.96762	1.56176	659.5	251.5	57.5	84.18289
Scale 1:4	0.16206	1.59226	82.70625	35.53701	42.26023	13.40361	2.17223	241	117	29.5	62.79935
Scale 1:8	0.21346	1.57248	43.43412	18.67561	21.77042	9.27133	1.97903	117.5	71	15	43.43857

Appendix III: Additional figures of deformation band networks

Appendix III: Figure summarizing the deformation band network along Fault 1.

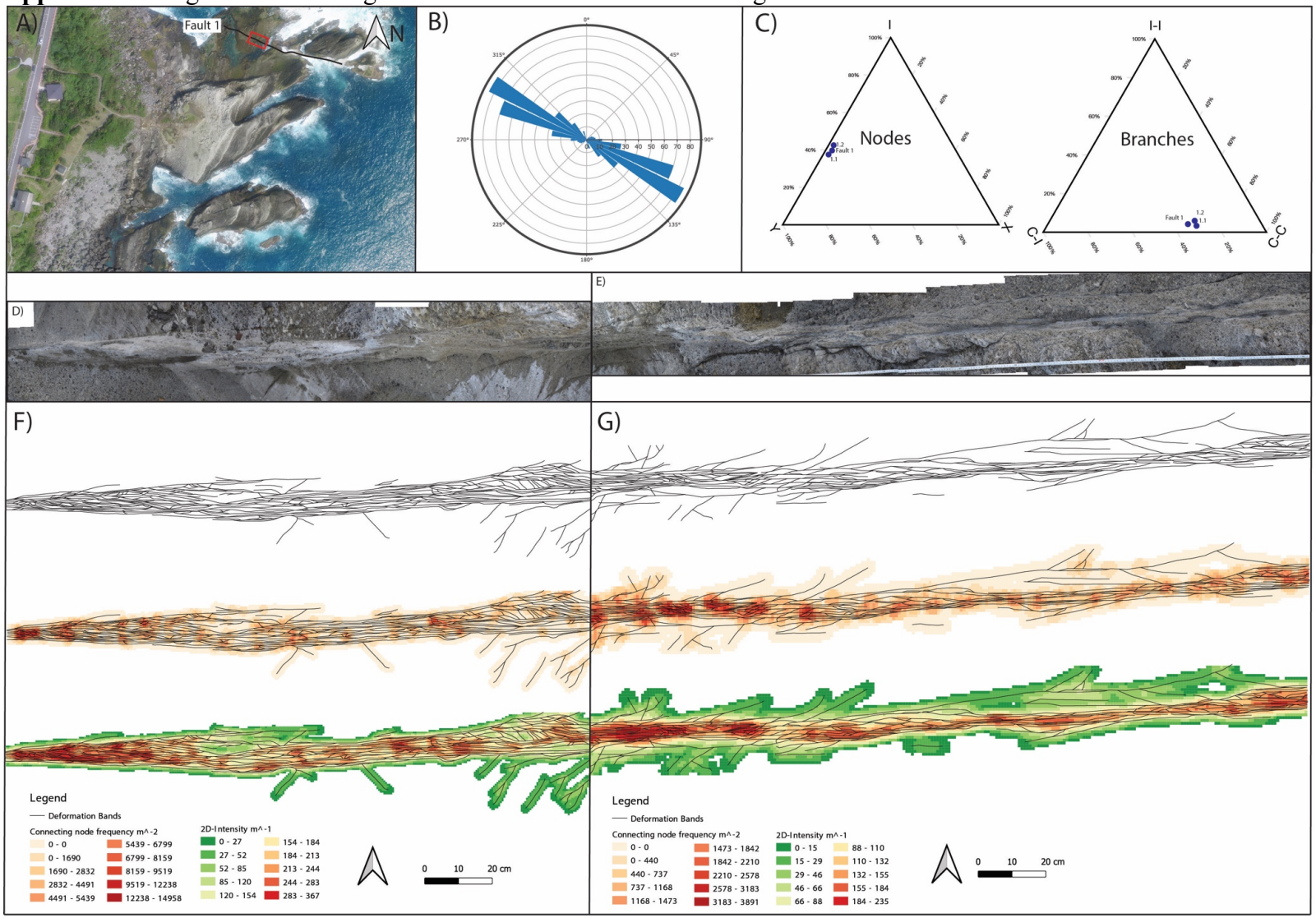

A) Unmanned Aerial Vehicle (UAV) photo of the study area. Fault 1 (northern fault) is marked as a black line, red box indicates where the close-up photos were taken. B) Rose diagram showing deformation band orientations of Fault 1. D) Close-up photo of Section 1.1 (Fault 1). E) Close-up photo of Section 1.2 (Fault 1). F) Digitized deformation band network, connecting node frequency map and 2D-intensity map, of Section 1.1. G) Digitized deformation band network, connecting node frequency map and 2D-intensity map, of Section 1.2.

Note different values for connecting node frequency and 2D-intensity for F and G.

Appendix III: Figure of deformation band network SN-4, showing the area (red box) of the network.

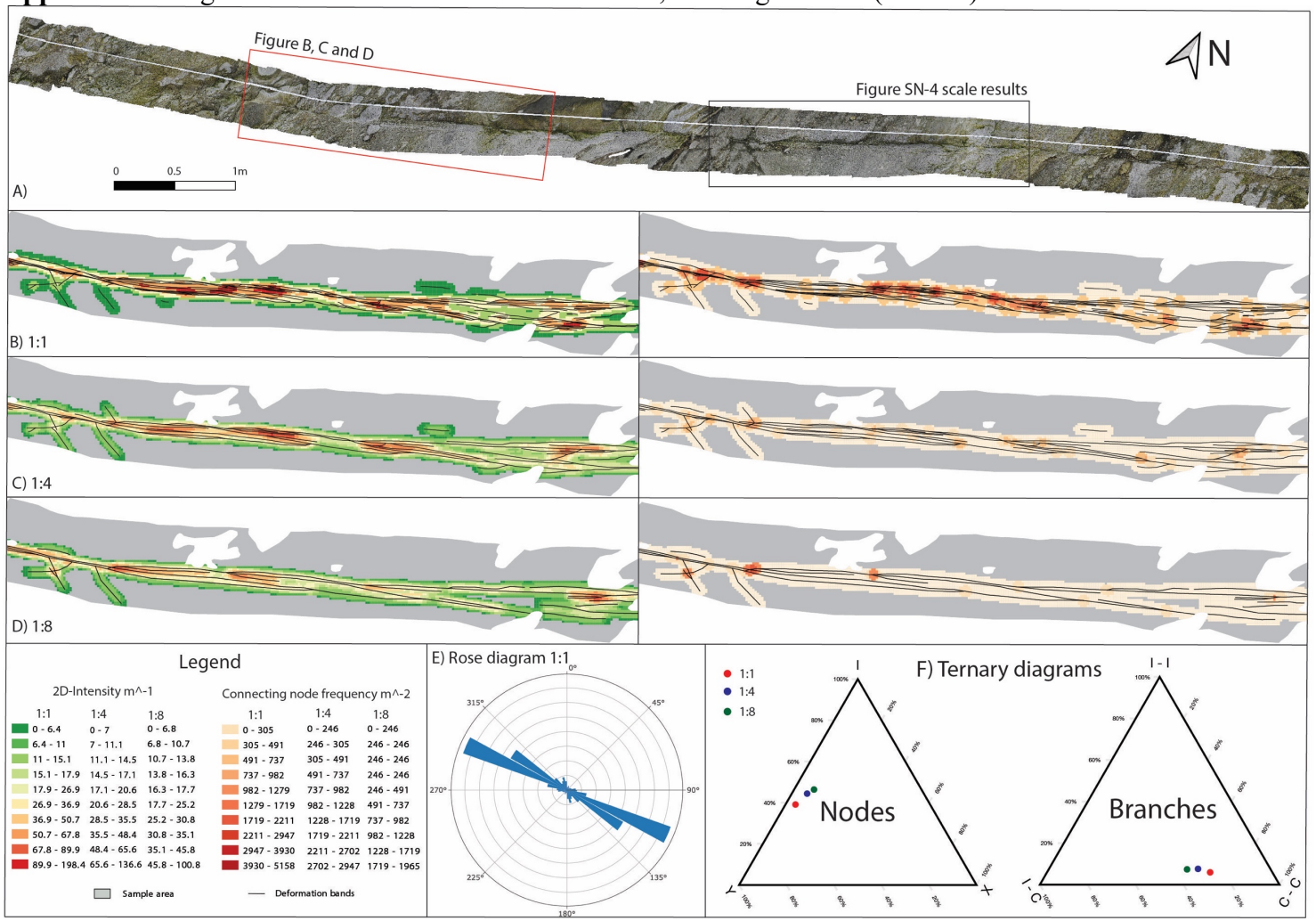

A) SN-1 is made of 105 close-up images merged together into a high-resolution model. The red box marks the placement of figure B, C and D. Black box marks the placement of Figure 5.16B, C and D. B) Deformation band intensity map and connecting node frequency map of the SN-4 network mapped at 1:1 scale. Note, grid size 0.01x0.001 m and sampling radius 0.03 m are the same for all networks, but the contour intervals vary. C) Deformation band intensity map and connecting node frequency map of the SN-4 network mapped at 1:4 scale. D) Deformation band intensity map and connecting node frequency map of the SN-4 network mapped at 1:8 scale. E) Rose diagram showing the orientation of the deformation bands mapped at 1:1 scale. F) Ternary diagram displaying the node and branch distribution of the SN-4 network mapped at different scales: 1:1 (red), 1:4 (blue) and 1:8 (green).

Appendix III: Summary of deformation band network SN-2.

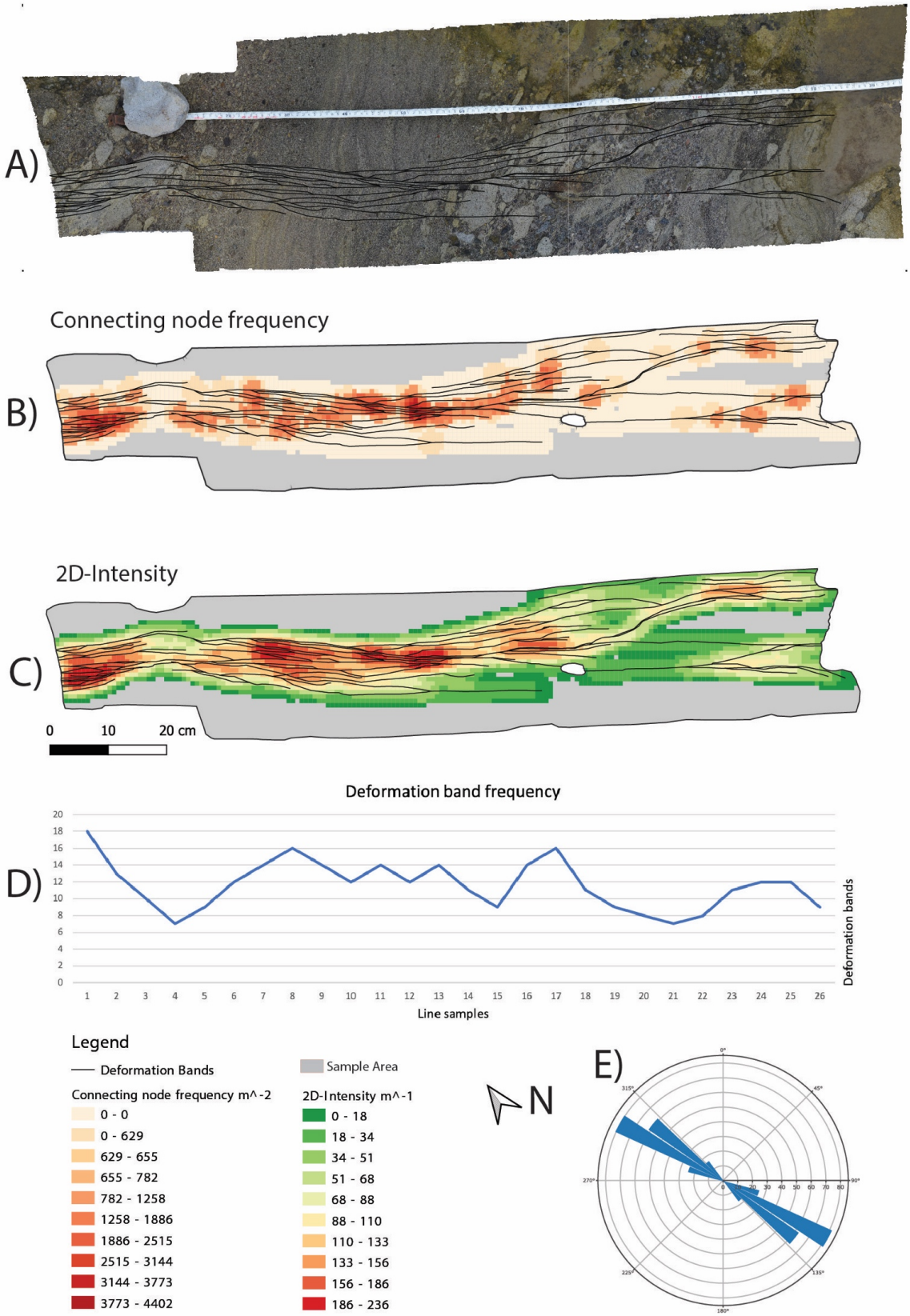

Figure summarizing deformation band network SN-2, the location of the network is shown in Figure 4.3. A) Digitized deformation band network of network SN-4. B) Connecting node frequency map. C) 2D-intensity map, intensity variation within the network. D) Deformation band frequency plot, displaying the variation of deformation bands across the network. E) Rose diagram showing the orientation of the deformation bands.

Appendix IV: Workflow for photo-merging, and NetworkGT

Appendix IV: Workflow in Agisoft Metashape

Agisoft Metashape performs photogrammetric processing of digital images and generates 3D-models to be used in GIS applications. A simplified workflow in Agisoft Metashape is shown here, for a more detailed description, see: Agisoft Metashape User Manual - Professional Edition, Version 1.5 (2020).

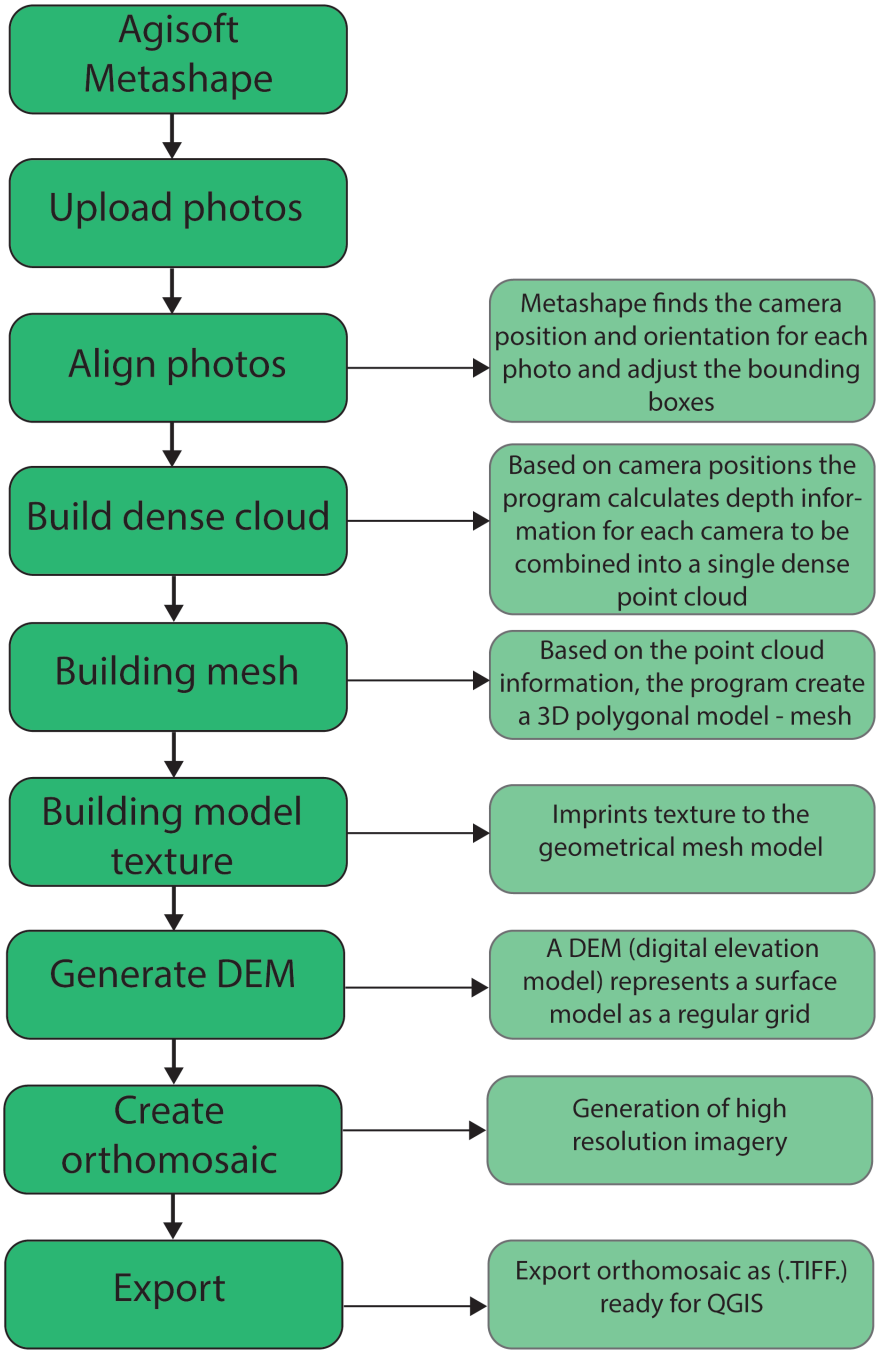

Appendix IV: Workflow in Adobe Photoshop

Network consisting of fewer photos (ten or less) was stitched together in Adobe Photoshop. This is more efficient (faster processing) and gives better results for small networks.

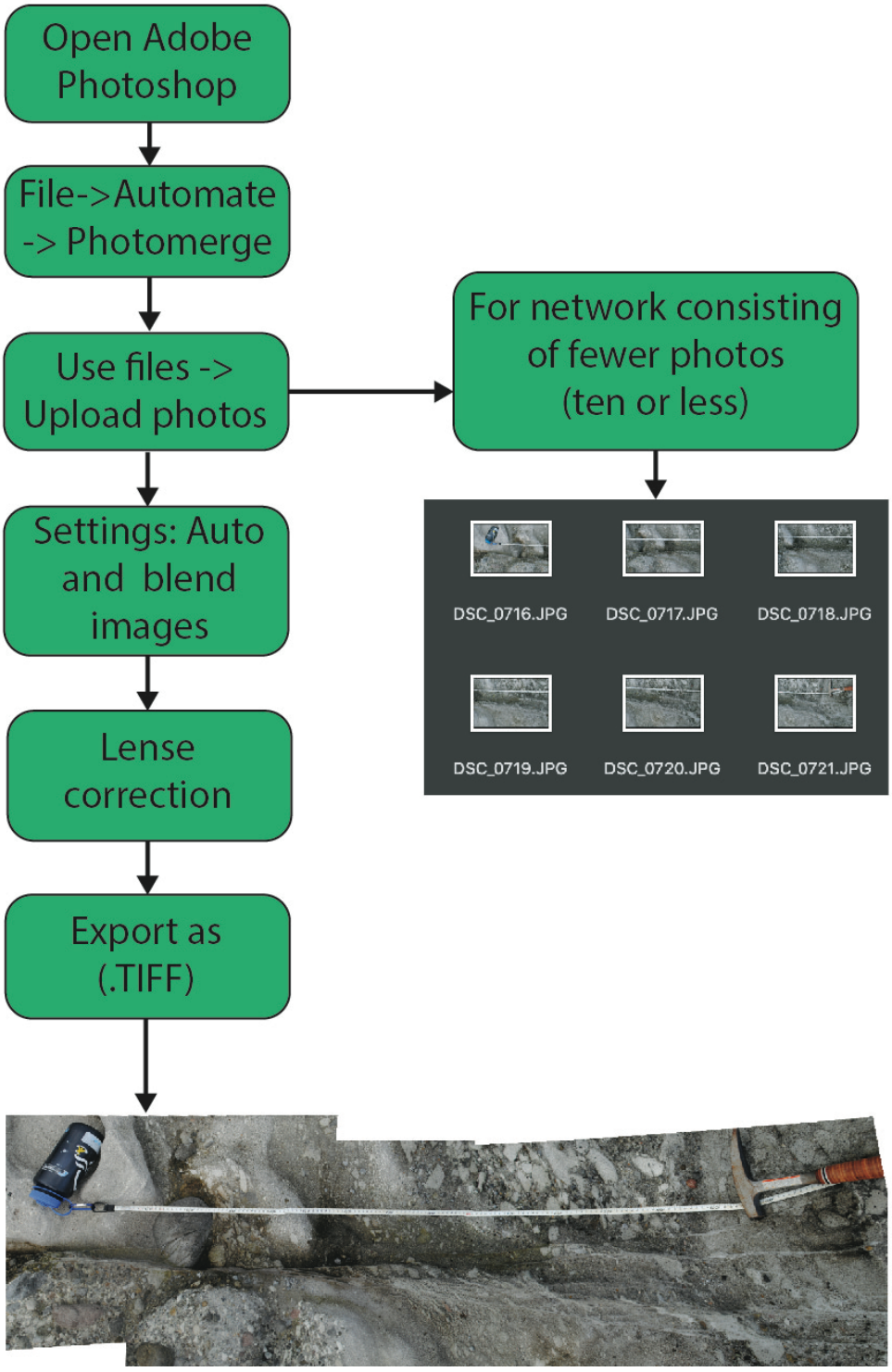

Appendix IV: Workflow in NetworkGT

NetworkGT is an open-source toolbox for GIS applications for sampling, analyses, and spatial mapping of geometrical and topological attributes of two-dimensional networks. The workflow described here is used for extracting and plot geometric and topological information, including plots of deformation band frequency, rose diagrams, topology and different contour maps of topological parameters. For a more detailed description, see Nyberg et al. (2018) "NetworkGT: A GIS tool for geometric and topological analysis of two-dimensional fracture networks".

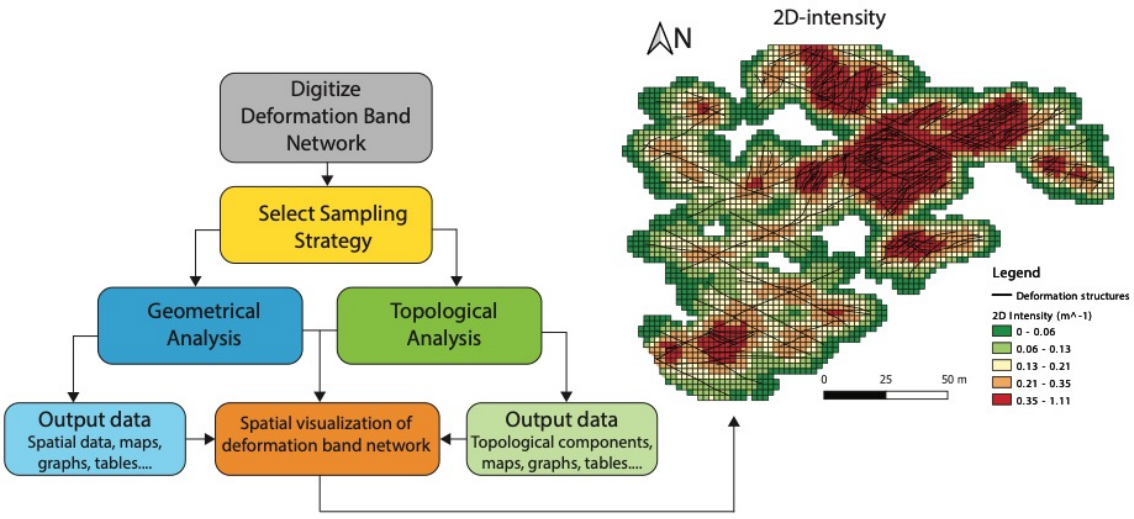

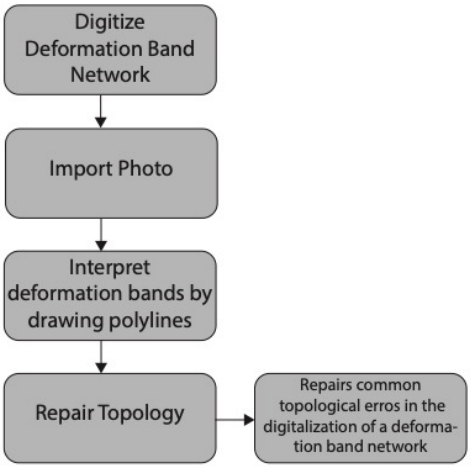

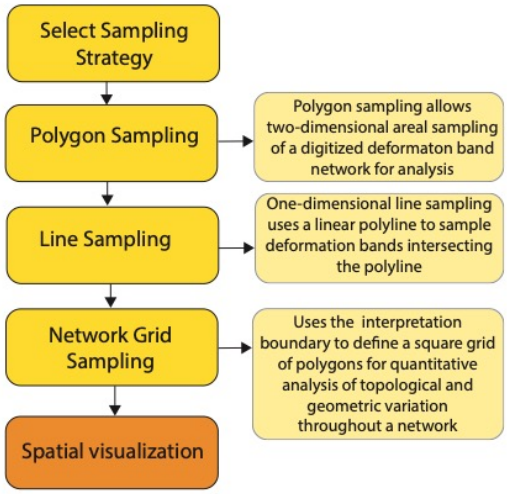

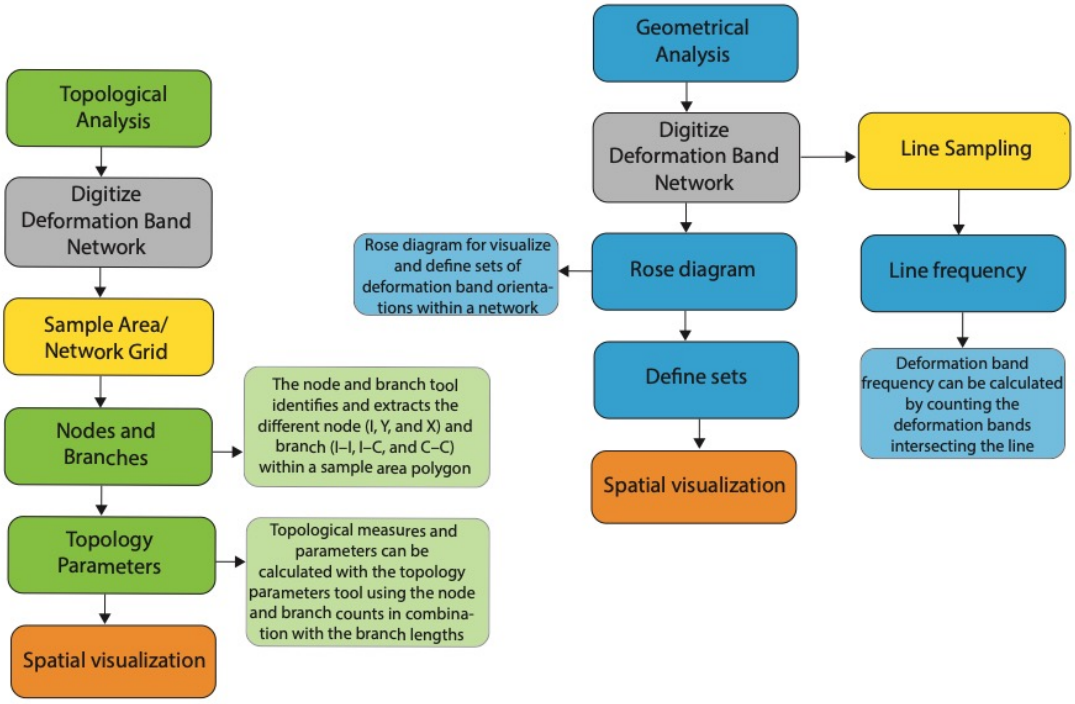

Summary of workflow: The workflow used to extract geometric and topological information from the studied deformation band networks. Grey indicates the work for digitizing the deformation band networks. Yellow demonstrates the different techniques that can be used within NetworkGT. Green indicates the workflow for the topological analysis of a deformation band network. Blue indicates the workflow for the geometrical analysis of a deformation band network.